Plasmon Directed Chemical Reactivity and Nanoparticle Self-Assembly

Erich M. See

Dissertation submitted to the Faculty of the Virginia Polytechnic Institute and State University in partial fulfillment of the requirements for the degree of

Doctor of Philosophy
in
Physics

Hans D. Robinson, Chair
Richey M. Davis
Jean J. Heremans
Leo E. Piilonen

March 21, 2017
Blacksburg, Virginia

Key Words: Nanotechnology, Nano, Plasmon, Plasmonics, Surface Plasmon Resonance, SPR,

Self-Assembly, nanoparticle

Plasmon Directed Chemical Reactivity and Nanoparticle Self-Assembly

Erich M. See

(ABSTRACT):

Nanotechnology has advanced to the point that nanoparticles can now be fabricated in a broad variety of shapes from a wide range of materials, each with their own properties and uses. As the list of manufacturable particles continues to grow, a new frontier presents itself: assembling these existing nanoparticles into more complicated nanoscale structures. The primary objective of this thesis is to demonstrate and characterize one such method of nanoscale construction, the plasmonically directed self-assembly of gold nanospheres onto both silver nanospheroids and gold nanorods. At the heart of this research is a the use of a photocleavable ligand (1-(6-Nitrobenzo[d][1,3]dioxol-5-yl)ethyl(4-(1,2-Dithiolan-3-yl)butyl) carbamate), which is capable of forming a photoreactive self-assembly monolayer (SAM) on gold and silver surfaces. After photoactivation, this SAM becomes positively charged at low pH, allowing it to electrostatically bind with negatively charged gold nanospheres (or other negatively charged nanoparticles). In this thesis, I describe both a secondary photoreaction that this ligand is capable post-photocleavage, which removes the ligand's ability to bind to negatively charged gold nanospheres, allowing for, among other assembly methods, reverse photopatterning. I further show that this photocleavable ligand can be used in conjunction with gold nanospheres to create aligned, metal structures on silver nanospheroid surface by exposure to linearly polarized UV light. Similarly, I also demonstrate how the ligand can be used to preferentially bind gold nanospheres to the ends of gold nanorods with the use of ultrafast femtosecond pulsed 750 nm laser light, making use of multi-photon absorption. Both methods of self-assembly, as well as the secondary photoreaction, are dependent on the plasmonics of the metal nanoparticles. This thesis also goes into the backgrounds of plasmonics, plasmonically mediated catalysis, self-assembly, and photocleavable chemicals.

This work was supported by grants from the National Science Foundation (DMR-1006753) and from the Institute for Critical Technology and Applied Science.

Plasmon Directed Chemical Reactivity and Nanoparticle Self-Assembly

Erich M. See

(GENERAL AUDIENCE ABSTRACT):

Nanotechnology has advanced to the point that nanoparticles can now be fabricated in a broad variety of shapes from a wide range of materials, each with their own properties and uses. As the list of manufacturable particles continues to grow, a new frontier presents itself: assembling these existing nanoparticles into more complicated nanoscale structures. The ability to build and design such structures further advances the use of nanotechnology for medical and industrial applications. In this thesis, I describe and demonstrate a method of nanoparticle self-assembly developed by our group which uses the unique optical properties of metallic nanoparticles in conjunction with a light-activated binding chemical to control and direct the assembly of gold nanoparticles onto a silver nanosphere or gold nanorod base. The preliminary results for both of these techniques are highly promising, and I describe them in detail. I furthermore explore a secondary light-driven reaction our light-activated chemical is capable of. This secondary reaction can prevent particle binding, broadening the applications and techniques of the light-activated binding chemical.

Acknowledgements

I wish to thank Dr. Hans D. Robinson for the guidance, training, and advice he has given me in the course of my doctorate career, as well as the patience he has demonstrated with me while doing so. He has been instrumental in shaping me into the scientist I am today. Thank you to Dr. Webster Santos, Cheryl Peck, and Xi Guo for collaborating with our group on this journey of discovery, and providing us with the photocleavable ligand necessary to have made any of this research possible. To Dr. Jan Yarrison-Rice at Miami University, who helped me take my first steps in nanophysics. I also want to thank Dr. Brad Miller, my high school physics teacher, whose class was like a lightning bolt through my spine. I'd always been interested in science, but it was in his class that I realized I what course in science I wished to pursue.

Thank you to my friends for both pushing me forwards and putting up with me all these years. To my closest highschool friends Daniel Schoenbach and Lat Ware, who helped me navigate those hazardous waters, and who watched my back in those crowded halls. To Charlie Bowman, and to the memory of Ken Akers, for helping push me out of my shell in college and make broader friends. To William Robinson, Phil Hochendoner, and Aaron Turner, my fast friends through my eight years here at Virginia Tech.

To my family—my younger brother Matthew, for his constant companionship and steadfast friendship. To my parents, who've supported me, nurtured me, and helped me to become the people I am today, showing me my talents in both art and science. And who've helped align my moral compass, and advised me in times of confusion.

And to my wife, Jennifer See, who has comforted me in distress, pushed me in moments of hesitation and doubt, and cared for me in moments of illness. Her presence has been a source of deep stability and love, and it means all the world to me.

Table of Contents

Table of Figures

Table of Tables

Chapter 1

1 Introduction

1.1 The State of Nanotechnology

Currently, we could be said to exist in the stone age of nanotechnology. Just as simple stones could be fashioned into tools, just as a sharp rock could be used as an axe, and a smooth rock could be turned into a shovel, we have become increasingly skilled at crafting and forming various shapes — spheres and cubes, fibers and rods, triangles and prisms. And at the nanoscale, like a stone-aged tribe, we have found that these various shapes themselves have a variety of uses, without need for much further alteration. Carbon nanotubes, for instance, are frequently used to strengthen materials or woven to form super-strong, super-light carbon fiber. Gold nanoparticles, without significant alterations, can be used in both the detection and destruction of cancer cells based on their unique optical properties. Colloidal silver has long been used as a powerful anti-microbial. With just slightly further refinement, such as bioconjugating molecules to the surface of the particle, the uses of these particles increase further still.

Having mastered simple nanoscale shapes, we, like our stone-wielding ancestors, now stand at the threshold of building more complex structures. Just as early societies could envision the axle without being able to easily join wheel and rod together, so too do we struggle with nanoscale structures that we can design, but not easily build. And nanoparticles are, as might be imagined, inherently more difficult to work with for a variety of reasons, which can include their size, their stability, and their ease (or lack thereof) of manufacture. Despite this difficulty, we have nevertheless begun to assemble larger scale nanostructures.

There are two primary methods of building these structures--Top-down, which involves rendering nanoscale structures from bulk material, and bottom-up, which involves building nanoscale structures from already-existing nanoscale materials. Of particular interest to our group is bottom-up self-assembly, which involves assembling existing nanoparticles into larger structures via a self-driven, often chemical process, that, once initiated, will build the structure

for us. This is opposed to, for instance, building a structure piece-by-piece with an atomic force microscope.

My research revolves around developing and characterizing new methods of bottom up self-assembly. These methods are optically driven, and in fact rely on the optical properties of the nanoparticles to both drive and direct the self-assembly process. Our ultimate goal is to develop another method of assisted self-assembly, utilizing the very optical property that makes many of these potential structures interesting: Surface Plasmon Resonance (SPR).

By attaching a photocleavable ligand to gold and silver nanoparticles, we can use SPR to selectively photocleave the chemical. This will create a patchy particle, which we will then further use for optically controlled, bottom-up self-assembly.

1.2 Thesis Outline

Chapter 1 (section 1.3 in particular) deals with the necessary literature review for this thesis, going over the backgrounds of my research. This encompasses surface plasmon resonance, plasmon decay, nanoparticle self-assembly, and photocleavable moieties.

Chapter 2 is an in-depth review of all the experimental methods used in this work, in order to make it easier for future graduate students to replicate and build from this work. It includes both the synthesis and preparation of all substrates and nanoparticles used, as well as the exposure and characterization methods. Each section also briefly dips into why a particular nanoparticle, photoexposure, or characterization method might be useful.

Chapter 3 explores a secondary photoreactive effect that our photocleavable ligand undergoes when it is exposed to green light after it has already been photocleaved. I show that this reaction removes the ligand's ability to bind gold nanospheres to itself, and also can only occur after photocleavage. This allows us, among other things, to perform reverse-photoexposures with our photocleavable ligand, expanding our options for controlled self-assembly.

In Chapter 4, I demonstrate that we can use our photocleavable ligand and polarized UV light to preferentially photocleave the ligand at plasmonic hotspots when deposited on silver nanospheroids. I demonstrate this selective photocleavage by conjugating gold nanospheres to the photocleaved sites, and use rotational spectroscopy to demonstrate the presence of aligned nanostructures on the surface.

Chapter 5 looks at using our photocleavable ligand to perform selective self-assembly of gold nanospheres to the ends of gold nanorods. Here, I present preliminary results of this experiment, as well as discuss our group's previous attempts.

1.3 Literature Review

1.3.1 Plasmonics

One particularly interesting trait displayed by metallic nanoparticles are their unique optical properties. Primarily, these properties rely on the behavior of collective electron excitations within the particle, also known as plasmons. They can, broadly, be broken into three categories: bulk plasmons, surface plasmons (SP's), and localized surface plasmons (LSP'S).

I) <u>Bulk Plasmons</u>

Bulk plasmons are excitations in the bulk or volume of the metal, and are not relegated solely to nanoscale surfaces. By modeling a metal as a gas of freely-propagating electrons amidst a set of positively charged atom cores, one can describe the optical properties of a metal. This is also called the plasma model. From this plasma model, we can ultimate derive a plasma frequency—the innate resonant frequency of the electron sea. This frequency can be approximated as

$$\omega_p = \sqrt{\frac{n_e e^2}{m^* \varepsilon_o}}$$

where n_e is the number density, e is the electric charge, m^* is the effective mass of the electron, and ε_0 is the permittivity of free space. Below the plasma frequency, the metal is opaque and reflective to light, while above the plasma frequency, the metal loses this reflectivity and becomes transparent. When exposed to light at the metal's plasma frequency (and only at the

plasma frequency), the oscillating electric field of the light is able to set up a collective oscillation in the material, called a bulk or volume plasmon [1].

II) Surface Plasmons and Surface Plasmon Polaritons

Surface plasmons are collective electron oscillations that propagate along a metal-dielectric boundary. Unlike bulk plasmons, which are volume-oscillations and can only be excited by a specific wavelength of light, surface plasmons are surface waves that can be excited by multiple compatible wavelengths. If x is the direction of propagation, all plasmon oscillations must conform to the dispersion relation

$$k_x = \frac{\omega}{c}\sqrt{\left(\frac{\varepsilon_1 \varepsilon_2}{\varepsilon_1 + \varepsilon_2}\right)}$$

where ω is the frequency of the longitudinal oscillations, ε_1 is the dielectric function of the metal, ε_2 is the dielectric function of air or vacuum, and c is the speed of light.

However, due to a momentum mismatch, light incident on a metal surface in a vacuum cannot stimulate these surface plasmons. One way to alleviate this is to bring the light through a prism before allowing it to interact with the thin metal film, as shown in Figure 1.1 [2].

In this figure, ε_0 is the permittivity of the prism, ε_1 is the permittivity of the metal film, and ε_2 is the permittivity of air, the vacuum, or the surrounding dielectric. In this configuration, specific angles allow incident light to couple to the metal-air interface and produce surface plasmons. These plasmon-photon couplings are sometimes also called surface plasmon polaritons (SPP's). The conditions required for this coupling are

$$k_x = \sqrt{\varepsilon_o}\frac{\omega}{c}\sin(\theta_0)$$

where θ_0 is the angle as shown in Figure 1.1, and where k_x also satisfies the dispersion relation in Equation 1.3.2. At this angle, there is a sharp reduction in the reflected light, as much of it is absorbed and, as the theory indicates, transformed into SPP's.

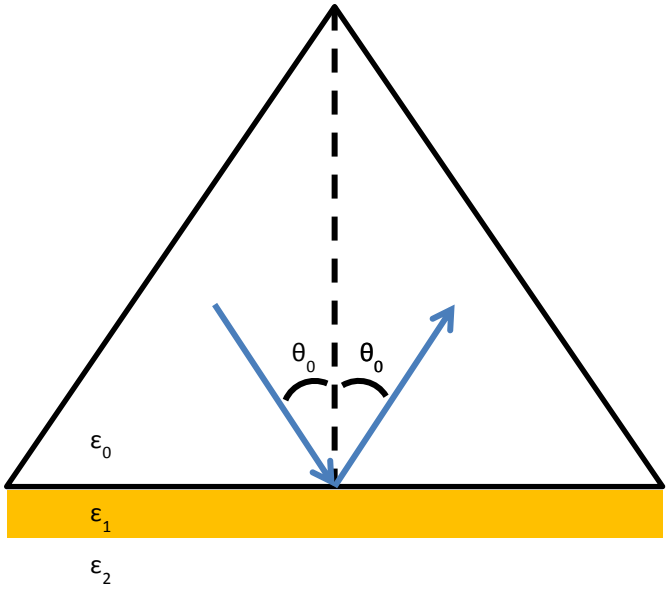

Figure 1.1: Schematic of the setup necessary to induce SPP's on a metal surface with incident light.

III) Localized Surface Plasmons

Plasmon oscillations confined to a nanoparticle are called localized surface plasmons. As we are working with plasmonic nanoparticles, it is this type of plasmon (and plasmon resonance) that we are most interested in.

When light passes near a metallic nanoparticle, the oscillating electric field of the light begins to push the conduction band electrons along the surface of the nanoparticle into a form of collective displacement (Figure 1.2) [3,4]. In the simplest approximation, the free electrons in the nanoparticle are given energy and pushed out of equilibrium by the electric field of the incident light, leaving areas of net positive charge (holes) behind. As the system has been pushed out of equilibrium, the electrons will, in the absence of an electric field, attempt to return to their equilibrium positions. The whole system, then, can be seen as a damped, driven harmonic oscillator, with the high-energy carriers driven by the electric field of the incident light. In plainer terms, it's like a child sloshing back and forth in a bathtub, creating areas of high and low water levels.

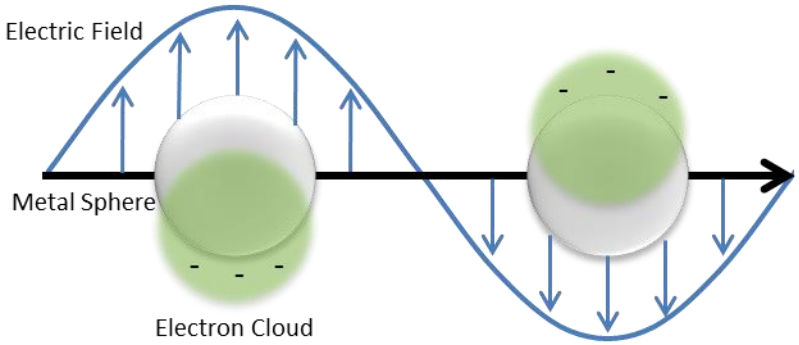

Figure 1.2: Electron displacement in response to an external electric field**.**

Like a damped driven oscillator, the nanoparticle has a resonant frequency, determined by the nanoparticle's size, shape, material, and dielectric surroundings[4]. The closer the frequency of the incident light is to the resonance of the nanoparticle, the stronger the oscillation. When the frequency of the incident light is close to or matches the resonant frequency of the nanoparticle, a very strong enhancement occurs, known as surface plasmon resonance (SPR). At (and near) resonance, the incident light is directed into very intense, localized hot spots, and these in turn result in extreme enhancements in the intensity of the electric field and, consequently, the intensity of the light. These hot spots can have intensities and magnitudes on the order of hundreds or thousands of times more intense than that of the incident light [5]. In a way, we can think of the nanoparticle acting like an antenna when the incident light is near its resonant frequency, collecting and absorbing light from an area larger than that of its physical size and concentrating it into very small volumes (the hot spots) [6].

It is worthwhile to mention that sizes of these hotspots are far smaller than the wavelength of the light incident on the nanoparticle—there is no other way to do this, as the wavelength of the incident light is a limiting factor for all other methods of focusing. This is one of the main reasons (in addition to the enhancement effects) that plasmon resonance is interesting.

One method of mathematically calculating SPR is Mie theory, which will be explained more in-depth in section 4.28.

1.3.2 Applications of Plasmonics

I) Surface Enhanced Raman Spectroscopy

One of the most prominent uses of plasmons is in Surface Enhanced Raman Spectroscopy (SERS), a modification of Raman spectroscopy. All atoms and molecules have intrinsic vibrational modes, which correlate to their structure and, in the case of more complex molecules, sub-structures. At its most basic level, Raman spectroscopy (or vibrational spectroscopy) utilizes the inelastic scattering (Raman scattering) of monochromatic light off of a molecule's vibration eigenmodes in order to create a kind of fingerprint that can be used for identification. When excited by a laser, phonons, (i.e. molecular vibrations,) or other excitations existing in the stimulated molecule can interact with the incident photons and cause a shift in their energy, pushing it up or down. These shifts, in turn, reveal information about the makeup and vibrational modes of the system [7].

Spontaneous Raman scattering is typically very weak. However, when adsorbed onto rough metal surfaces or nanostructures capable of supporting plasmons, the effect is greatly enhanced, sometimes by a factor of 10^{10} or 10^{11}--to the point where the detection of single molecules becomes possible. This is mainly due to plasmonic enhancement. The enhanced optical field adjacent to the plasmonic nanostructure greatly increases the amount of Raman scattering, allowing for a far stronger signal. In this manner, plasmons and plasmonic enhancement greatly contribute to the uses of Raman spectroscopy.

II) SPP Based Biosensors

The sensitivity of SPP's to the surrounding medium can be used to build a biosensor by utilizing the fact that changes to the system's dielectric constant will result in changes to the system's SPR angle. One elegant method involves a half-cylindrical prism, with a single wavelength of light introduced at a fixed angle. The prism's curved surface causes the incident beam to be spread over a broader angle as it passes into the prism. A thin metal film is fabricated on the prism, with binding sites for melocules on the metal surface. Figure 1.3 shows a diagram of this setup [1].

As mentioned previously, at most angles, the light will be well reflected off the metal film. However, light striking the metal film at the SPR angle will instead couple to and excite SPP's in the metal film at the metal-air interface, resulting in a sharp dip in the reflected light. When the incident light is spread out at multiple angles (as in Figure 1.3), this results in a physical absorption band amidst the spread of reflected light, an area of greatly reduced intensity. When a target molecule is brought past the metal film, they will couple to the capture molecules, resulting in a small shift in the dielectric constant of the system. This, in turn, alters the SPR angle, which will result in a physical shift of the absorption band's location**.** By coupling this setup to an optical sensor (such as a CCD camera) and microfluidics system, it can form a biosensor with no moving parts, save those required to push the analyte through the system itself. This allows for the possibility of more portable, rugged biosensors.

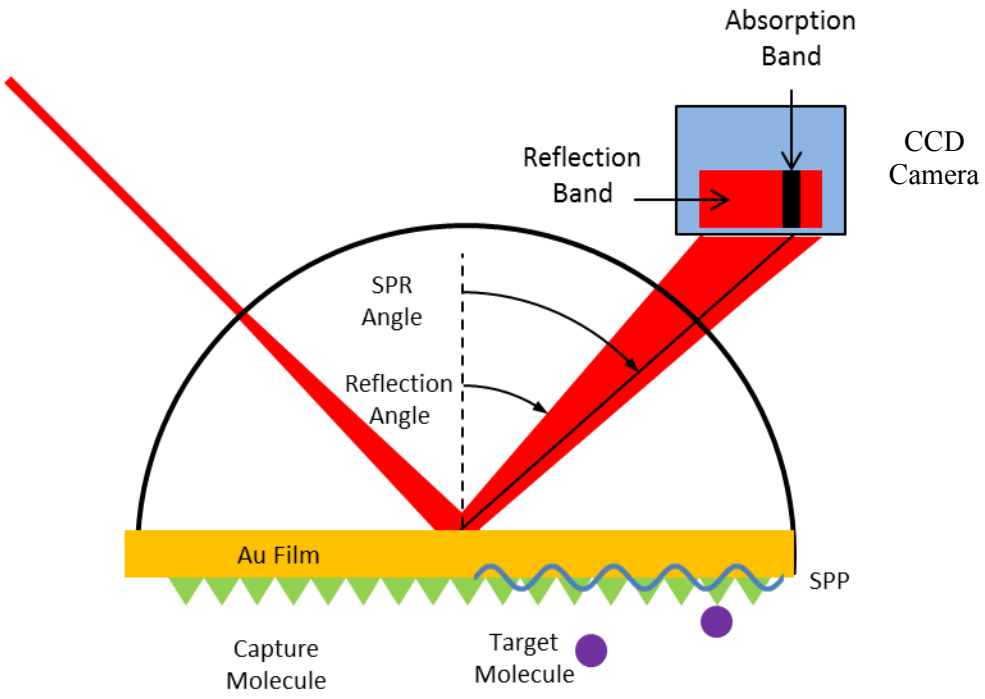

Figure 1.3: Schematic of an SPP based biosensor, using the change in SPR angle to determine whether or not a target molecule (analyte) has passed by a capture molecule

III) LSPR-Shift Sensors

As previously mentioned, small changes in the dielectric constant of a plasmonic nanoparticle's surroundings can result in a significant shift in its surface plasmon resonance. Plasmonic nanoparticles coated in a capture molecule will experience a resonance shift (generally, a redshift) when exposed to the applicable target molecule, as the target molecule's capture will alter the dielectric constant surrounding the nanoparticle. This, in turn, will alter particles' LSPR, which, among other affects, will alter their absorption and scattering spectra. By combining this trait with dark-field microscopy, it becomes possible to build a biosensor centered around singular nanoparticles [1].

One simple, but effective method involves discrete gold or metal nanoparticles of sizes in the 50nm diameter range, deposited onto a transparent surface. When viewed through a dark field microscope, the scattering caused by these singular nanoparticles is visible to the eye, even if the individual nanoparticle cannot be resolved. If submerged in mediums with dielectric constants significantly different than that of air, the wavelength of scattered light can shift to a degree discernable by human observation [8]. If functionalized with a capture molecule, the scattering shifts upon reacting with the target molecule are still large enough to be easily detected by simple optical sensors. This method of biosensing has already been recorded to have a high degree of sensitivity, able to detect concentrations in the zeptomolar range [8,9].

IV) Solar Cell Enhancement

Not all uses of SPR are sensing-based. The light-amplification and scattering properties of plasmonic nanoparticles also have broad applications with regard to energy generation. Specifically, they can be used to enhance existing solar cells. One specific application is enhancing Dye-sensitized solar cells (DSSC's) [7].

Typically, DSSC's consist of a TiO_2 (or other broad-band-gap) semiconductor surface, with a sensitizing dye chemisorbed to it. These are then attached to a transparent, conducting oxide film, which serves as the electrode. When light is adsorbed by the dye, it creates a photoexcited electron, which is in turn passed on to the TiO_2 layer, and then to the conducting electrode. A second reaction reduces the dye to its ground state, carrying a hole to the opposite electrode. DSSC's are attractive because, unlike some other solar methods, they do not require

extremely high purity for their components and their ease of manufacture. However, by themselves they also have a relatively low efficiency--on the order of 9%--compared to other solar cells. However, the inclusion of metal nanospheres into the dye layer of the DSSC's can greatly enhance their efficiency via LSPR. Some of this enhancement comes from mechanisms similar to those in SERS, while some comes from a broader scattering cross section, or a LSPR tuned to the absorption peak of the dye. Silver, in particular, has shown to be particularly useful, both for its ability to be tuned to a broad portion of the visible spectrum, due to the ease of manufacture and capping of silver nanoparticles, due to low plasmonic losses, and due to good environmental stability.

1.3.3 Plasmon Decay:

Plasmon oscillations cannot persist forever. Eventually, they must decay away. This occurs via a variety of mechanisms. The simplest and most readily apparent mechanism is the radiative decay path, in which the plasmon decays via the emission of a photon, removing the energy from the particle, as shown in Figure 3 [10,11].

While radiative decay is in most cases the dominant mechanism of plasmon decay, other, non-radiative decay pathways are also important. As these are non-radiative and do not involve the spontaneous re-emission of a photon, they are collectively referred to as the dark modes of plasmon decay. Three of these decay paths are outlined in Figure 1.4. These pathways are thermoplasmonic heating, hot-carrier injection, and chemical interface damping (CID). In what follows, we will discuss each of them in more detail.

I) <u>Thermoplasmonic Heating</u>

Thermoplasmonic heating is the dominant form of dark-mode plasmon decay, during which a single plasmon oscillation decays and transfers its energy into an electron within the material [12]. When it does this, it excites a single electron existing below the Fermi level to a state well above the Fermi level, leaving a hole behind, resulting in a high-energy electron-hole pair. Collectively, these are known as hot carriers (hot electrons and hot holes) due to their energies being larger in magnitude than the thermal energy of the particle would predict.

After a short time span (~1-10 fs following the creation of the hole-electron pair) the high-energy carriers begin to interact with their nearby neighbors, sharing energy and scattering off them, creating more energetic carriers (of lower energy) in the process, until the electrons have thermalized at a temperature above the ambient. Starting at around 100 fs, these carriers, in turn, begin transferring some of their energy to the particle's lattice via electron-phonon interactions, causing the thermal temperature of the nanoparticle to rise, as outlined in Figure 1.4a. Eventually, this brings the electronic and lattice temperature back into equilibrium with each other, resulting in the heating of the nanoparticle [12-17]. This entire process occurs on a time scale on the order of 1-100ps. This thermal heating can result in greatly elevated temperatures, high enough to boil water or generate tissue damage [18-20].

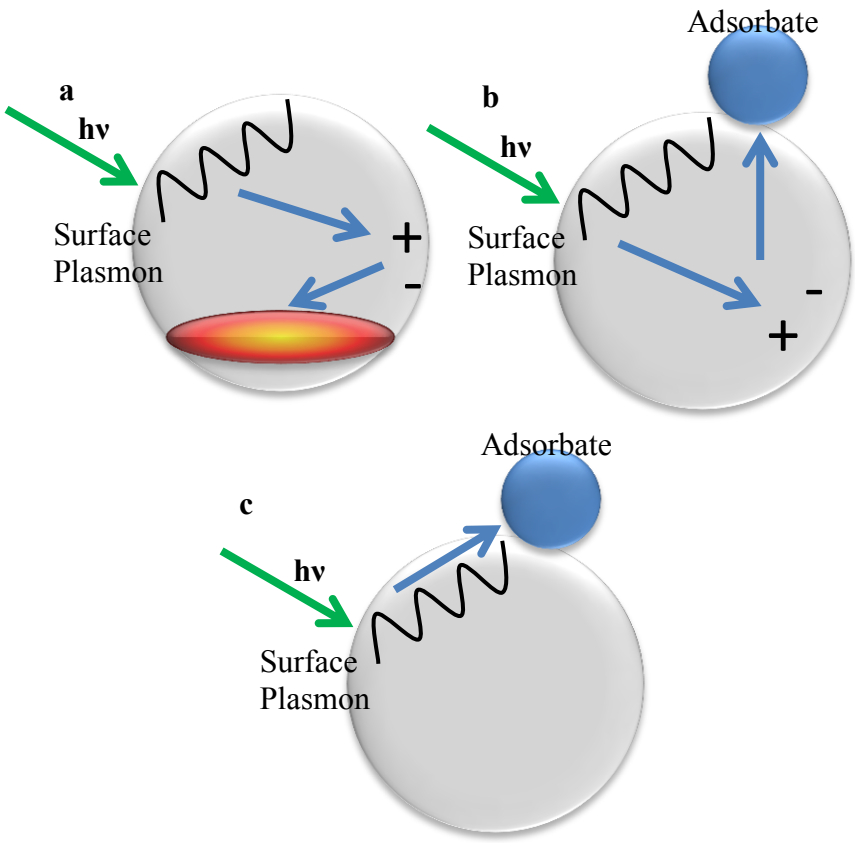

Figure 1.4: Three dark-mode decay mechanisms. a) Thermoplasmonic heating, in which the plasmon decays into a high-energy electron hole pair, which lose energy and heat the particle. b) Hot-carrier injection, in which the plasmon decays into a high-energy electron hole pair, one (or both) of which escape the particle to a nearby receptor site, and c) Chemical Interface Damping (CID), in which a plasmon decays via direct interaction with an adsorbate, exciting a high-energy carrier inside an available state.

This ability to heat nanoparticles to such high temperatures allows for a wide range of applications. A medical use, for instance, is the imaging and heat-treatment of cancer tumors. When using nanoparticles which are resonant within the transparency window for human tissues (700-900nm), it becomes possible to thermally damage tissues which have been impregnated by nanoparticles, while avoiding damage to tissue without nanoparticle deposits. Hirsh, L.R. et al demonstrated the viability of this technique in vivo [18]. Anesthetized mice had tumors treated with iron-core gold nanoshells, and were then exposed to an infrared laser. Tissue which received nanoparticles experienced a temperature increase of ~37K, which is more than sufficient to cause instant cell death, effectively cauterizing the tumors from within. In contrast, nanoshell-free tissues experienced a temperature increase of only ~9K, below the threshold necessary to cause permanent tissue damage. This selectivity of the nanoparticle heating allows for target cancer treatment, provided the nanoparticles are only deposited in cancer tissues. Studies have shown similar results, where nanoparticles have been able to completely destroy prostate tumors [21].

II) Hot Carrier Injection

Under certain circumstances, the charge carriers generated via the initial plasmon decay of Landau damping do *not* stay within the particle and result in heating. Due to their high energy, these carriers are freer to move farther away from the surface of the nanoparticle than an equilibrium electron would be. As shown in Figure 1.4b, if there is a nearby acceptor state, such as from an adsorbed molecule or adjacent surface, the high energy carriers (or some of the still-very-energetic carriers generated by the initial scattering) can tunnel into these states, leaving the particle [22-26]. This entire event occurs within 1ps after the plasmon decays into the initial hot carriers. Some controversy over this mechanism exists–1ps is much, much greater than the 10fs it should take for those carriers to relax via thermoplasmonic heating. Nevertheless, evidence suggests that it does occur, as discussed in the next section.

III) Chemical Interface Damping

Chemical Interface Damping (CID) also results in the injection of hot carriers into a nearby adsorbate or substrate, but does so via a different mechanism than the hot-carrier-injection that can come from Landau damping, outline in Figure 1.4c. In CID, plasmon decay comes about as a

result of the oscillating plasmon directly interacting with an adsorbed molecule. When the oscillating plasmon interacts with an unoccupied state on the adsorbate, it can decay via the directly exciting a hot electron (or hole) into the available state [27-29].

While determining the mechanism of carrier injection into an adsorbate is a difficult task, both mechanisms result in similar consequences. In both cases, the hot-carrier injection or excitation can result in catalysis on existing adsorbate molecules via interaction with specific molecular orbitals [22, 30-33]. Some orbitals can, if populated by an electron, weaken the intra-atomic bonds within a molecule, resulting in molecular instability, which are called anti-bonding orbitals. Conversely, some orbitals promote and stabilize intra-atomic bonds if populated by an electron, and these are called bonding orbitals. During hot-carrier injection, additional orbitals are sometimes occupied (or, in the case of hot holes, depopulated). If an electron populates an anti-bonding orbital (or a hole depopulates a bonding orbital), an adsorbed molecule can be rendered unstable, promoting it to cleave or otherwise change its composition. Similarly, adsorbed chemicals can also be made react and bind with each other.

One simple, but demonstrative example is the room-temperature plasmon-induced dissociation of molecular Hydrogen (H_2) into elemental Hydrogen (H) [34,35]. Au nanoparticles were laid down on a Titanium Oxide (TiO_2) substrate and then exposed to a steady stream of hydrogen. While gold does not have strong binding energy with H_2, it will diffuse into the TiO_2 matrix, ensuring contact with the gold nanoparticle. In order to measure the disassociation of H_2, a stream of H_2 and molecular Deuterium (D_2) were blown over this substrate, with the output of Hydrogen-Deuterium (HD) monitored. The production of HD would be tied directly to the disassociation of H_2 (and, by extension, D_2). When exposed to a laser, HD was found to form at a rate six times higher than prior to the laser's ignition. This increase in HD production could not simply be attributed to the temperature increase generated by the laser, as heating the nanoparticles in dark conditions resulted in only a two-fold increase in the production of HD, suggesting that the disassociation observed under laser illumination is indeed a plasmon-based effect. Current theory suggests that hot electrons generated by plasmon decay in the gold nanoparticle were transferred into the H_2 molecule's anti-bonding orbital. This, in turn, greatly weakens the H_2 bond and leads to the molecule's disassociation [35].

1.3.4 Nanostructure Creation

Currently, nanoscience is pushing at the frontiers of more complicated structures. Already, nanoparticles have been adhered to bulk surfaces and mixed into epoxies, creating materials that are super-hydrophobic [36] or exceptionally strong and light [37]. But these are mostly random depositions of particles in a matrix. Creating well-ordered and structured composite nanostructures is a more challenging prospect, a goal that is only now being realized. With this new goal, too, come new challenges. Among them is that attaching nanoparticles to *other* nanoparticles in both a controlled fashion and on industrial scales proves difficult, as does simply carving out complex nanostructures with top-down methods.

Top down methods involve taking bulk material and rendering nanoscale structures out of them, such a photolithographic etching. These methods are limited to either one material, as is the case in most photolithographic etching methods, or slow processing times for nanoscale structure creation, or both. Furthermore, the size and type of the structures assembled are limited by factors such as the wavelength of visible light.

Bottom-up approaches, while generally faster and amenable to larger-scale fabrication, come with a variety of complications, including the fact that nanoparticles are inherently unstable. In solution, nanoscale particles have a tendency to aggregate, due to the lower free energy level of bulk matter (or their high surface-area-to-volume ratios). To be kept stable in solution, they must be coated in either a charged or steric barrier in order to prevent aggregation. For instance, the humble gold nanospheres are, when synthesized, coated in a citrate layer that gives them a negative charge **[38].** This uses electrostatic repulsion to prevent aggregation. If this charge is neutralized, the gold nanospheres very quickly aggregate and drop out of solution, as this aggregated, bulk state is the free energy minimum. It is via manipulating the state which represents the free energy minima that we can perform bottom-up self-assembly, whether via altering the chemical makeup of the nanoparticle solution, or by introducing an outside force, or some combination thereof—both chemically altering the nanoparticles while guiding them using an outside force, pushing the nanoparticles towards a new free energy minimum.

I) <u>Undirected Self Assembly</u>

Undirected self-assembly methods include utilizing changes to the hydrophobicity[39], solubility[40,41], electrostatic[40,42], or other basic properties[43] of the nanoparticles to get them to assemble or build off of each other. This is undirected because once the process has started, it proceeds via any outside influence or forces until the particles reach their new free energy minimum, or get stuck in a local minimum.

An example of hydrophobic self-assembly involves gold nanospheres coated in a polystyrene (PS) brush in THF. Upon the addition of water (which is a nonsolvent for PS), the gold nanospheres begin to aggregate. While the addition of a polymeric surfactant can suppress further aggregation, mild heating at 70˚C after the surfactant has been added leads to the expulsion of THF and creates a tight cluster of the hydrophobic nanospheres [44]. Solvent forces can be manipulated in a similar manner. In one example, cetyltrimethylammonium bromide (CTAB) coated gold nanorods were capped at their ends with polystyrene tethers. By introducing salt to the solution, the solvent quality of the polystyrene in the solution was reduced, causing the gold nanorods to assemble into long chains [40].

Electrostatic self-assembly can take two forms. One is the suppression of electrostatic forces that are *preventing* nanoparticle aggregation. Such is the case of gold nanospheres, which are generally stabilized in solution due to negative charge carriers adsorbed on their surface. In these cases, self-assembly is affected by *suppressing* the electrostatic repulsion force. This can be done via a variety of means, such as altering pH, salt content, and temperature [40,42]. By altering these variables, the gold nanospheres (or other charge-stabilized nanoparticles) can be caused to cluster and together, their electrostatic repulsion weakened [45]. The other approach is to combine oppositely charged particles, such as positively charged gold spheres and negatively charged silver spheres, and allowing them to assemble into crystalline structures [46].

II) Controlled Self-Assembly

Uncontrolled self-assembly methods have their own limitations. As they rely solely on chemical reactions and manipulations, they are, by nature, undirected once started—which means the nanoparticles may get ‘stuck’ in a local free energy minima, take a long time to reach said minima, or assemble together into an undesired shape. Furthermore, uncontrolled self-assembly can be somewhat limited in the structures it can build. To design more refined methods of

nanoparticle combination, we must turn to *assisted* self-assembly, in which an outside force or influence manipulates and alters the self-assembly of the nanoparticles [47]. These can include magnetic[48], electric[49], or shear fields[50], as well as the use of specially-crafted template substrates[51], patterned surfaces designed to alter nanoparticle assembly. In all of these cases, the self-assembly process is no longer a self-contained reaction, and is instead assisted by this outside field or template that controls and guides the assembly.

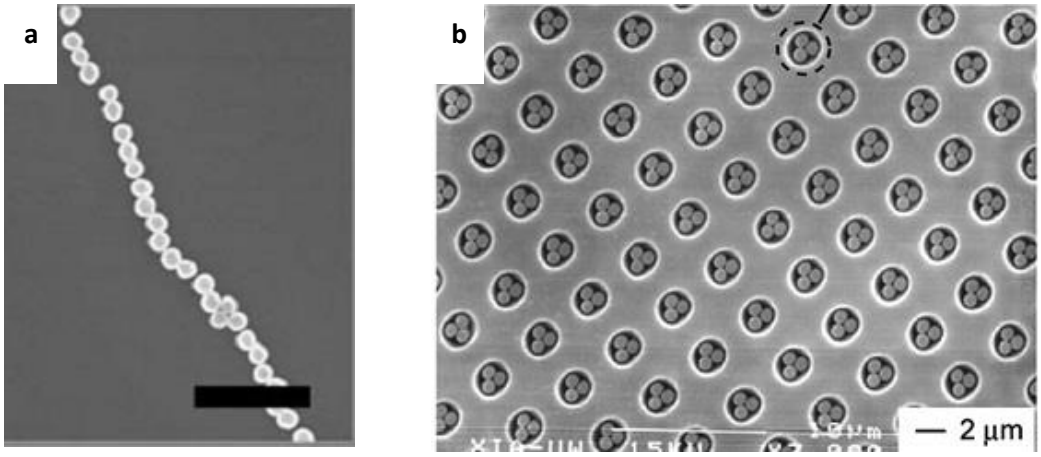

Figure 1.5: Two results of controlled self-assembly. a) 1D chain of iron-core gold nanoshells formed via applied magnetic field. Scale bar is 1µm. From L.N. Kim et al [48] b) Polystyrene spheres formed into trimer couplets via template-assisted self-assembly. From Rycenga et al. [51]

Iron-core gold-nanoshell particles can be assembled by the application of magnetic fields. L.N. Kim et al demonstrated both tis assembly, as well as that by altering the direction of the fields, the chains would likewise assemble along different axis [48]. An example of the template method can be seen in M. Rycenga D et al, where instead of an outside force, a nanosphere solution was introduced to a silicon substrate with small, specially designed pits etched into its surface [51]. By slowly evaporating the colloidal suspension, the spheres were locked into an arrangement set by the shape of the pits and size of the nanospheres, which can be seen Figure 1.5.

1.3.5 Patchy Particles

The above methods use largely isotropic, symmetrical nanoparticles in their self-assembly process, which ultimately limits what can be formed, even using outside forces to direct the

process. In order to build more complicated structures, it can be advantageous to introduce anisotropies to the nanoparticles. One way to achieve this is through particles with small areas or patches that are chemically or physically different from the rest of the particle, lending them the name patchy particles. Patchy particles can have anywhere from one single, differentiated patch, to upwards of six of seven patches dotting a surface [52-54].

One method of patchy particle creation is particle lithography. Particle lithography involves depositing charged colloidal particles on an oppositely charged surface. After this deposition, the particle is then functionalized via chemical or evaporative processes, and the portion of the particle in contact with the surface is shielded from this functionalization. In many ways, this is similar in concept to templating [55].

There are many other methods of patchy particle creation, spanning from using DNA to strategically bind to specific nanoparticle segments to ablating and altering small areas of a nanoparticle with precise laser illumination to depositing material on specific parts of a particle—to list and describe all the known methods of patchy particle fabrication would be a thesis in and of itself [54].

Once fabricated, patchy particles can be used to assemble larger nanoscale structures via either self-assembly or directed self-assembly. One dramatic example of self-assembly with patchy particles involves negatively charged polystyrene spheres modified with two different caps, labeled ‘A’ and ‘B’ as seen Figure 1.6a**,** whose bonding abilities depend on the ionic strength of the solution [56]. At low ionic strength, the A caps would preferentially bond to other A caps. At higher ionic strengths, B-B bonds became possible, while A-A bonds were less favored, but still existent. This allows for assembly to proceed in stages, controlled only by the ionic strength of the solution. For instance, one could start at a low ionic strength to favor A-A bonds, then increase the solution’s ionic strength to formulate B-B bonds once the A-A bonds had formed, so that the complex structures such as those shown in Figure 1.6 can assemble.

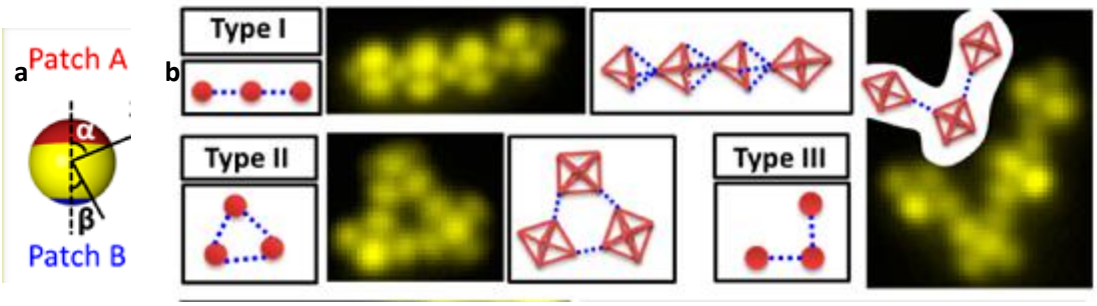

Figure 1.6: Two-patch particle for self-assembly. a) Demonstration of the two different patches. b) Assemblies of particles depending on ionic bond strength and order. From Chen et al. [56]

Another example of controlled self-assembly using patchy particles involves the use of single-patch polystyrene nanospheres with one hemisphere coated in a thin gold shell [57-59]. By applying an external AC field, these spheres were forced to self-assemble into various staggered chains. Furthermore, variations in the field intensity and frequency of the field result in different orderings of the chains, from highly ordered 2-D crystals to non-crystalline groupings.

1.3.6 Photocleavable Protective Groups

Photocleavable protecting groups (PPG's) are, as their name implies, protective groups that can be bound to other moieties, capping them and preventing them from reacting, thus protecting them in the way a marker cap protects a marker. Upon illumination with light at the proper wavelength and intensity, PPG's will cleave, releasing one or more leaving groups and uncaging the protected moiety. This makes it possible to control both the time and place the uncaged moieties are able to interact with their environment. One use for these PPG's is to control an uncaged moiety's introduction to a biological system—including bioagents, acids, bases, pheromones, etc. Therefore, biocompatibility and solubility are primary considerations. Another important factor is the activation wavelength—wavelengths well above 300nm are desirable, as biological tissues will be less likely to absorb (and be damaged) by light in this range.

The most commonly PPG's belong to the nitroaryl group, including nitrobenzyl and nitrophenethyl compounds. Many of these compounds have activation wavelengths in the 320 nm to 370 nm range. However, the compounds sometimes can form into toxic and strongly absorbing byproducts, leading to issues with biocompatibility. These are by no means the only

group of PPG's, however. Others include arylcarbonylmethyl groups, coumarin-4-ylmethyl groups, and arylmethyl groups. Each have their own properties, uses, and sensitivities. An exhaustive exploration of PPG's would take an entire thesis, and their uses too extend past chemical delivery. We ourselves are using a ligand containing an o-nitrobenzyl PPG, which we discuss in depth in Chapter 2.Other uses and considerations for these PPG's include directed self-assembly, as we'll discuss in Chapter 2.2.

1.4 Objectives

The primary objective of this thesis is to demonstrate a new method of controlled self-assembly, that being plasmonically directed self-assembly. The thrust of our research relies on a photocleavable ligand (described in section 2.2). By coating a plasmonic nanoparticle in this ligand (the base nanoparticle on which other particles will be assembled) and utilizing SPR to direct and control the intensity of light incident on the nanoparticle, we can selectively cleave the ligand at the plasmonic hotspots. This creates differentiated areas on the formerly isotropic surface of the nanoparticle, turning it into a patchy particle. These patches are capable of binding with negatively charged particles, allowing us to create structures based on the location of the base particle's plasmonic hotspots.

Chapter 4 and Chapter 5 both present work on this premise, with different base nanoparticles presented in each. This thesis also describes a secondary photoreaction that our photocleavable ligand can undergo after it has been photocleaved. This photoreaction alters the ligand's binding ability, and so can be used to help further guide the directed self-assembly. This work is presented in Chapter 3.

Chapter 1 References

[1] S. A. Maier, *Plasmonics: fundamentals and applications* (Springer, New York, 2007), Vol. 1st, Book, Whole.
[2] H. Raether and SpringerLink, *Surface Plasmons on Smooth and Rough Surfaces and on Gratings* (Springer Berlin Heidelberg, Berlin, Heidelberg, 1988), Vol. 111, Book, Whole.
[3] A. Wokaun, Molecular Physics **56**, 1 (1985).
[4] K. L. Kelly, E. Coronado, L. L. Zhao, and G. C. Schatz, The Journal of Physical Chemistry B **107**, 668 (2003).
[5] X. Kou, W. Ni, C.-K. Tsung, K. Chan, H.-Q. Lin, G. D. Stucky, and J. Wang, Small **3**, 2103 (2007).
[6] C. F. Bohren, American Journal of Physics **51**, 323 (1983).
[7] T. V. Shahbazyan and M. I. Stockman, *Plasmonics: theory and applications* (Springer, New York, 2013), Vol. 15.;15;, Book, Whole.
[8] A. D. McFarland and R. P. Van Duyne, Nano letters **3**, 1057 (2003).
[9] R. P. Van Duyne, A. J. Haes, and A. D. McFarland, in *Proceedings of SPIE*2003), pp. 197.
[10] K. L. Ngai and E. N. Economou, Physical Review B **4**, 2132 (1971).
[11] M. L. Brongersma, N. J. Halas, and P. Nordlander, Nat Nano **10**, 25 (2015).
[12] A. Manjavacas, J. G. Liu, V. Kulkarni, and P. Nordlander, ACS Nano **8**, 7630 (2014).
[13] S. Link and M. A. El-Sayed, The Journal of Physical Chemistry B **103**, 8410 (1999).
[14] C. Voisin, N. Del Fatti, D. Christofilos, and F. Vallée, The Journal of Physical Chemistry B **105**, 2264 (2001).
[15] G. Baffou and R. Quidant, Laser & Photonics Reviews **7**, 171 (2013).
[16] G. Baffou, R. Quidant, and C. Girard, Applied Physics Letters **94**, 153109 (2009).
[17] H. H. Richardson, M. T. Carlson, P. J. Tandler, P. Hernandez, and A. O. Govorov, Nano Letters **9**, 1139 (2009).
[18] L. R. Hirsch, R. J. Stafford, J. A. Bankson, S. R. Sershen, B. Rivera, R. E. Price, J. D. Hazle, N. J. Halas, and J. L. West, Proceedings of the National Academy of Sciences **100**, 13549 (2003).
[19] V. P. Zharov, K. E. Mercer, E. N. Galitovskaya, and M. S. Smeltzer, Biophysical Journal **90**, 619 (2006).
[20] O. Neumann *et al.*, Proceedings of the National Academy of Sciences **110**, 11677 (2013).
[21] J. M. Stern, J. Stanfield, W. Kabbani, J.-T. Hsieh, and J. A. Cadeddu, The Journal of Urology **179**, 748.
[22] K. Watanabe, D. Menzel, N. Nilius, and H.-J. Freund, Chemical Reviews **106**, 4301 (2006).
[23] J. I. Gersten and A. Nitzan, Surface Science **158**, 165 (1985).
[24] P. Dombi, A. Hörl, P. Rácz, I. Márton, A. Trügler, J. R. Krenn, and U. Hohenester, Nano Letters **13**, 674 (2013).
[25] A. O. Govorov, H. Zhang, and Y. K. Gun'ko, The Journal of Physical Chemistry C **117**, 16616 (2013).
[26] R. Sundararaman, P. Narang, A. S. Jermyn, W. A. Goddard Iii, and H. A. Atwater, Nat Commun **5** (2014).
[27] K. Wu, J. Chen, J. R. McBride, and T. Lian, Science **349**, 632 (2015).
[28] M. J. Kale, T. Avanesian, H. Xin, J. Yan, and P. Christopher, Nano Letters **14**, 5405 (2014).
[29] H. Petek, M. J. Weida, H. Nagano, and S. Ogawa, Science **288**, 1402 (2000).
[30] L. Brus, Accounts of Chemical Research **41**, 1742 (2008).
[31] A. Nitzan and L. E. Brus, The Journal of Chemical Physics **75**, 2205 (1981).
[32] J. Gavnholt, A. Rubio, T. Olsen, K. S. Thygesen, and J. Schiøtz, Physical Review B **79**, 195405 (2009).

[33] P. V. Kamat, The Journal of Physical Chemistry B **106**, 7729 (2002).
[34] S. Mukherjee *et al.*, Nano Letters **13**, 240 (2013).
[35] S. Mukherjee, L. Zhou, A. M. Goodman, N. Large, C. Ayala-Orozco, Y. Zhang, P. Nordlander, and N. J. Halas, Journal of the American Chemical Society **136**, 64 (2014).
[36] R. G. Karunakaran, C.-H. Lu, Z. Zhang, and S. Yang, Langmuir **27**, 4594 (2011).
[37] S. U. Deokar and S. Visal, International Journal for Innovative Research in Science and Technology **2**, 238 (2016).
[38] G. Frens, Nat Phys Sci **241**, 20 (1972).
[39] A. Sánchez-Iglesias *et al.*, ACS Nano **6**, 11059 (2012).
[40] K. Liu, C. Resetco, and E. Kumacheva, Nanoscale **4**, 6574 (2012).
[41] M. Grzelczak, A. Sánchez-Iglesias, H. H. Mezerji, S. Bals, J. Pérez-Juste, and L. M. Liz-Marzán, Nano Letters **12**, 4380 (2012).
[42] H. Zhang and D. Wang, Angewandte Chemie International Edition **47**, 3984 (2008).
[43] D. Fava, M. A. Winnik, and E. Kumacheva, Chemical Communications, 2571 (2009).
[44] A. Sánchez-Iglesias *et al.*, ACS nano **6**, 11059 (2012).
[45] G. Mariani, D. Moldenhauer, R. Schweins, and F. Gröhn, J. Am. Chem. Soc **138**, 1280 (2016).
[46] A. M. Kalsin, M. Fialkowski, M. Paszewski, S. K. Smoukov, J. M. B. Kyle, and B. A. Grzybowski, Science **312**, 420 (2006).
[47] Y. Sun *et al.*, Faraday Discussions **181**, 463 (2015).
[48] L. N. Kim, E.-G. Kim, J. Kim, S.-E. Choi, W. Park, and S. Kwon, Bulletin of the Korean Chemical Society **33**, 3735 (2012).
[49] M. Mittal and E. M. Furst, Advanced Functional Materials **19**, 3271 (2009).
[50] B. Martín-García and M. M. Velázquez, Langmuir **30**, 509 (2014).
[51] M. Rycenga, P. H. C. Camargo, and Y. Xia, Soft Matter **5**, 1129 (2009).
[52] É. Duguet, C. Hubert, C. Chomette, A. Perro, and S. Ravaine, Comptes Rendus Chimie **19**, 173 (2016).
[53] A. B. Pawar and I. Kretzschmar, Macromolecular Rapid Communications **31**, 150 (2010).
[54] A. Walther and A. H. E. Müller, Chemical Reviews **113**, 5194 (2013).
[55] G. Zhang, D. Wang, and H. Möhwald, Nano Letters **5**, 143 (2005).
[56] Q. Chen, S. C. Bae, and S. Granick, Journal of the American Chemical Society **134**, 11080 (2012).
[57] S. Gangwal, O. J. Cayre, and O. D. Velev, Langmuir **24**, 13312 (2008).
[58] S. Gangwal, A. Pawar, I. Kretzschmar, and O. D. Velev, Soft Matter **6**, 1413 (2010).
[59] S. Gangwal, O. J. Cayre, M. Z. Bazant, and O. D. Velev, Physical review letters **100**, 058302 (2008).

CHAPTER 2

2 Experimental Procedures

2.1 INTRODUCTION

This chapter is meant to serve not only as an explanation of the various methods by which I prepared and measured the samples studied in this thesis, but also as a guide to future graduate and undergraduate students who wish to replicate or repeat my procedures. Because of this, I will detail my experimental procedures in depth, including some minor details that helped synthesis proceed and missteps that caused procedures to fail. I will also go into detail as to when and why to use a specific method. Unless otherwise noted, all water used was ultrapure de-ionized water.

Section 2.2 examines the photocleavable ligand used in all our experiments, and details its properties, as well as the methods of forming self-assembled monolayers on silver and gold surfaces. Section 2.3 describes the synthesis, characterization, and methods of deposition for gold nanospheres. Section 2.4 describes the synthesis techniques used to make the gold nanorods used in Chapter 5, as well as the methods for depositing them onto a sample substrate. Section 2.5 describes the method of creating a Tollens surface, a sample substrate that is coated in silver nanospheroids. Furthermore, it details the properties of these substrates. Section 2.6 discuses, in brief, the mechanisms for building thick metal films, as well as the reasons for using them. Section 2.7 discusses the various ways in which our substrates are photoexposed, including with unpolarized UV light, green light, an ultrafast femtosecond red laser, and a continuous wave UV laser. Section 2.8 discusses the three primary ways we characterized our samples –spectroscopy, rotational spectroscopy, and field emission scanning electron microscope (FESEM) imaging.

2.2 1-(6-Nitrobenzo[d][1,3]dioxol-5-yl)ethyl(4-(1,2-Dithiolan-3-yl)butyl) carbamate—Our Photocleavable Ligand

2.2.1 Photoreactive Ligand Background

All of the research presented in this thesis revolves around the use of a photoreactive *o*-nitrolbenzyl ligand, shown in Scheme 3.1**.**

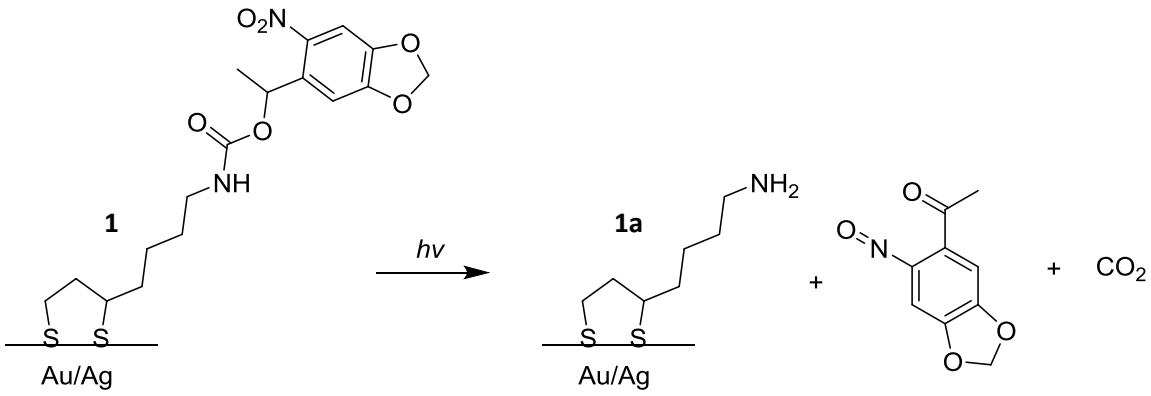

Scheme 2.1: Photocleavable ligand at the heart of our research. 1 will undergo photocleavage when exposed to Ultraviolet (~365nm) light, breaking into the amine-terminated 1a, its leaving group, and CO_2. Both1 and 1a are capable of forming SAM's on gold and silver surfaces via the double-sulfide group.

This photocleavable ligand (**1)** is capable of chemically bonding with Au and Ag surfaces via the disulfide group, and was extensively documented in Daengngam et al.[1] When exposed to a gold film, a 1mM solution of **1** in ethanol formed a self-assembled monolayer (SAM) on the surface, with a density of ~123 ng/cm^2 after an exposure time of six hours. When the solution was replaced with ethanol, no loss of density was recorded, further indicating that it had formed a stable SAM. [1]

When exposed to ~1 J/cm^2 of UV (365 nm) light, the ligand undergoes a photouncaging process to form three byproducts: the leaving group, CO_2, and **1a**. This process is characterized by a shift in the absorption spectrum of the solution and the ability of the primary amine group on **1a** to bind gold nanospheres (AuNSs) to itself. This occurs because when the amine is group at the terminal end of **1a** is subjected to low pH, it becomes positively charged. Therefore, when

submerged in a bath of low-pH, negatively charged AuNSs, the activated ligand can be used to adhere the gold nanospheres to a UV-exposed gold (or silver) surface conjugated with **1**, illustrated in Figure 2.1. We can see that gold nanospheres (bright spots) by and large only bond to photoactivated areas of the ligand-coated surface.

Below exposures of 1 J/cm^2, some AuNS adhesion still occurs, as shown by Daengngam in his doctoral dissertation.[2] Figure 2.2 demonstrates how, even at exposures below a full dose (7min in Figure 2.2), there is some degree of AuNS adhesion.

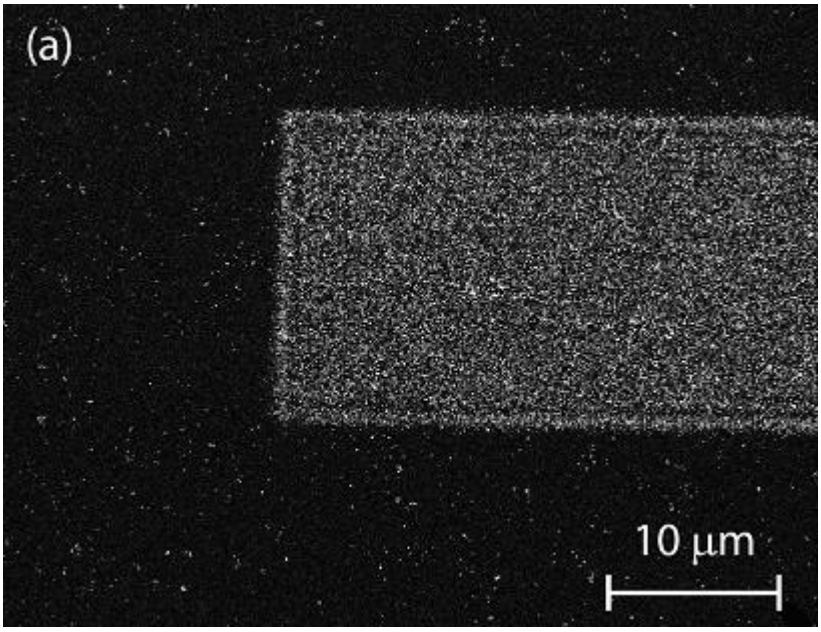

Figure 2.1: FESEM image of a gold substrate coated in 1, with AuNSs (bright spots) attaching to areas that have been exposed to UV light. From Daengngam et. al.[1]

Preliminary work on nanoparticle self-assembly was performed by Chalongrat Daengngam, showing that this ligand could bind to gold rods that had been deposited on a substrate. Following exposure to UV light, AuNS were bound to the AuNR via submersion into an AuNS bath. We will discuss his work more in-depth in Chapter 5.

In this thesis, we will demonstrate our ability to use this ligand to selectively bind gold nanosphere nanoparticles to other plasmonic nanoparticles in controlled configurations. By making use of the plasmonic hot spots generated by surface plasmon resonance and by the lightning-rod effect, we can create areas where the intensity of the light is much stronger than the overall incident intensity. By conjugating a plasmonic nanoparticle with **1**, then carefully

controlling the intensity of the incident light exposure, we can cause **1** to cleave into **1a** predominately at the plasmonic hotspots, leaving **1** nearly unaltered elsewhere. This, in turn, allows us to bind AuNSs only to the locations where **1a** is presentn demonstrating our ability to plasmonically direct the self-assembly process of the nanoparticles.

The synthesis of **1** was performed by Cheryl Peck and Xi Guo in the group of Dr. Webster Santos. The process is also detailed in Daengngam et al [1].

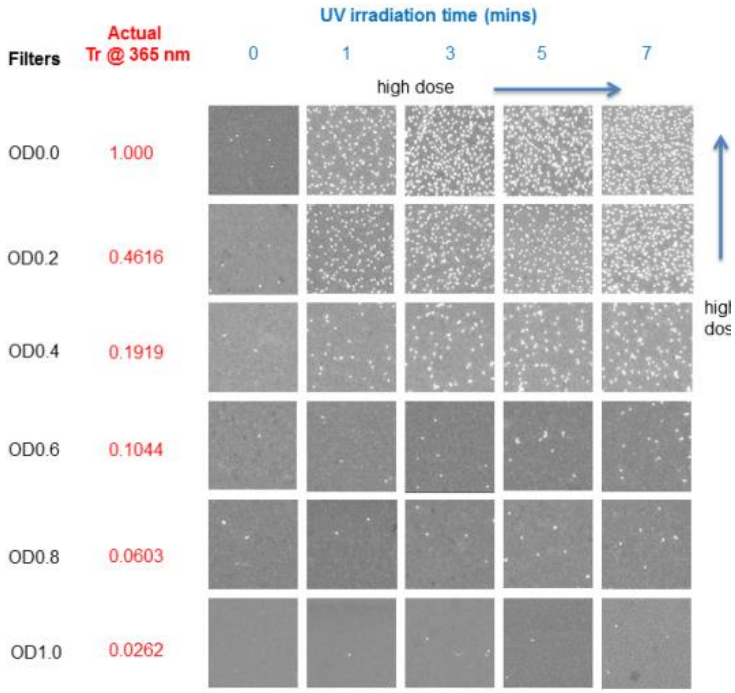

Figure 2.2: Comparisons of exposure dose and AuNS adhesion. Even at doses below a 'full' dose (7min at OD 0), AuNSs are still present. Taken from Daengngam's doctoral dissertation. [2]

2.2.2 Conjugation and SAM formation process

When conjugating **1** to a surface, it was important to perform the following procedure described below under red light or low-light conditions, in order to prevent inadvertent photocleavage of **1** into **1a.** The samples used were ~1" wide, for use with a five-slot staining jar, and no more than ~1" tall, for ease of submersion. They were originally carved from a 1"x3" microscope slide.

The following are the materials and vessels needed for this step. We will need one 10 mL vial of 2 mM **1** (in ethanol) stored a -17 ˚C, one clean glass vessel, one set of sample slides, and

200 proof ethanol. I frequently used a five-slot staining jar as a dedicated vessel for this process. We will also discuss how to make the various sample slides later in this chapter, in sections 2.4, 2.5, and 2.6.

The first step in this process was placing the samples in a clean glass vessel. While any clean glass container can be used, I frequently used a five-slot staining jar. I recommend strongly against using a freshly-acid-washed container, as such harsh cleaning methods are generally unnecessary except perhaps for the first use, and can interfere with SAM formation. Instead, one vessel was labeled as a dedicated container for conjugation with **1**, and cleaned via ethanol rinse immediately after each use. Immediately before the next use, it was filled with~20-30mL of ethanol and sonicated for 5 minutes. In between uses, this vessel was covered with parafilm to prevent dust infiltration.

In general, the samples used with this staining jar were ~ 1" wide (or else they would not be stable in the staining jar), and generally ~ 1" tall. By staggering the samples at angles, it was possible to fit up to nine samples in a five-slot staining jar without having any faces touching each other, except at discrete points. The schematic shown in Figure 2.3 helps further clarify this method of loading the staining jar.

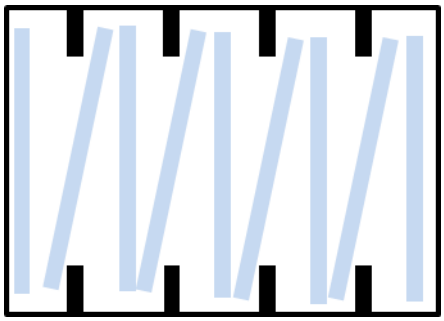

Figure 2.3: Top down-schematic of 1" wide glass slides in a five-slot staining jar. Specifically, this demonstrates the arrangement necessary to pattern nine samples at once.

Once the samples were in place, they were submerged in a 1 mM solution of **1** in ethanol. For 1"x1" samples in a five-slot staining jar, ~10ml was enough to fully submerge all samples. As **1** was provided in 2 mM concentrations, this was generally done by combining 5mL of **1** in ethanol with 5 mL of ethanol. Higher concentrations of **1** are fine to use, as generally we wished

to use the entire vial of **1** at once, as it does not keep well once opened. Slightly lower concentrations were also capable of forming SAM's on the samples, so long as the total concentration did not drop below 0.5 mM. Lower concentrations of **1** did take longer to form SAMs, however.

After the samples were submerged in 1 mM **1** in ethanol, the vessel was sealed with Parafilm. One corner was then lifted slightly, and argon was gently blown in through the opening for approximately three minutes. Afterwards, the container was resealed with Parafilm and further covered with aluminum foil to block any stray light. Alternatively, the sample was occasionally simply placed dark space. After 48 hours, the samples were removed and carefully double-rinsed in ethanol, using multiple tweezers to help prevent cross contamination. Afterwards, the samples were blown dry with dry nitrogen gas and placed in an opaque sample holder.

2.3 Gold Nanospheres (AuNS)

2.3.1 Synthesis and Characterization

AuNS were prepared via the Turkevitch method as outlined in Frens [3]. The synthesis requires the following materials: a 5 ml 1% (by weight) solution of sodium citrate, 2.5 ml of an aqueous 10 mM solution of gold (III) chloride trihydrate ($HAuCl_4 \cdot 3H_2O$), a glass flask filled with 97.5 ml ultrapure water, and a clean stir bar.

The 2.5 mL of the 10 mM $HAuCl_4$ solution were added to the beaker with 97.5 mL of ultrapure water. This resulted in a solution with a $HAuCl_4$ concentration of ~0.01% by weight. The beaker was then placed on a hot plate with a stirrer installed, covered with a flask lid, and heated to boiling. Once the solution was boiling vigorously, the stirrer was turned on at as high as possible while still keeping the beaker stable, and sodium citrate was injected into the rapidly stirring solution. It was important to make sure whatever amount of sodium citrate used is injected all at once, as quickly as possible. To create ~10nm diameter spheres, I used 2 mL of the sodium citrate solution. Less sodium citrate resulted in larger spheres, which is clarified further in the G. Frens paper.[3] Note that the G. Frens paper is based around making a 50mL solution

of AuNS, while the method just outlined results in 100 mL. After injecting the sodium citrate, the solution turned clear, then a very dark purple color, and finally slowly faded up into a reddish-orangish color. The flask was left on the heat to stir for ~20 minutes, and then removed from the heat and allowed to cool before being sealed with Parafilm.

There are two primary ways to characterize the nanoparticles. One is via spectrometry, which is described later in section 2.8.2, and reveals information about their resonance. The other is using dynamic light scattering (DLS) and zeta potential measurement system, which gives information regarding the particle size and electric surface potential. As using a DLS and zeta potential system requires specific training, further instruction is beyond the scope of this dissertation.

2.3.2 AuNS Conjugation Methods

Primarily, we use AuNSs to bind to **1a**, both to assemble nanoscale structures and as a straightforward method of visualizing where **1a** is present on a sample. There are two primary methods of introducing our samples to AuNSs: drop casting and submersion. In both cases, the pH of the AuNS suspension should be adjusted to ~5.7, as **1a** becomes positively charged in this pH range. However, if the AuNSs were recently synthesized, pH adjustment is probably unnecessary, as the solution's pH at synthesis should be close to the required level. Over time, the solution will slowly drift towards a more neutral pH (7), necessitating the addition of small drops of HCl to readjust the pH balance.

I) <u>Dropcasting</u>

Dropcasting is best suited for situations where we don't care if all areas with **1a** present are conjugated to an AuNS, but when we do care more about the overall pattern of adhesion. Alternatively, it is also useful when very large areas have been photocleaved into **1a.** For this reason, we will use it frequently in Chapter 3, where we care about the overall patterning of specific areas, rather than making sure AuNSs adhere everywhere on the sample where they are able to adhere. It is best suited for short deposition times—when using the dropcast method, long deposition times can result in the AuNS suspension evaporating, leaving AuNSs deposited on the surface even in areas where no **1a** is present.

Dropcasting gold nanospheres is a fairly simple affair: A solution of AuNSs (concentrated with centrifugation or as-synthesized) is deposited dropwise onto the sample, until the desired area is covered in the AuNS solution. In general, surface tension keeps the droplet resting on the sample. But care must be taken to not overload the sample—if too much AuNS solution is added, the droplet may run off the edge of the sample and wick under it, both greatly reducing the amount of AuNS solution present on the surface and putting the system a risk for drying out. Once this is done, the sample is covered and left to incubate in darkness for about thirty minutes to one hour, before being removed and rinsed thoroughly in deionized water.

If using drop-casting for long time periods, it is important overnight, to seal the samples in an airtight container with a small beaker of water also placed inside the container. This is to prevent the AuNS solution from drying out. Allowing the solution to dry out will invalidate the sample, as AuNSs will appearing to adhere to the surface regardless of the presence of **1a** or not.

II) <u>Submersion</u>

Submersion is better suited for situations where small areas have been photocleaved into **1a**, such as the tips of nanorods, or small sections of a nanosphere—circumstances where we want the AuNSs solution in contact with the sample surface for an extended period of time, to ensure the AuNSs have time to encounter and bind to as many instances of **1a** as possible. For this reason, submersion will be our primary method of AuNS application in Chapters 4 and 5.

Submersion is somewhat more difficult than dropcasting. First, the samples are placed into a clean glass container, such as a staining jar or small beaker. If the container in question was acid-cleaned, it must be thoroughly rinsed multiple times with DI water before the introduction of the sample. Afterwards, a AuNS suspension is poured over the sample(s) until completely submerged. They can then be left as long as a day or even a week, before being removed, rinsed thoroughly in DI water, and blown dry with compressed air.

2.4 Gold Nanorods (AuNRs)

2.4.1 AuNR Synthesis

Prior to synthesis, the following components were either located or prepared: 150 ml of a 0.1 M cetyltrimethylammonium bromide (CTAB) solution (5.46678 g CTAB in 150 ml of water) heated to (and kept at) 28 ˚C, five clean 25ml beakers, 5 small stir bars, at least 4.25 ml of 10 mM Aqueous $HAuCl_4$ solution (0.03939 g in 10ml of water), at least 2 ml of 10 mM aqueous $AgNO_3$ (0.0169 g $AgNO_3$ in 10 ml water), at least 2 ml of 0.1 M aqueous L-Ascorbic acid solution (0.17612 g L-Ascorbic acid in 10 mL water), at least 5 ml of 0.1 M HCl, and a freshly prepared 10 mL solution of 100 mM aqueous $NaBH_4$ (0.0378g in 10 mL), which is immediately into a 10mM solution immediately before use The $NaBH_4$ must be prepared using ice cold water, or it will not work. Furthermore, the $NaBH_4$ should not be prepared until immediately prior to its use, once everything else has been assembled and set up. The $HAuCl_4$ solution can be stored for up to two months.

This method relies on the formation of gold nanorods from gold 'seeds' in a growth medium. In darkness (or under red light), 0.25 mL of 10 mM $HAuCl_4$ was added to a 10 ml aqueous solution of 0.1 M CTAB under vigorous stirring. After 1 minute, 600 µL of 10 mM $NaBH_4$ was added. The solution was then left to stir in darkness for 15 minutes, while kept at ~30˚C. Afterwards, the resulting seed solution was removed from stirring.

Under gentle stirring (60rpm) 1 mL of 10 mM $HAuCl_4$ was added to 20 mL of 0.1 M CTAB and 0.100-0.140 ml of 10 mM $AgNO_3$ kept at 30˚C and left to stir. After one minute, 400 µL of 1.0 M HCl and 160 µL of 0.1 M L-Ascorbic acid was added. Then, 48 µL of the previously synthesized seed solution was injected into the mixture. The entire procedure was done under gentle stirring (60 rpm) at ~30 ˚C in darkness (sealed with tinfoil, for instance) for 3 hours.

The ratio of $AgNO_3$ to $HAuCl_4$ used can determine the final nanorod size, and thus the desired nanorod resonance—the higher the ratio of $AgNO_3$, the longer the rods the rods will be, up to a point. This is explored in depth in Alekseeva et al [4], which also looks at how the starting seed size can alter the AuNR growth, and is an excellent resource for AuNR synthesis. As the process is somewhat difficult to control, and relies on precise ratios, it is difficult to

predict exactly how much $AgNO_3$ should be used. Therefore, it can be prudent to perform three or four nanorod synthesis at once, varying the amount of $AgNO_3$ in each vial.

2.4.2 Characterization

AuNRs are best characterized via spectrometry. To characterize the as-synthesized suspension, it must first be heated to 30˚C to fully dissolve all the CTAB, then slightly diluted before being placed in a microcuvette. When properly formed, the AuNRs have two distinct absorption peaks, corresponding to resonances polarized along the longitudinal and transverse axis of the nanorod. In the figure below (Figure 2.4), the transverse resonance is located near 520nm, while the longitudinal resonance, which is substantially stronger, occurs at lower wavelengths. The precise location of the longitudinal resonance is determined by the nanorod aspect ratio. A sample spectrum is provided below. In my work, I tended to aim for nanorods with a longitudinal resonance of ~740nm**,** as that range was deemed most likely to work for two-photon absorption (see Chapter 5) photocleaving of **1**. Qualitatively, these rods tend to have a purplish-red coloration, but sometimes will also appear brownish.

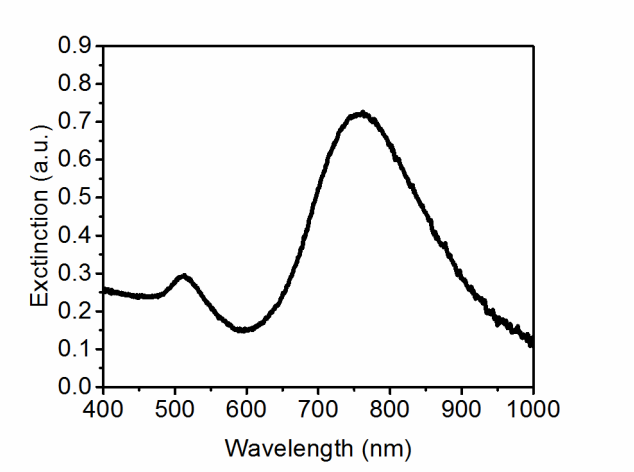

Figure 2.4: Sample extinction spectrum for a batch of AuNRs synthesized via the method outlined in Chapter 2.4.

2.4.3 Deposition on Surface and Sample Preparation

Depositing the AuNRs on a surface requires two different processes: wrapping the AuNRs in Poly(sodium 4-styrenesulfonate) (PSS), which gives them a stable negative charge, and creating a positively charged sample substrate to deposit the AuNRs on. The two processes should be run in parallel, such that they finish at approximately the same time. Otherwise, either the AuNRs or

the sample substrate may lose some of their charge, and the AuNRs may not properly adhere to the surface. Two methods of preparing positively charged substrate surfaces will be detailed here: using silane, and using poly(allylamine hydrochloride) (PAH). We have had the best success with PAH, however both methods are included for completeness.

I) Wrapping Nanorods in PSS

Wrapping the nanorods in PSS requires the following materials: One 2 ml flask or beaker with stir bar, a 5 mL 5 mM (monomer basis) aqueous solution of PSS, and one clean centrifuge tube. The PSS solution should be prepared one day prior to PSS-coating the AuNRs, in order to ensure the PSS has had enough time to fully dissolve.

1 mL of the AuNR solution was placed in a centrifuge tube and heated to 28 ˚C to fully dissolve the CTAB present in the sample. Temperature was kept below 32 ˚C, as excess heating can cause deformation of the AuNRs.

To remove excess CTAB, the sample was then centrifuged at 2500 RCF for 12 minutes, after which 95-98% of the supernatant was removed and replaced with water. The sample was then sonicated for up to 30 s to re-suspend the nanorods in the solution. It is important to not sonicate the nanorods longer than thirty seconds—excess sonication can cause heating that will cause the nanorods to deform. The centrifugation was then repeated. Again, 98% of the supernatant was removed and replaced with water, after which the sample was sonicated to re-suspend the nanoparticles.

After the centrifugation, the 1 ml of nanorod solution was placed into a small beaker with 0.150 mL 5 mM PSS and stirred vigorously for 30 s. After 30 s had elapsed, the solution was stirred slowly for an additional two hours. A small portion (~100 μL) was removed and diluted to check the spectra again, to determine whether the nanorods were still present and undamaged.

II) Creation of a charged substrate surface

Here we discuss the two surfaces that the AuNRs can be easily deposited on: a PAH surface, and a silane surface. Either glass or silicon substrates can be prepared via these methods. Depending on the exposure method used, it may also be prudent to create ‘guide marks’ on the surface—reference points for methods of exposure that will expose only a small surface area of the

sample. This can be done with a diamond scribe, carefully etching a specific line and orientation symbol in the surface. This should be done under water, to reduce glass or silicon debris generated in the process, and is outlined further in Chapter 5.

i) Aminopropyl Triethoxysilane Surface

Functionalizing the substrates with silane requires anhydrous toluene and (3-aminopropyl)triethoxysilane (APTES). The toluene was acquired from Dr. Santos group in Davidson, while the APTES must be drawn from its container using a glass syringe.

The sample substrates were cleaned in aqua regia for 10 minutes, then rinsed thoroughly with water. Afterwards, the slides were sonicated in acetone, then in methanol, and then blown dry with dry nitrogen gas. The slides were then placed in a beaker that was dedicated to this silane-coating process, such that no two faces of the substrates were touching each other. The beaker was then placed in a heated oven and baked at 120 ˚C for 10-20 minutes to reduce surface moisture. After removal from the oven, the beaker was filled with *anhydrous* toluene until the sample was halfway covered. Then, 0.1 ml of APTES was added for every 10 ml of toluene that would ultimately be used (for example, I frequently used 40 ml of toluene in total, so I added 0.4 ml of the silane after 20 ml of toluene had been added). The solution was then stirred gently by hand using a swirling motion for 30 seconds, after which the remaining toluene was added until the samples were completely submerged. At this point, the beaker was covered with either another larger beaker or a petri dish. It is imperative *not* to use parafilm to cover the silane solution—the toluene fumes will weaken or dissolve the parafilm, which will fall into the beaker and ruin the substrate.

After 15 minutes, the toluene/silane mix was drained into a waste bottle, and the samples, still in the beaker, were rinsed briefly with anhydrous toluene. The beaker was then placed back in the oven and baked for an additional 1 hour at 120 ˚C. Afterwards, it then was removed from the oven and subsequently sonicated in baths of pure toluene, a 50/50 toluene/methanol mix, and pure methanol. After removal from the methanol, the samples were blown dry, and ready for PSS-coated AuNR deposition.

ii) PAH-Coated Substrates

This method is swifter than the silane method, but is also heavily dependent on the pH adjustment of the PAH. The PAH surface method requires a 10mM (monomer basis) PAH solution of a large enough volume to fully submerge a slide (generally 100-200 ml). This solution must be prepared at least 12 hours in advance to give the PAH time to fully dissolve, and is adjusted to pH 7 immediately prior to use.

The substrates were cleaned by immersion in aqua regia for 15 minutes, then rinsed thoroughly with DI water and blown dry. Afterwards, the slides were immersed in the PAH solution for approximately 10 minutes. They were then removed and blown dry with a stream of dry nitrogen gas.

III) Deposition and Preparation.

Once both PSS-wrapped AuNRs and positively-charged substrate were prepared, AuNRs were deposited on the surface. First, the PSS-coated AuNRs were placed into a centrifuge tube and centrifuged two more times at 2500 RCF for 12 minutes, each time removing 95% of the supernatant fluid, replacing it with ultrapure water, and sonicating the centrifuge tube. This is done to remove excess PSS that did not bind to AuNRs. If this is not done properly, free PSS will quickly bind to any positively charged substrate before the rods have a chance to do the same, preventing AuNR adhesion.

The prepared nanorod solution was then diluted at a 1:1 ratio with water. Once diluted, the solution was drop-cast onto the prepared slides, then placed under a cover and allowed to incubate overnight. A small beaker of water was also placed inside the enclosure with the prepared substrates, to raise the ambient humidity and prevent the AuNR solution from drying out. This allowed the negatively charged nanorods to adhere to the positively charged surface. After deposition, the samples were removed, rinsed with water, and blown dry. At this point, one of the glass substrates was characterized in the spectrometer, to make sure that AuNRs had indeed adhered to the surface—if they had, a spectra similar to that of AuNRs in solution, except slightly blue-shifted due to the lower index of refraction of air compared to water, would be present.

Afterwards, the samples were placed in an ozone cleaner for ~20-40 minutes. This process removed both PSS from the nanorods, as well as the organic silanated/PAH film surrounding the nanorods. The time needed will vary—PAH needs less time in the ozone cleaner than silane. However, the ozone cleaner itself may also lose power over time. In order to account for this, when first attempting this process, it is important to try numerous different ozone-cleaning times and checking the AuNR sample spectra afterwards, in order to determine the optimal cleaning time.

Too little ozone exposure results in an excess of positively charged PAH or silane left on the substrate. This, in turn, allows the negatively charged AuNSs to bind to it, even in the absence of **1a**. Continued ozone exposure results in the continued removal of PSS and PAH or silane until only the areas beneath the nanorods are left, keeping them bound to the surface. Continued ozone cleaning past this point begins to strip that away as well, resulting in the removal of the AuNRs from the sample surface when it is next immersed in fluid.

2.5 Tollens Surfaces

2.5.1 Tollens Synthesis

The Tollens reaction allows for the quick creation of silver nanospheroids (AgNSs) on a glass substrate with relative ease. Like gold, silver nanostructures have strong plasmon resonances. The Tollens surface's resonance lies within 350 nm-450 nm range, making it potentially useful for the purposes of controlled self-assembly when conjugated with **1**.

Prior to the synthesis itself, several glass microscope slides should be prepared as the substrates. If the slide is to be broken into smaller samples, it is important to scratch the break lines in with a diamond-tipped pen *prior* to cleaning. The same goes for any markings that will serve as labels. After marking, the glass slides should be cleaned with aqua regia in a staining jar and left to sit for ten minutes. Afterwards, the aqua regia is removed, replaced with ultra-pure water, which is then removed and replaced two additional times, with the water left in place after the final rinse. It is important to make certain these glass slides are cleaned with aqua regia shortly before synthesis, or the Tollens substrate may not adhere properly.

The synthesis itself requires two tall (~150 ml-200 ml) beakers of ultrapure water, one disposable centrifuge tube, 1 mL of a 0.8 mM aqueous solution of potassium hydroxide (KOH), ~1 mL of ammonium hydroxide (NH_4OH) combined with ~1 mL of water, a 1.9 M stock solution of glucose, and 3 mL of freshly prepared 1 mM aqueous silver nitrate ($AgNO_3$). The $AgNO_3$ should be prepared in a dedicated glass vial with a dedicated stir bar. It is important not to clean this vial with aqua regia between uses except when absolutely necessary, such as when the entire interior becomes silvered or after contamination by reagents not used in this experiment. Cleaning the vial with aqua regia tends to cause the next synthesis performed using it to fail. While a quick rinse with diluted NH_4OH can help prevent such failure (if it has been recently acid cleaned), this has not prevented failure in all cases. Generally, the vial was cleaned solely via thorough rinsing with water immediately before and after each synthesis.

The sample preparation process is based upon the synthesis described in Wang et al [5]. The $AgNO_3$ vial was placed on a stir plate under gentle stirring, and diluted NH_4OH was added dropwise to the $AgNO_3$ until a brown precipitant formed. Once formed, further NH_4OH was added until the precipitant dissolved again. Next, 1 mL of 0.8 M KOH was added, resulting in a black precipitant. Again, NH_4OH was added until the precipitant dissolved.

Next, a cleaned glass substrate was removed from the water bath, blown dry, and placed (label side up) on a clean, absorbent surface inside the fume hood--either fresh fume-hood paper, or a few layers of kim wipes.

Then, 0.2 mL of the 1.9 mM glucose solution was added to the centrifuge tube, followed by 0.55 mL ultrapure water. This dilutes the glucose solution to 0.5 mM. Then, 0.75 mL of the solution in the $AgNO_3$ vial was added to the disposable centrifuge tube. The lid was then capped, shaken rapidly for ~2 seconds. Afterwards, the solution inside was quickly pipetted onto the glass microscope slide. Typically, it was allowed to incubate for 75 s. Allowing it to sit for longer resulted in larger (and more densely packed) spheroids, while a shorter dwell time resulted in smaller spheroids. Qualitatively, the longer the solution is allowed to sit, and the larger the spheres are, the more brown the glass substrate will appear. After the desired dwell time was reached, the sample was picked up and rinsed consecutively in both water baths, halting the reaction—separate tweezers do not need to be used for each bath. Afterwards, it was

blown dry and set (face up) on another clean surface. This was repeated until all glass substrates had been processed.

To test whether the Tollens surface had properly adhered to the glass, a drop of water was placed near the corner of one of the substrates to see if the Tollens surface would remain on the glass surface. If the glass slide was not sufficiently charged or cleaned prior to synthesis, then this can cause the silver to lift off from the glass, indicating that the substrates are not suitable for further use.

Immediately after synthesis, the samples were gently rinsed with ethanol, then conjugated with **1,** following the procedures outlined in section 2.2.

2.5.2 Properties

This synthesis process resulted in a glass substrate covered in AgNSs, with diameters ranging from 20 nm to 100 nm. Qualitatively, the Tollens-conjugated samples that worked best in the experiments had a transparency similar to that of colored saran wrap, and a yellow to yellow-brown color. This allowed for good visual contrast between areas that had been conjugated with AuNS and those that had not. Its transparency also allowed for easier spectroscopy. Halting the reaction earlier resulted in smaller spheres, and a fainter, more yellow color. Halting the reaction later resulted in a more brown and opaque substrate. Quantitatively, the Tollens samples could have absorption peaks ranging from 350 nm to 450nm, depending on when the reaction was halted. A spectrum of a Tollens sample made by this process is shown in Figure 2.5.

These samples will slowly oxidize after formation, so measurements must be performed (or re performed) within a few months of the experiment. Storage in a dry box may prolong their life, however.

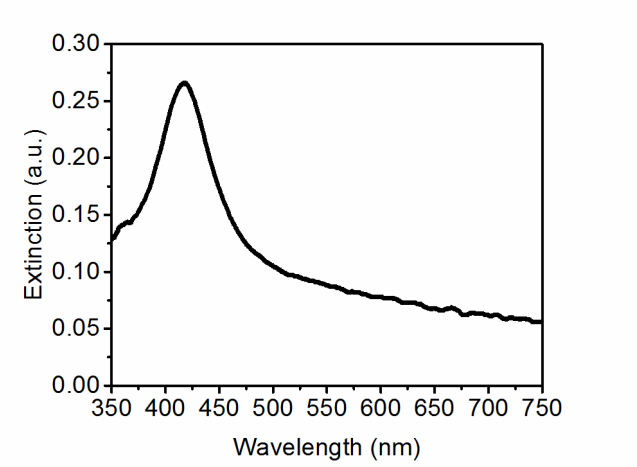

Figure 2.5: Sample extinction spectrum for Tollen's sample synthesized via the method outlined in Chapter 2.5.

2.6 Continuous Metal Films

2.6.1 Continuous Metal Film Uses

Continuous metal films can be used to determine whether or not a reaction or effect is plasmonic in nature. If the reaction (or effect) If the reaction or effect can proceed on a thick metal film as easily as it can on a thin film, or on a nanoscale surface, then it is likely not plasmonic in nature. If it does not proceed as easily on a thick, continuous metal film, then that suggests the effect *is* plasmonic. Plasmons are not as easily generated on a thick metal film, and they decay more quickly than on a plasmonic nanoparticle, causing thick metal films to have far less plasmonic enhancement than nanoparticles of an identical metal. This is due to thick metal films being less plasmonically available, and less capable of strong plasmon resonance.

2.6.2 Preparation and Synthesis

As with most sample substrates, this requires cleaned microscope slides to be prepared prior to use—the exact method cleaning, however, is not critical. Other necessary components include an electron-beam evaporator (or other method of depositing a thick metal monolayers), and the requisite metals for evaporation. In our case, we will use titanium (Ti) as an adhesion layer for glass slides, and silver (Ag) or gold (Au) for the continuous metal film layers. We will not describe the training required for electron beam evaporation here, as it is beyond the scope of this dissertation.

The process is rather straight forward. For glass slides, a 5nm Ti adhesion layer was evaporated onto the glass, followed by either an Ag or Au layer, depending on the material and thickness desired. For thick films, it is best to use a slow deposition time, in order to make it as smooth as possible. The process for evaporating onto silicon is identical.

2.7 Exposure Methods

In order to perform controlled self-assembly, we must first cleave **1** into **1a**. We accomplished this in one of several ways.

2.7.1 Unpolarized UV light (UV Crosslinker):

The UV crosslinker is used to expose a sample to unpolarized UV light. This might be to act as a control, comparing fully cleaved regions to areas with more selective photocleaving. Alternatively, it might be to explore an effect that requires photocleaving **1** into **1a** to proceed, such as in Chapter 3.

UV Crosslinker exposures were performed in a FB-UVXL-1000 UV Crosslinker fitted with a bulb with an emission maximum at a wavelength of 365 nm (It is important to note that this is *not* the original bulb). Samples were placed face up in the center of the UV Crosslinker (marked with a black X in pen), and then exposed for the desired time/dosage. Typically, exposures were typically 1 J/cm^2 in order to fully photocleave all **1** into **1ab,** or about 15 minutes of exposure with a 365 nm light bulb.

2.7.2 Green (550 nm) Light Exposures

Green light (~550 nm) exposures were generally performed for one of two purposes. The first purpose was that a green-light exposure, prior to any other photocleaving attempts, will reduce the amount of non-specific AuNS binding, making it easier to determine whether or not a particular approach worked. For this reason, most of my samples were exposed to green light prior to other exposures, to reduce the amount of non-specific binding. The second possible reason to do a green-light exposure is to remove the ability of an area of **1a** to bind AuNSs to itself. This effect is discussed further in Chapter 3.

Green light exposures were performed with a Mercury-Xenon white light source and a 550 nm green light filter with a 10 nm bandwidth (Andover Corporation's 550FS-10), using the optical setup shown schematically in Figure 2.6, resulting in a dosage strength of ~1 mW/cm^2. Typical green light doses were on the order of 2 J/cm^2, requiring an exposure time of approximately 30 minutes.

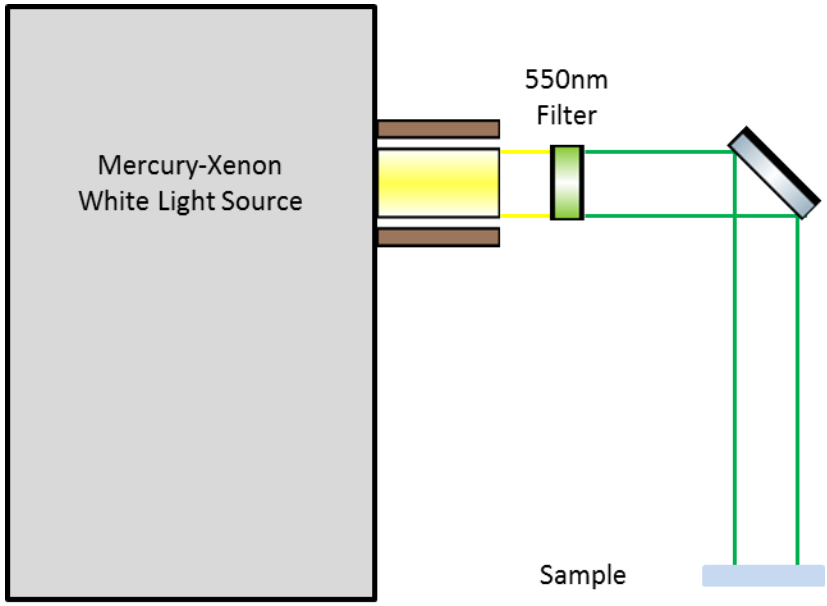

Figure 2.6: Schematic of the green light exposure setup.

2.7.3 Ultrafast Femtosecond Pulsed Laser 730nm Laser

The ultrafast femtosecond laser was used for non-linear photoexposures—that is, exposures intending to use multi-photon absorption (See Chapter 5.3 for more detail) in order to photocleave **1** into **1a.**

This was done by using a Chameleon Ultra II TI: Sapphire laser, with a pulse width of 140fs and a repetition rate of 80 MHz as the source. The laser was brought through a circular polarizer into a Zeiss LSM 510 laser-scanning microscope, and focused onto the sample by a 20x or 2.5x objective, with the sample in either air or a mixture of Isopropyl alcohol and HCl. In order to either image or pattern a sample, the LSM was programmed to scan the laser beam over a pre-programmed region, varying the speed and exposure levels based on the operator's choice.

2.7.4 UV Laser

A UV laser was used in place of a UV-Crosslinker to obtain exposure with *polarized* UV light. I will discuss such experiments in Chapter 4.

UV laser exposures were provided by a 376 nm 60 mW vertically polarized laser. In order to reduce the power and expose an area wider than the beam, the laser was brought through a 0.6 OD filter and into a Thor Labs BE02-05-A10x beam expander broadening the spot size to ~10mm in diameter, providing a peak power of 76.4 mW/cm^2. By using a programmable shutter, we were able to control precisely what dosage each sample received. A schematic of the setup is shown in Figure 2.7

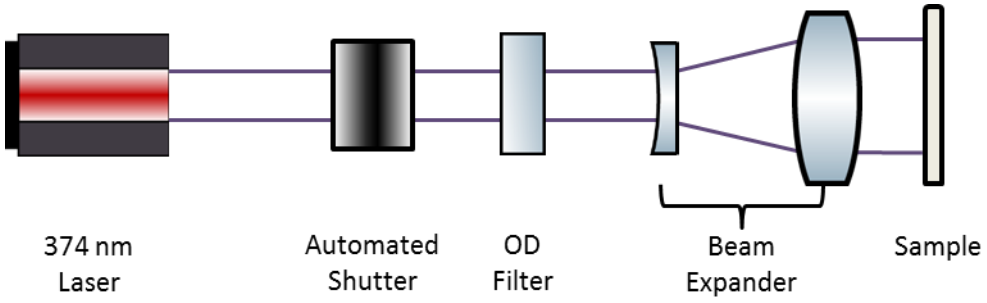

Figure 2.7: Schematic of UV-Laser exposure setup

While exposing the sample with a well-defined dose is important, so too is knowing *where* the sample was exposed—unlike with UV crosslinked samples, only a portion of the sample exposed to the polarized UV laser will receive exposure. For this purpose, I made an 'alignment sample' to make certain I knew exactly where the laser was striking on every sample placed in the sample holder. This simply consisted of a glass slide marked with a sharpie of the same size and shape as the samples used. It was placed in the sample holder and used to align the laser to the marked spot. Later, this dummy sample was used as a reference to determine where on every sample the laser had struck.

2.7.5 Shadowmasked Exposures

In some cases, it's helpful to have areas of different exposure on the same sample, in order to better compare and contrast different exposure types without having to worry about the differences between samples. To do this, we used a shadow-mask to cover certain areas of a sample whilst leaving others exposed. The mask is simply a brass sheet with ~3.5 mm wide

parallel sections cut out of it, 3.5 mm apart. This create alternating bands of brass and empty space at 3.5 mm intervals. This allowed us to expose select areas of the sample to a specific optical dose, while keeping other parts covered and in shadow. Shadow mask exposures were therefore generally used with green light or the crosslinker. The shadowmask used in this thesis should not be confused for a photomask, which produce micron-scale or nano-scale patterns for photopatterning—our shadowmask is a far simpler, macroscale construction.

2.8 Characterization Methods

In the course of my research, I used several methods to characterize the various samples I created. I have included both the methods I used, as well as brief explanations for measurements they would be suited for.

2.8.1 FESEM Imaging

Field-emission scanning electron microscopy can be used to directly image samples at much higher resolutions than an optical microscope is capable of delivering. This is useful when one is looking for specific structures on a surface, such as nanospheres sticking to the ends of nanorods. Multiple FESEM images a surface can also be used to perform statistical calculations for how effective a particular technique is (rate of nanosphere adhesion for a particular technique, etc.). It can also be used to confirm and support spectroscopy results, or used on opaque samples, where spectroscopy cannot be used.

Generally, if one intends to take FESEM measurements, a silicon substrate can be more useful than a glass substrate, unless one also needs to take spectroscopy data. As silicon is naturally conducting, silicon substrates can be placed directly into the FESEM without further processing (assuming that the materials deposited are also conducting). If glass substrates must be used, then it is necessary to sputter carbon or gold onto the samples to render them conducting.

2.8.2 Spectroscopy

Optical spectroscopy can be useful in determining general trends about the plasmonic sample under study—for instance, whether or not gold nanospheres have adhered to a surface, or to a

particular portion of a surface. This is done via observing shifts in the spectrum that come about due to interactions with and between plasmonic modes. This is explained in more detail in the Discussion section of Chapter 3.

UV-VIS spectrophotometry was performed using an Ocean Optics H2000CG-UV-NIR spectrometer. The system's white light source was provided by a Mikropack DH-2000 source box that is brought through a fiber optic cable and passed through a collimating lens. The light is then brought through the sample—whether a fluid inside a microcuvettte, or a glass sample slide resting in (or atop) a sample holder—and back through another, identical collimating lens, condensing the beam back into a second fiber optic cable, which is connected to the spectrometer.

2.8.3 Rotational Spectroscopy

Rotational spectroscopy is a variant of spectroscopy that is useful for detecting aligned anisotropies on a transparent sample substrate. In rotational spectroscopy, a polarizing filter is put in-line with the sample, and either the polarizer or the sample are rotated around the optical axis of the system, allowing one to observe how the spectra changes as the angle between polarizer and a defined axis on the sample changes. If a sample is purely isotropic (or randomly anisotropic), then either the spectrum will show no major shift as the angle between the polarizing filter the sample changes (if the sample is isotropic), or it will shift randomly with no discernable pattern (if the sample is randomly anisotropic). If, however, there are aligned structures or some other source of anisotropy present on the sample, then the spectrum presented may change in a defined, recognizable pattern. This is further explained in Chapter 4.

In the work presented in this thesis, rotational spectroscopy was performed using a modified Filmetrics F10-VC system. The sample was attached to a rotating stage, and placed in-line with a stationary Edmund Optics wire mesh 400-1200nm polarizer (product #33-082), in order to measure the sample's absorption as a function of its orientation with respect to the polarizer. The rotational stage was then connected to a secured X-Y positioning platform by means of a physical adapter, allowing us to center rotational stage in the beam path of the Filmetrics system. A schematic of the setup can be seen in Figure 2.8.

In an ideal setup, we would use a fixed sample and rotate our polarizer, as opposed to what we have shown in Figure 2.8, where the sample is attached to the rotating stage. This is because the polarizer is far more uniform than the sample—even if the system's center of rotation were not coincident with the optical axis of the beam, it would not greatly affect the system. However, the light provided by this Filmetrics device has a minor degree of polarization, which means that we were forced to keep the polarizer fixed in place in order to account for this, meaning we must rotate the sample, instead. This, in turn, means that axis of rotation of our stage must be maintained as close as possible to the system's optical axis.

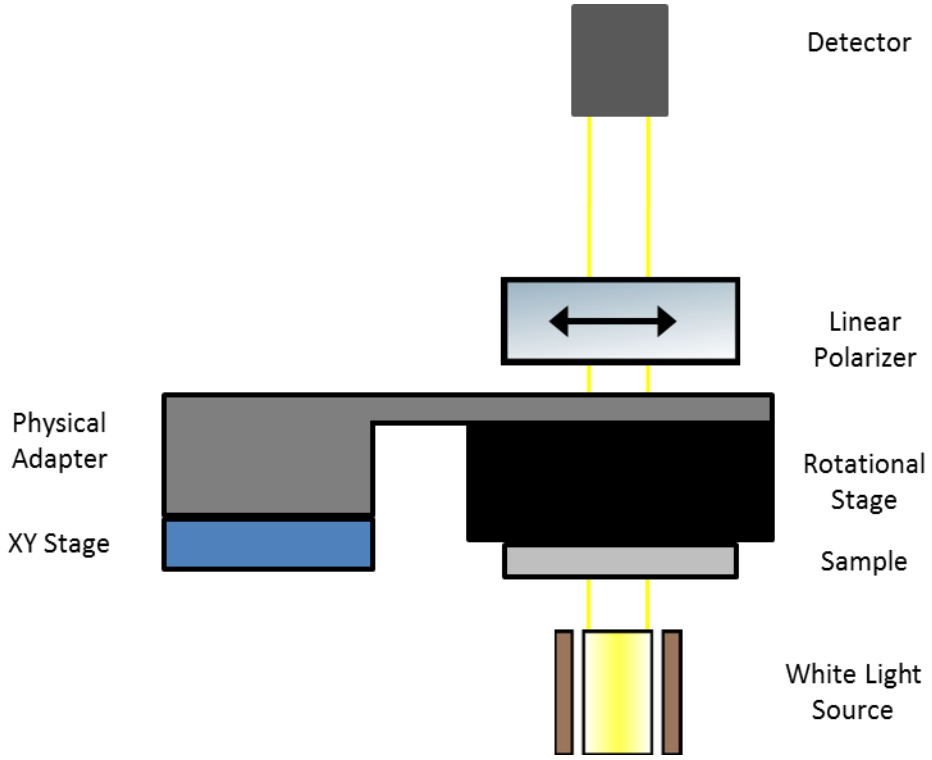

Figure 2.8: Schematic of rotational spectroscopy setup

To achieve such concentricity, a sample was placed in the sample holder and moved into the beam path, with initial centering done by visual estimtion. Then, the transmission spectra through the sample was measured for four different orientations: 0˚, 90˚, 180˚, and 270˚. If the sample was centered, orientations 180˚ apart (0 and 180, 90 and 270) would have identical transmission spectra. If these spectra were not nearly identical, this indicated that the sample was

not centered. Adjustments were made, and the process was repeated until the axis of rotation was as close to the center as reasonably possible.

Once centered, the samples were characterized by rotating them and measuring the transmission spectra in 10˚ intervals. Some of these measurements were graphed as extinction spectra, via taking the negative log of the transmission measurements ($-\text{Log}(I/I_0)$). More detail on this can be found in Chapter 4.

Chapter 2 References

[1] C. Daengngam, S. B. Thorpe, X. Guo, S. V. Stoianov, W. L. Santos, J. R. Morris, and H. D. Robinson, The Journal of Physical Chemistry C **117**, 14165 (2013).
[2] C. Daengngam, Dissertation, Virginia Polytechnic Institute and State University, 2012.
[3] G. Frens, Nat Phys Sci **241**, 20 (1972).
[4] A. Alekseeva, V. Bogatyrev, B. Khlebtsov, A. Melnikov, L. Dykman, and N. Khlebtsov, Colloid Journal **68**, 661 (2006).
[5] Z. Wang, S. Pan, T. D. Krauss, H. Du, and L. J. Rothberg, Proceedings of the National Academy of Sciences **100**, 8638 (2003).

CHAPTER 3

3 Plasmon-Induced Photoreaction of *o*-Nitrobenzyl Based Ligands Under 550nm Light

This chapter represents work that has been submitted to Phys Chem C, but not yet published. It has been altered to fit formatting requirements. Supplementary information mentioned in this chapter is not included, as it is either replicated elsewhere in this work (Mie theory: Section 4.2.8), or not relevant to the dissertation.

3.1 Abstract

We studied the plasmon-driven photoreaction of a dual thiol-anchored *o*-nitrobenzyl-based photouncaging ligand on silver nanoparticles. Previous results have shown that this compound strongly anchors to gold surfaces, and a 1 J/cm^2 dose of UV light induces the intended photoreaction, uncaging an amine on the surface. This allows for photopatterning and the selective adhesion of gold nanospheres (AuNSs) to a surface via electrostatic attraction between the positively charged amines and negatively charged AuNSs. Here, we report that when the ligand is adsorbed on a silver nanospheroid film (AgNS), an additional photoreaction induced by green light which inhibits AuNSs adhesion in the UV exposed film. Our finding suggest that this is a result of the neutralization of the amine group's ability to become charged, as opposed to the removal of the ligand from the surface of the silver nanospheroids. We hypothesize that this neutralization may be due to a form of hot-hole induced photocatalysis resulting in an N=N double bond between two neighboring ligands. This reaction has been documented in similarly amine-terminated moieties. This neutralization allows for a more fine-tuned, plasmonically based control of the ligand's photoreaction, as the green light exposure only affects the ligand if it has

previously been cleaved by UV light, and makes it possible to peform reverse photopatterning on the surface.

3.2 Introduction

An extensive and broad range of photochemistries have been studied for the purpose of direct photopatterning on photoreactive self-assembled monolayers (or SAMs) [1-4]. Some of these include the optical breaking of Si–C bonds [5], metal-sulfur bond oxidation [6], 7-nitrodine [1], aryl ester [7], and (coumarin-4-yl)-methyl [3], among several others. Of particular interest to us are *o*-nitrobenzyl based ligands, which have seen a great deal of study [8-13].

Photoreactive SAMs are of particular interest in plasmonics. Plasmonics applications generally take advantage of the ability of plasmon resonance in metal nanostructures to concentrate light into nm-scale regions, known as hot spots, that tend to occur at sharp corners or in narrow gaps in the nanostructures. At these locations, the light intensity can be orders of magnitude higher than elsewhere on and near the structures [14]. Photoreactive SAMs make it possible to selectively modify the surface properties at the hotspot, which could then be used to affect nanoassembly in new ways, or to enhance the efficiency of surface-enhanced Raman spectroscopy (SERS) substrates, which rely on the adsorption of analytes on plasmonic hot spots.

Plasmonic effects can also affect reactions on, or adjacent to, a metal nanostructure. This occurs through non-radiative (or dark) decay of plasmon modes into hot carriers that are either injected into or excited within molecules on or near the metal surface [15-17]. The charge carriers are denoted hot because their energy distributions are characteristic of a thermal temperature well above ambient. The two primary mechanisms of this hot-carrier transfer are detailed in Figure 3.1. These are chemical interface damping (CID, Figure 3.1a) and hot carrier generation (Figure 3.1b).

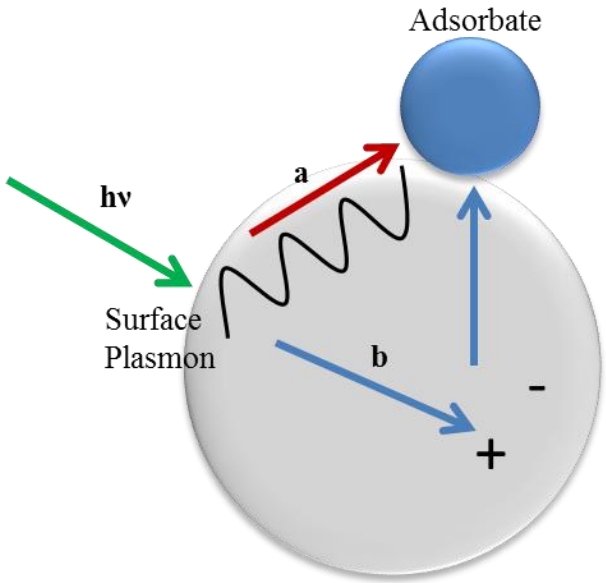

Figure 3.1: Two possible sources of hot carrier transfer. a) Chemical Interface Damping (CID), in which the plasmon decays via injecting a hot carrier directly into an adsorbate site b) Hot carrier injection, in which a plasmon decays into a hot electron/hole pair, which can then travel into an available adsorbate site.

When damped by CID, the plasmon wave decays via interaction with a moiety adsorbed on or near the surface. The collective plasmon excitation interacts with the unoccupied states in the adsorbate and decays by inducing a discrete excitation into these states. The net result of this process is the population of an excited state in the adsorbate [18-20].

Hot carrier injection is slightly more involved. In this process, the plasmon wave decays into a high-energy electron-hole pair within the metal band structure. These hot carriers have a very short lifespan, decaying on the order tens of femtoseconds, dissipating most of their energy as heat [21-28]. This plasmonic heating itself has a variety of uses, such as thermal treatment of cancer cells[29] and controlling nanowire growth [30]. However, it may also be possible for the hot carriers to tunnel into the adjacent adsorbate or surface state, resulting in an excitation similar to that obtained in CID [24,31-37].

Either mechanism can affect a reaction in the adsorbed molecules [38-41]. Some examples include hot-hole mediated oxidation of citrate molecules on silver nanosurfaces [42-44], the plasmon-assisted splitting of water [45-47], and the partial oxidation of ethylene [48].

Hot carrier injection and CID are also not limited solely to affecting catalysis, and can also be used to trigger or power a variety of hot carrier devices [49,50].

One dramatic example of hot carrier catalysis the gold-catalyzed plasmon-mediated disassociation of hydrogen (H_2), as shown in Mukherjee et al [51,52], who demonstrated that it is possible induce H_2 (and D_2) disassociation via laser illumination of AuNSs on a TiO_2 substrate, and that the increase in H_2 disassociation was not due to thermoplasmonic heating or optical enhancement. This suggests that hot electrons leave the surface of the excited nanosphere and occupy an anti-bonding orbital of H_2 (or D_2). This in turn leads to the disassociation of the bond and the formation of H^-.

Our group has previously explored the properties of 1-(6-nitrobenzo[d][1,3]dioxol-5-yl)ethyl(4-(1,2-dithiolan-3-yl)butyl) carbamate (**1**), a photocleavable *o*-nitrobenzyl based ligand, shown in Scheme 3.1 [53]. When exposed to ultraviolent light, **1** undergoes photocleavage, resulting in the amine-terminated **1a** and its leaving group. Both **1** and **1a** can bond to gold and silver surfaces. It efficiently forms SAMs on gold, binding to the surface through the disulfide group. Quartz crystal microbalance measurements have shown that a 2 mM solution of **1** in ethanol would form a complete, stable SAM on a gold surface within 6 hours, with a surface density of ~$3*10^{-10}$ mol/cm^2 and a thickness on the order of 10-15 Å.

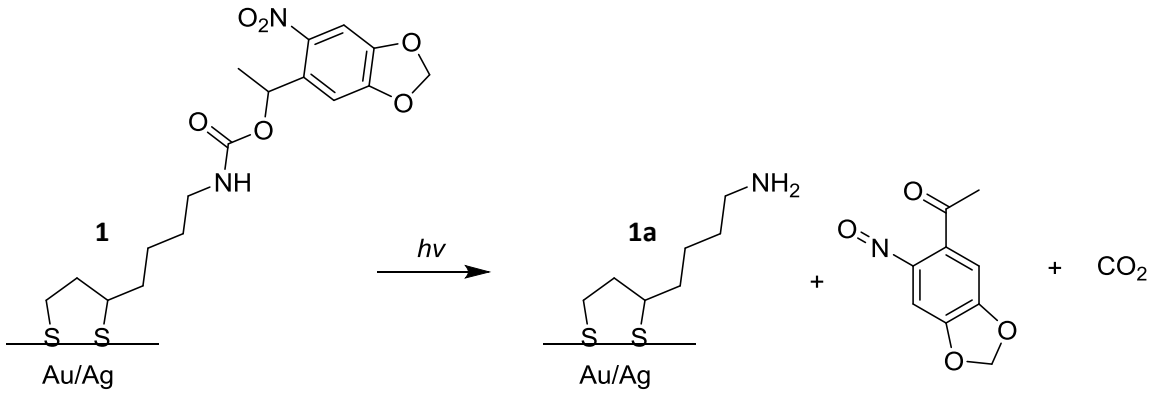

Scheme 3.1: Photocleavable ligand studied in this paper. When exposed to ultraviolet light, 1 undergoes photocleavage, resulting in the amine-terminated 1a, its leaving group, and CO_2. Both 1 and 1a can bond or stay bound) to gold and silver surfaces via the double-sulfide group.

Such a monolayer can be patterned by exposure to ultraviolet light with a wavelength of 365 nm, at a dose of ~1 J/cm^2. This exposure induces the photouncaging of the amine group in **1**

(Scheme **1**), resulting in **1a** as the primary byproduct, which produces an exposed primary amine group on the surface. At sufficiently low pH, this amine becomes positively charged. When the surface is then exposed to a low pH bath of negatively charged gold nanospheres (AuNSs), the AuNSs will bind to the surface. This binding can be detected via imaging the substrate in a Field Emission Scanning Electron Microscope (FESEM), where the AuNSs present as bright dots, visualizing the patterning obtained from UV exposure. Areas of high exposure see a much higher rate of AuNS deposition than unexposed areas, as shown in Figure 3.2, which demonstrates both the spatial resolution of the lithography (<0.5 μm) and its potential use in the directed self-assembly of nanoparticles.

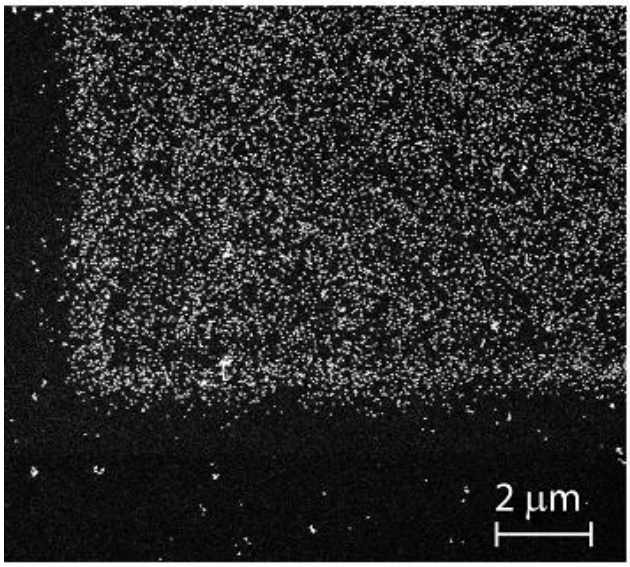

Figure 3.2: AuNS deposited on a photoactivated substrate of 1, and demonstrates the resolution of photoactivation. Light areas indicate AuNS adhesion, from Daengngam et al.[53]

When investigating **1** bound to silver nanoparticles, we observed an additional photoreaction outside of **1**'s (and **1a**'s) absorption band. As will be detailed below, exposure to light in the 550nm range led to a decrease in AuNSs binding to **1a**. This implies that a photoreaction either removed **1a** from the particle surface or neutralized its ability to become charged at low pH.

A plasmonically-driven hot-carrier catalysis that occurred under similar conditions was described by Wu et al [54], where they theoretically predicted that para-aminothiophenol

(PATP), a common probe chemical in SERS, could catalyze into dimercaptoazobenze (DMAB) under appropriate illumination conditions, such as a typical SERS measurement. This was experimentally proven both in Fang et al [55] for aqueous silver nanoparticle and in Huang et al [56] for thin, rough silver films in the presence of silver nanospheres. The structure, and proposed reaction, is shown in Scheme 3.2.

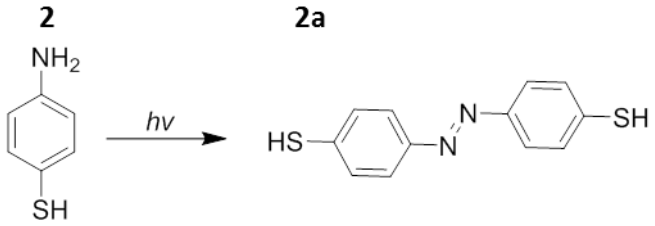

Scheme 3.2: PATP (2) can, under illumination, spontaneously catalyze into and trans DMAB (2a) as described in Huang et al. [56]

Detailed analysis by Zhao et al [57] showed this reaction was a form of photo-activated catalysis, similar to the plasmonic disassociation of H_2. In this case, however, the process involves hot holes generated via plasmon decay in the silver nanoparticles, which are then injected into the adsorbed PATP. This begins a chain of reactions that results in the amine losing its hydrogens and forming a N=N double-bond with its nearest neighbor, transforming the PATP to DMAB. Other recent work on this topic has explored the conditions under which this catalysis occurs on gold nanoparticles [58,59], and the efficacy of the catalysis when a graphene intermediary is placed between the PATP molecule and the nanosurface [60].

In this paper, we investigate this phenomenon and show that the secondary photoreaction undergone by **1a** is purely a photo-optical effect, much like the PATP-DMAB catalysis. We also show that this phenomenon is confined to nanostructured surfaces, and is very likely a plasmon-driven process similar to the PATP-DMAB hot-electron mediated catalysis.

3.3 Materials and Methods

3.3.1 Reagents and Materials

Silver (99.99%) and titanium were purchased from Kurt. J. Lesker company. Glass substrates used are Fisherbrand Microscope Slides and were purchased from Fisher Scientific. Silver nitrate ($AgNO_3$) 99%, tri-sodium citrate, and gold (III) chloride trihydrate ($HAuCl_4 \cdot 3H_2O$) (99.99%) were purchased from Sigma Aldritch, while potassium hydroxide (KOH) pellets (85%) were purchased from Arcos Organics. Ammonium hydroxide (NH_4OH) was purchased from Spectrum, and glucose was purchased from Fisher Scientific. 1-(6-Nitrobenzo[d][1,3]dioxol-5-yl)ethyl(4-(1,2-Dithiolan-3-yl)butyl)carbamate (**1**) was obtained via the method outlined by Daengngam et al [53].

3.3.2 1-(6-nitrobenzo[d][1,3]dioxol-5-yl)ethyl(4-(1,2-dithiolan-3-yl)butyl) carbamate Synthesis

The molecule was synthesized from two primary precursors, lipoic acid and 1-(6-nitrobenzo[d][1,3]dioxol-5-yl)ethan-1-ol. The synthesis itself is outlined in Daengngam et al [53].

3.3.3 Gold Nanosphere Synthesis

AuNS were prepared via the Turkevitch method as outlined in Frens et al.[61] In brief, 2 ml of 40 mM tri-sodium citrate in water were added to a boiling 100 ml aqueous solution of 300 µM gold (III) chloride trihydrate under vigorous stirring, resulting in citrate-capped AuNS of ~10 nm diameter. The pH of the solution was adjusted to ~5.4 with diluted hydrochloric acid.

3.3.4 Surface and Sample Preparation

Rough silver nanospheroid (AgNS) surfaces were prepared via the Tollens method as outlined in Wang et al [62]. The substrates used for spheroid formation were glass microscope slides, which were cleaned by soaking in aqua regia for twenty minutes, followed by thorough rinsing with deionized (DI) water, and drying with a stream of dry nitrogen gas prior to use.

3 mL of 0.1 M $AgNO_3$ was then prepared in DI water. A single drop of pure NH_4OH was added, resulting in a brown precipitant. Further NH_4OH was added dropwise until the resulting brown precipitant dissolved. The $AgNO_3$ was then mixed with 1.5 mL of 0.8 M KOH, resulting in a black precipitant. Pure NH_4OH was added again until the solution once more became clear. Then, 0.75 mL of the resulting solution was quickly mixed with 0.75 mL of a 0.5 M glucose solution, and dropcast onto the glass slides. The solution was allowed to sit for 75 seconds and then rinsed with DI water to halt the reaction. This resulted in a glass substrate covered in AgNSs, with diameters ranging from 20 to 100 nm and with strong absorption peaks ranging, based on particle size, from 350 to 450 nm.

The samples were double-rinsed thoroughly in DI water, blown dry with dry nitrogen gas, then placed in a 1 mM solution of **1** in ethanol under argon for ~36 hours. After that time, the samples were removed and dried with nitrogen, and allowed to sit for ~5 hours in darkness, unless otherwise stated.

Thick continuous film silver samples were prepared via e-beam evaporation of 5 nm titanium followed by 150 nm of silver on an aqua regia cleaned Fisherbrand glass substrate. After deposition, these samples were treated identically to Tollens-made samples.

For the purposes of testing the reaction of **1** and **1a** in solution, 40 µM solutions of **1** in ethanol were prepared for various degrees of photoexposure.

3.3.5 Photoexposure

In order to determine the conditions that resulted in the prevention of AuNS adhesion, samples were dosed with differing exposures of UV (365 nm) and green (550 nm) light. UV exposures were provided by a FB-UVXL-1000 UV Crosslinker lamp. Green light was provided by a Mercury-Xenon white light source and a 550 nm green light filter with a 10 nm bandwidth (Andover Corporation's 550FS-10) and a power of ~1 mW/cm^2. UV doses were 1 J/cm^2, as this dose was previously shown to transform most of the adhered **1** to **1a** on gold surfaces. Green doses were ~2 J/cm^2, as this was the dose strength at which the observed secondary reaction had been discovered. All exposures were performed in atmospheric conditions.

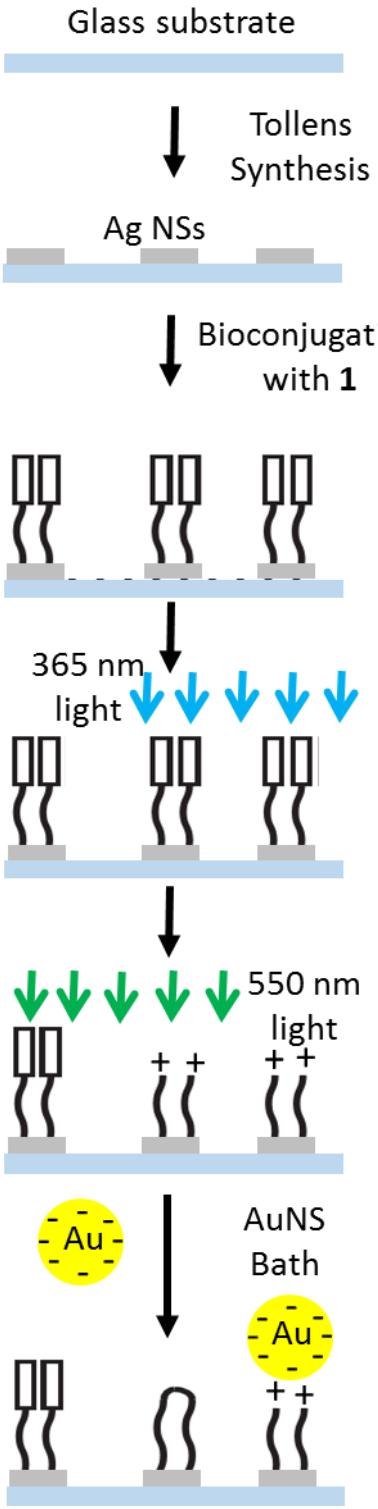

Figure 3.3: The AgNS substrate is conjugated with 1, subjected to photoexposure(s), and then exposed to a suspension of negatively charged AuNSs, which will adhere to any positively charged 1a on the surface.

Due to differences between samples causing different amounts of non-specific binding, AuNS adhesion is not always uniform from sample to sample, even among uniform exposure types. Similarly, the size distribution and plasmon resonance wavelength range also differ between samples. Therefore, we have designed the experiment such that two different exposure types can be compared on a single sample. Samples were exposed either across their entire surface (a flood exposure) or in alternating 3.8 mm wide bands defined by a simple brass metal mask placed on top of the sample (a banded exposure). When we combine flood with banded exposures, the sample is divided into two types of regions—those that received both the flood and the banded exposure (denoted Region 1) and those that received only the flood exposure (Region 2).

3.3.6 Gold Nanosphere Adsorption.

Immediately after the final exposure, AuNSs in an aqueous suspension were drop-cast onto the sample and left to incubate for thirty minutes. Afterwards, samples were rinsed thoroughly, then blown dry with compressed air.

A schematic illustrative of our sample preparation process is shown in Figure 3.3.

3.4 Results and Discussion

Table 1 provides an overview of the various samples, as well as the type of light exposure each of them received. The approximate AuNS density in each sample is indicated

qualitatively as either high, low, or none. In those regions that were exposed to multiple doses of light, the dose designation indicates the order of exposure, i.e. green-UV indicates green light exposure followed by ultraviolet light, while UV-green indicates the reverse order. In what follows, we discuss the characterization of all samples, performed by both UV-vis spectrophotometry (for transparent samples) and SEM imaging.

Table 3.1: List of samples, exposure types, and results.

		Exposure		AuNS Density	
Sample	Type	Region 1	Region 2	Region 1	Region 2
A	Tollens	UV	None	High	None
B	Tollens	Green	None	None	None
C	Tollens	Green-UV	UV	High	High
D	Tollens	UV-Green	UV	Low	High
E	Thick Film	UV	None	High	Low
F	Thick Film	Green	None	Low	High
G	Thick Film	UV-Green	UV	High	High
H	Tollens	Green-UV	UV-Green-UV	High	Low

3.4.1 Silver Nanospheroid (Tollens) Results.

Figure 3.4 shows the UV-vis extinction spectra for the four initial Tollens substrates (A-D). Each panel plots the spectra from both Region 1 and 2 on a specific sample, with the exposure indicated in the legend.

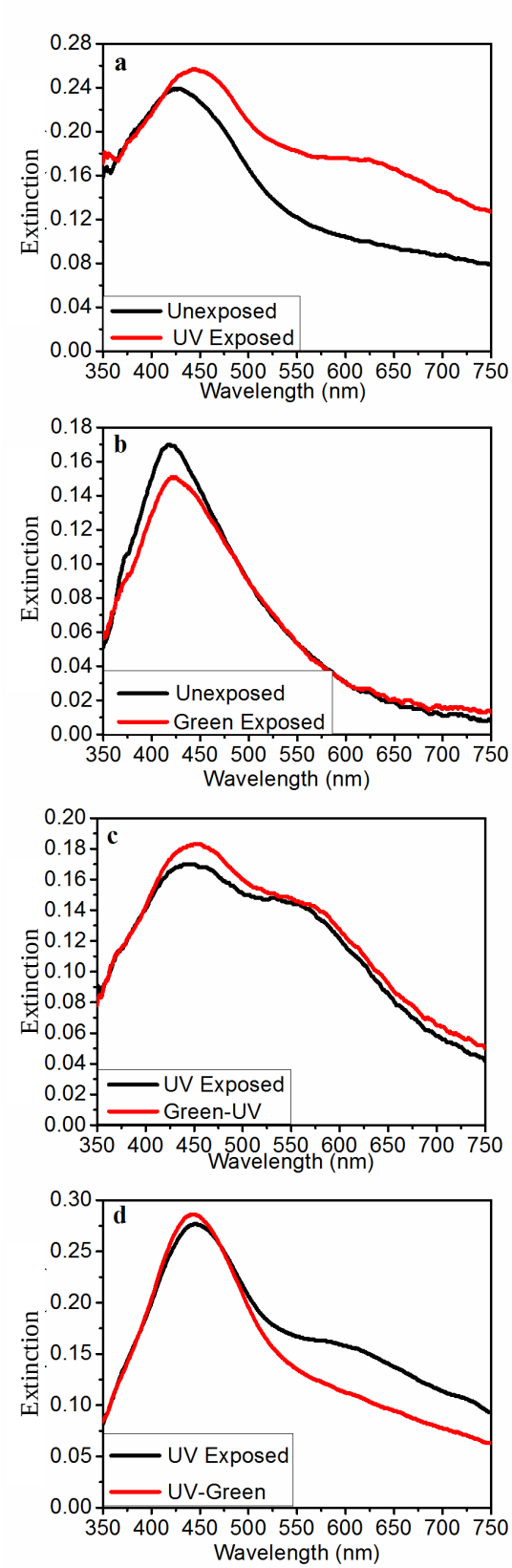

Figure 3.4: Optical extinction spectra of samples prepared as indicated in Table 1. a) Sample A . b) Sample B. c) Sample C. d) Sample D.

When AuNSs adhere to the AgNSs on the Tollens surface, they will produce a slight red shift in the silver particle plasmon peak as well as the appearance of an additional peak or shoulder on the red side of the initial peak. This occurs because between aggregation between Ag and Au particles has the effect of red-shifting the AgNSs plasmon resonance, and also causes the appearance of an additional plasmon mode, sometimes known as a gap plasmon[63-66] that is characterized by a high light intensity in the gap between the two nanospheres. It is the gap plasmon that is responsible for the peak in the 550-600 nm range, and the observation of a peak or shoulder in this range is a clear indication of AuNS binding to the AgNS at the substrate.

We also need to note that there is a fairly large sample-to-sample variation in the Tollens substrates, due to high sensitivity to initial conditions and reaction time. As a result, the initial plasmon peak position and shape can be rather different in different samples. At the same time, uniformity within a single sample is high (see supplemental information Figure S3). For this reason, we can legitimately compare the two spectra in each of the panels in Figure 3.4 to each other, as they were taken from different regions of the same sample.

The extinction spectra of Sample A (Figure 3.4a) shows the difference between areas that had been exposed to UV light (where AuNSs should stick to **1a**) and those which had no exposure (where nominally only **1** was present, and AuNSs should not stick). The spectrum from Sample A shows a red-shift of ~8nm in UV exposed areas when compared to unexposed areas. There is also a strong secondary peak at ~550-600 nm in the exposed areas when compared to the unexposed areas. This indicates that, as expected, AuNSs stick primarily to the areas exposed to UV light.

Sample B shows the difference between areas exposed to green light and unexposed areas. The plot of its extinction spectra (Figure 3.4b) shows no significant difference between green light exposed and unexposed regions, and indicated that there was no AuNS binding of note anywhere on the sample.

In Sample C, we compare a green-UV exposure to UV exposure only. Its extinction spectra (Figure 3.4c) also show little difference between the two regions, but in contrast to Sample B, both spectra exhibit a peak near 550nm, indicating AuNS binding across the entirety of the sample.

To establish if the order of exposure is important, Sample D compared UV-green exposure (i.e., the opposite exposure order compared to Sample C) to UV exposure only. As shown in Figure 3.4d, UV-only areas (indicated by the black trace) show a red shift in the main peak (~8nm) and the emergence of a secondary peak at ~600 nm, indicating that AuNSs bound to these areas, as expected from Sample A. On the other hand, in areas that were exposed to UV followed by green light (red trace) there is no red shift of the main peak and no shoulder on its red side. This indicates that the AuNSs did not bind to the UV exposed areas that had been subsequently dosed with green light. This is a reversal of the pattern seen in Sample A, which suggests that exposure to green light has prompted an alteration to **1a**, preventing the AuNSs from adhering to the substrate.

This is further reinforced by FESEM imaging of the sample. Figure 3.5 shows SEM images of the surface of samples A and D. The AgNSs appear as darker grey spheres, and the smaller, brighter spheres highlighted in red are AuNSs—in the original SEM images, the AuNSs were distinguished from the AgNSs by their monodisperse size (~20 nm) and higher brightness

when contrasted with AgNSs of the same size. This is discussed in greater detail in the supplemental information Figure 3.5a shows that the AuNSs do not bind to an unexposed surface on Sample A. In contrast, UV exposed areas (Figure 3.5b, from Sample D) show extensive AuNS binding to the AgNS. This is expected and agrees with the spectrum as shown in Figure 3.4a. Similarly, in Figure 3.5c (Sample D), we see that there is no AuNS adhesion in the areas that received UV-Green exposure, which is in agreement with the spectra in Figure 3.4d.

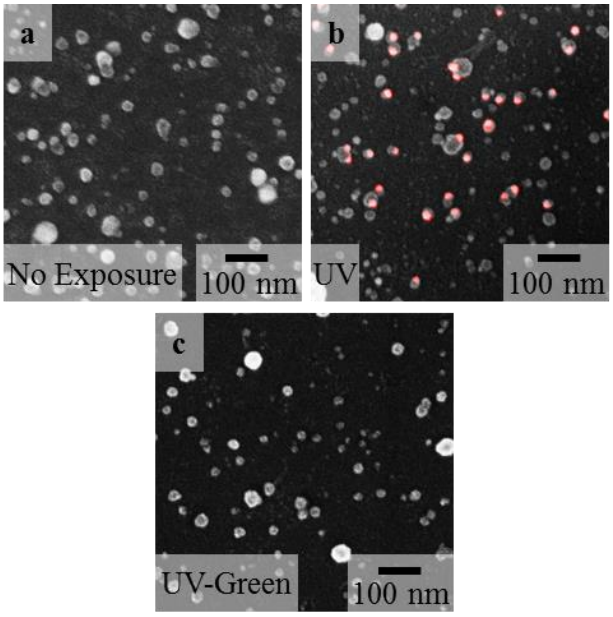

Figure 3.5: Tollens samples under FESEM imaging, with gold nanospheres highlighted in red, in order to show lack of adhesion after UV-Green exposure. a) Unexposed (Sample A) b) UV exposed (Sample D) c) UV-Green exposed (Sample D)

Together, this data shows that exposure to green light after the UV cleaving induces a photoreaction that removes the ability of **1a** to bind AuNSs to the surface. In contrast, we also see that **1** is not affected by the green light exposure performed before cleaving with UV light.

Comparison of these samples allows us to conclude that the binding properties of **1a** are only neutralized if the 550 nm dose occurs after the 365 nm dose. If that were not the case, and the order of the exposure did not matter, Sample C (Figure 3.4c) should show an absorption spectra of the same type as Sample D (Figure 3.4d), as these samples differ only in the order of exposure to green and UV light.

Furthermore, the data from Sample C shows that the green light exposure does not remove **1** or **1a** from the silver surface. If it did, then the absorption spectrum of the green-only exposed areas of Sample B (Figure 3.4b), the green-UV areas of Sample C (Figure 3.4c), and the UV-green areas of Sample D (Figure 3.4d) should indicate no AuNS binding, as all three would have **1** (or **1a**) stripped from the substrate, and subsequent UV exposure should have had little or no effect. Instead, we see a stark difference between the spectra of these samples, demonstrating that even after exposure to 550 nm light, **1** remains on the surface. It is clear that some chemical reaction is taking place on the surface of our substrate. In total, these four samples demonstrate that the interaction which occurs is related to **1a**'s amine groups, and can only proceed once **1** has been transformed into **1a** via UV exposure.

3.4.2 Continuous Silver Film Results

Silver films (samples E-G) were used to determine if the green-light-induced photoreactive effect is plasmonic in nature or not. If the effect is not plasmonic, then it should occur on continuous thick (150nm) silver films as readily as it occurred on Tollens substrates. If it is plasmonic in nature, a thick film should show little or no signs of the photoreactive effect, as surface plasmons are more difficult to directly excite on thick metal films with light incident from the air side of the sample. While the roughness of even a thick film does allow for some excitation of traveling surface plasmon-polariton waves, this is a weak effect, and the much stronger localized surface plasmon resonance seen in the isolated AgNS structures are entirely absent.

As the thick films interact differently with light compared to the Tollens surfaces, the intensity of visible light near the surface will also be changed, resulting in much lower light intensity at the surface of the continuous silver films than on the silver nanospheroids of a Tollens surface. To compensate for this reduction, the green light exposure time for Sample G was increased by a factor of 50 (from 30 minutes to approximately 24 hours) when compared to the Tollens sample exposures. A calculation justifying this increase is detailed in the Supporting Information. The continuous film samples were characterized via SEM imaging, and images were further analyzed with a sphere-counting program written in Mathematica to quantitatively compare the density of sphere adhesion on different areas of the substrate. Figure 3.6 displays

this as a graph of sphere density as a function of sample exposure for our continuous silver film samples.

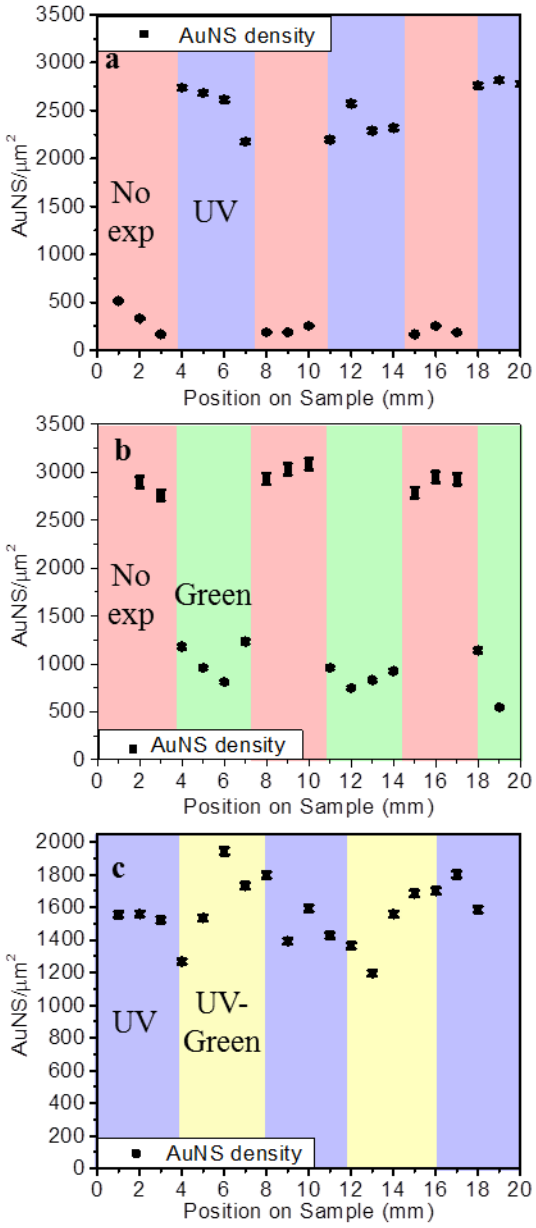

Figure 3.6: Histograms of particle density as a function of sample exposure. Red backgrounds indicate no exposure, blue backgrounds indicate UV exposure, green backgrounds indicate a green light-exposure, and yellow backgrounds indicate a UV-green exposure. Samples included are a) sample E, b) Sample F, and c) Sample G. Error bars assume spheres are Poisson distributed.

Figure 3.6a shows a qualitative graph of Sample E's particle density as a function of sample exposure, comparing the difference in AuNS adhesion between UV exposed and unexposed areas. In exposed areas, we can see a higher sphere density than in the unexposed areas by approximately a factor of five. This indicates that the UV exposure has indeed cleaved **1** into **1a**. However, while the AuNS density in the unexposed areas is lower than in the exposed areas, some AuNS binding is still present, as shown in the SEM image in Figure 3.7a. This is due to some amount of non-specific binding. The source of the non-specific binding could be due to some fraction of **1** breaking or otherwise decaying into **1a** without UV-light exposure, or it could be caused by some other contaminant. However, as we have seen non-specific binding across a broad spectrum of samples, the latter is less likely. Regardless, we nevertheless can see a clear contrast between UV exposed and UV unexposed areas.

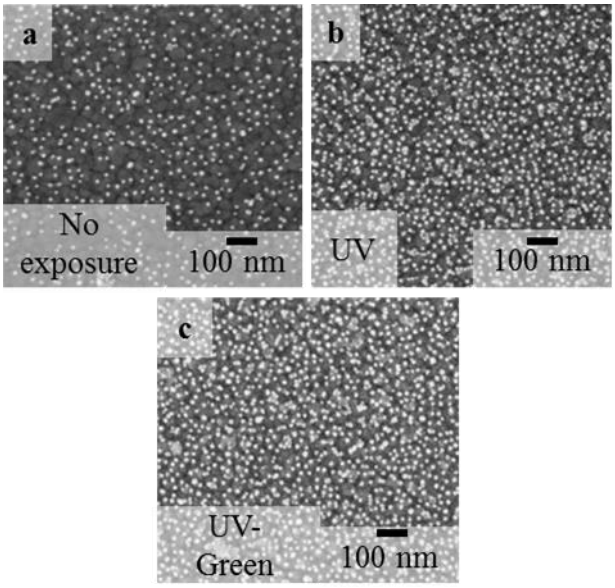

Figure 3.7: AuNS adhesion on a thick silver film for a) Unexposed area (Sample E), b) a UV exposed area (Sample G), and c) a UV-Green exposed area (Sample G). Note that there is little difference between the UV and UV-Green exposed areas.

With Sample F, we look at the difference in AuNS adhesion between unexposed and green light exposed areas on a thick Ag film. A plot of the AuNS density as a function of exposure area can be seen in Figure 3.6b, and SEM images of unexposed and green exposed areas can be seen in Figures 3.8a and 3.8b. We can see a stark difference between the unexposed and green exposed areas, with less AuNS adhering to the areas that were exposed to green light. This would imply that the nonspecific binding seen in several samples (such as the unexposed areas of Sample E in Figure 3.6a) are indeed caused by premature cleavage of **1** into **1a**, and which can be prevented via green light exposure. This is supported by previous results [67], which shows that photocleaving a small percentage of **1** into **1a** is sufficient for some adhesion of AuNSs to the surface to occur. As nonspecific binding can differ significantly from sample to sample, the differences between the unexposed areas of Sample E and the unexposed areas of Sample F are not unexpected. Precisely because of this issue, we focus on the differences in binding across a single sample.

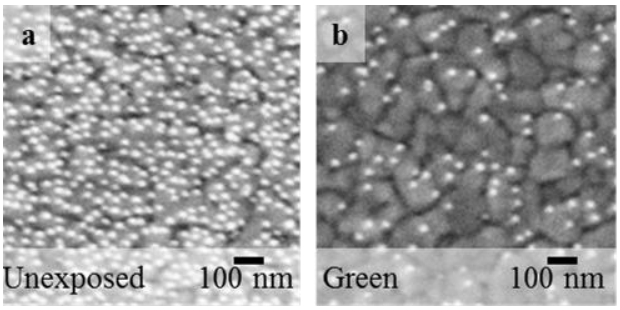

Figure 3.8: AuNS adhesion on a thick silver film for a) Unexposed area (Sample F), and b) Green light exposed areas (Sample F). Note the reduction in nonspecific binding for green-exposed areas.

Sample G examined the difference in AuNS adhesion between UV-green exposed areas to UV-exposed areas on a thick, continuous film. Figure 3.6c shows a graph of the sample's sphere density as a function of sample exposure, and Figures 3.7b and 3.7c show SEM images of UV exposed and UV-green exposed areas. In contrast to Sample E and Sample F, there is no easily identifiable relationship between sample exposure and sphere density. This indicates that, on a continuous silver film, UV exposure followed by subsequent exposure to green light does not result in a significant drop in AuNS adhesion. We can conclude that the **1a** present on the surface either did not undergo the photoreaction seen in the nanospheroid substrates, or did not undergo the photoreaction to the same extent.

This suggests that the green-light induced photoreaction we see in Sample D does not occur (or does not occur as strongly) on thick silver films. From this we conclude that it is likely that the green-light induced photoreactive effect is plasmonically driven, as thick silver films are less plasmonically available than rough thin films or nanospheroid surfaces. At the same time, green light exposure does reduce the non-specific binding on thick silver films, as seen in Sample F, implying that the green-light induced photoreactive effect *can* occur on thick silver films. Thick silver films are capable of supporting surface plasmons, but both the excitation strength and the plasmon intensity are greatly reduced compared to isolated structures. This is consistent with our results, which show that green light induced photoreaction *can* proceed on thick silver films, but with a greatly reduced efficiency.

3.4.3 Photoreactivity in Solution

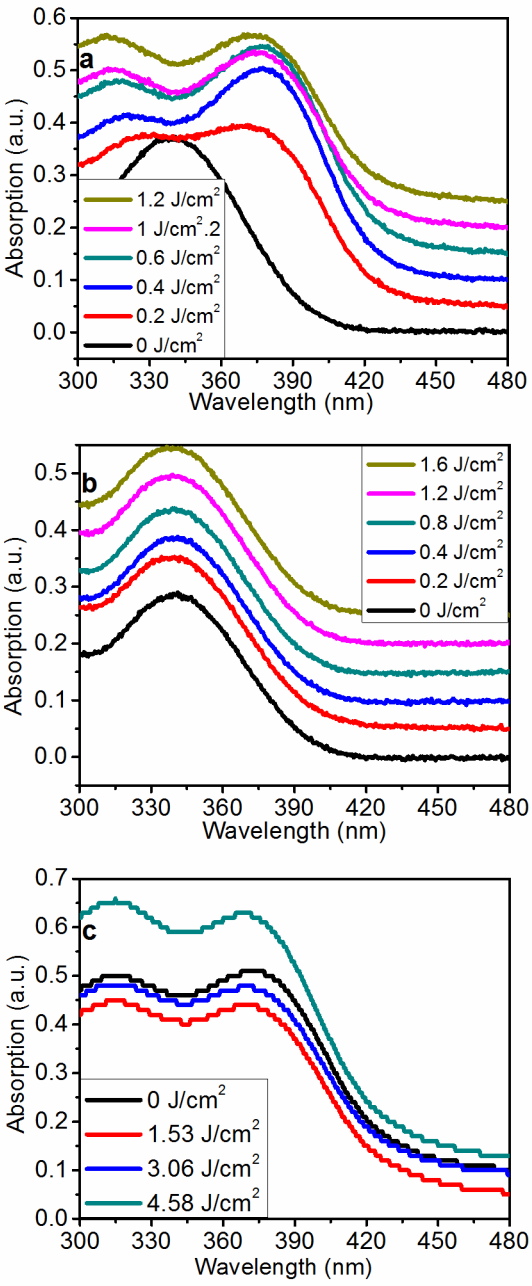

Figure 3.9: a) Absorption spectra of 1 with increasing UV doses b) Absorption spectra of 1 with increasing 550 nm doses c) Absorption spectra of UV-dosed 1 (1a) with increasing 550 nm doses. Individual spectrum in the figures are offset for clarity.

As a final control experiment, we investigated if green light could induce a photoreaction in solution. To that end, we compared the absorption spectra of three 40 μM solutions of **1** in ethanol. One sample was exposed to increasing doses of UV light, another was exposed to increasing doses of green light, while a third was exposed to 1 J/cm^2 of UV light, followed by increasing doses of green light. The spectra of all three samples can be found in in Figure 3.9, with individual spectra offset for clarity.

As previously shown in Daengngam et al [53], the absorption spectrum of **1** consists of one single 340 nm. With an increasing UV dose, the 340 nm peak flattens, then splits into a 300 nm and a 385 nm peak. This indicates the cleavage of **1** into its two constituent parts, **1a** and its leaving group. This is shown in Figure 3.9a.

When repeated with green light (550 nm range), the sample showed no change in its absorption spectrum, even when exposed to green light dosages in excess of the energy needed to photocleave with UV light, as shown in Figure 3.9b. In Figure 3.9c, the sample was exposed to UV light at 1 J/cm^2 prior to exposure to green light. As in Figure 3.9b, successive green light exposures engender no major change in the absorption spectrum of the solution. This suggests that, in solution, exposure to green light (prior or post cleaving) has no effect on the structure of **1** or **1a**.

Liquid chromatography mass spectrometry (LCMS) was performed on all three samples in their fully exposed state as well as on an unexposed sample of **1**. This measurement confirmed that there is no appreciable difference between the unexposed sample and the sample exposed to green light, or between the UV-exposed and the UV-green exposed samples. With this result, we can now draw the conclusion that the green-light induced reaction occurs only on surfaces such as rough silver films and silver nanoparticles, and that it is a plasmonically driven effect.

3.4.4 Pattern Reversal

Our previous work showed that we can use UV light to selectively photopattern **1** on a gold substrate, allowing AuNSs or other compatible materials to bind to the exposed areas [53]. In this paper, we have demonstrated that we can replicate this effect on nanostructured silver surfaces, allowing AuNSs to bind only to areas that have been exposed to UV light. Additionally, we have demonstrated that we can, with additional exposure to green light, neutralize the AuNS binding ability of the UV-exposed areas.

This green-light photoreaction gives us an additional method of photopatterning our samples, as we can now reverse the effect of the UV light on the surface, which makes it possible to reverse the pattern created by the photomask. To do this, the sample is first exposed to UV light, creating patterned areas where **1** is cleaved into **1a**. Next, the AuNS binding ability of the exposed area is removed via flood exposing the sample to green light. This is followed by a flood exposure to UV light, which creates a pattern of primary amine-presenting **1a** that is the reverse of the pattern created by the initial dose of UV light. (It should be noted that to reduce the degree of non-specific binding, both samples were also flood-exposed to green light *prior* to the initial UV dose.)

A sample prepared in this manner is listed as sample H in Table 1. It is visually compared to Sample A in Figure 3.10.The two samples are both initially exposed to UV light in the same pattern, which consists of a horizontal band through the center of both samples as they appear in the figure. Areas where AuNSs have adsorbed at high density appear darker in the image. We can clearly see the reversal of the pattern using green-UV flood exposure in Sample H. This allows for more complex photopatterning on plasmonically active substrates.

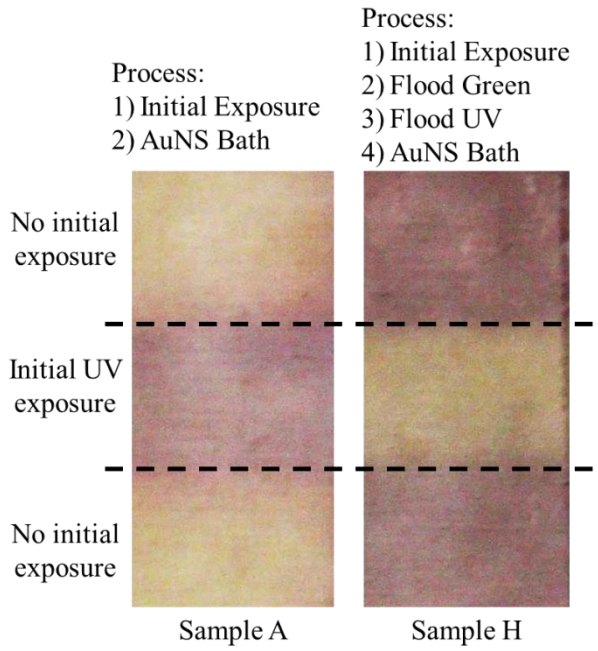

Figure 3.10: Portions of samples demonstrating photoreversal capabilities of 1. Left: Standard patterning, with AuNs adhering only to the UV-exposed (center) area of the sample. Right: Reversed exposure, with AuNS sticking everywhere except the initially UV-exposed center (contrast enhanced).

3.5 Discussion

By this point, it is clear that even though neither the ligand **1** nor **1a** absorb light at 550 nm, we can nonetheless induce a reaction in a SAM containing **1a** that leads to the neutralization of the **1a**'s ability to bind to AuNSs, and this appears to be a plasmonically driven reaction. Furthermore, as we have just demonstrated, we can use this effect to perform a form of plasmon-mediated reverse photolithography.

We note here that even though 550 nm does not coincide with the peak of the plasmon in the AgNS sample, thepeaks are quite wide and extend past 550 nm. This means that the AgNS plasmon resonances are readily excited by the green light.

What is not yet clear is the precise mechanism of the green-light-induced photoreaction, and we will put off this identification for future work. It is nonetheless instructive to note that there are examples in the literature of plasmon-mediated reactions that are very similar to what

we are observing. As we mentioned in the introduction, it has been shown that PATP (**2**) will, when adsorbed onto silver nanoparticles, catalyze into DMAB (**2a**) under nonresonant illumination, forming a N=N double bond. Furthermore, this catalysis can be attributed to hot hole injection caused by plasmon decay in the silver nanoparticle surface.[55] Upon initial examination, **1** is rather dissimilar from PATP, but it cleaves into **1a**. Unlike **1**, **1a** contains a primary amine, as does PATP. In Figures 3.4c and 3.4d, we also see that the green-light-induced photoreaction only proceeds when **1a** is present prior to the green light exposure, and that **1** is unaffected by green-light exposure. This suggests that it is the amine group of the ligand which undergoes the photoreaction, and that the amine group must be present on the surface for the photoreaction with green light to occur.

We therefore propose that, when adhered to a AgNS and exposed to green light, **1a** undergoes a photoreaction similar to that of PATP (**2**) catalyzing into DMAB (**2a**), and forms N=N bonds with its nearest neighboring ligand. The formation of an N=N double bond would prevent **1a** from becoming positively charged at low pH, and therefore remove its ability to bind the negatively charged AuNSs. Furthermore, the photon energy used in this photocatalysis (550 nm) is within the range used by Fang et al [55] in their PATP(**2**) catalysis. This premise is further supported by the fact the photoreaction requires available plasmon modes to operate.

However, other possibilities also exist. When in a SAM, **1**'s photocleavage does not always result in **1a.** There is a possible side reaction in which **1**'s nitro group reduces into an aromatic amine, and no photouncaging occurs [68,69]. It is possible that the amine groups generated by photouncaging **1** into **1a** are reacting with the products of this side reaction, and that this also results in a nullification of **1a**'s ability to bind AuNS. This process might proceed identically to the previously hypothesized reaction, with two nearby amine groups forming a N=N bond via hot carrier catalysis. However, as the rest of the photocleavable leaving group is not removed, other chemistries may also be possible. Whatever the details of the green light induced reaction are, our results show that it is very likely plasmonically driven.

Our data also gives some indication of **1a'**s orientation relative to the surface of the silver nanoparticle. The hot carriers must reach the amine group via a means other than electric conduction through the molecule, as the alkyl group with a primary amine cannot act as a

conductor of charge. This means that for hot carriers to either tunnel into or be excited within the **1a**-containing SAM, the ligands need to be lying down on the surface at least part of the time, so that the amine groups overlap with the electronic wavefunction of the metal, which extends about 10Å from the surface. This is consistent with observations we have made on this SAM in a different context [70], which indicate that SAMs made from **1** are of medium density, allowing the endgroup of **1** to spend at least part of the time in close proximity to the surface.

3.6 Conclusion

We have demonstrated an additional photoreaction in a photocleavable *o*-nitrobenzyl-based disulfide ligand when adhered to silver nanoparticles. The reaction first requires the silver nanoparticle be exposed to UV light, transforming the adsorbed **1** into **1a** via photouncaging. Then, if the particle is exposed to green light, this results in a photoreaction that prevents **1a** from becoming positively charged at lower pH. This, in turn, prevents negatively charged AuNSs from adhering to the AgNSs, demonstrating the light-induced alteration to **1a**. This reaction allows us to neutralize **1**'s binding properties post-cleaving. We hypothesize this is due to a hot-hole catalyzed reaction, similar to the hot-hole catalyzed transformation of PATP into DMAB, as seen in Fang et al [55].

This post-UV passivation creates a broader category of uses for **1** within the context of photo lithography and nanoparticle adhesion. In addition to the direct photo-patterning demonstrated in Daengngam et al[53], this photoreactive effect would allow for reverse-patterning of a sample, as demonstrated with a proof-of-concept shown in Figure 3.10. This reverse patterning may also be possible on plasmonically available Au substrates, as Xu et al [59] detailed that the similar PATP-DMAB conversion is possible with gold nanosphere substrates. It also allows for passivation of a surface post-deposition: after nanoparticles have adhered to a rough silver surface, the entire substrate could be dosed with a UV-green exposure, preventing any further particle binding.

Future research will both explore these possibilities, as well as more directly investigate the nature of the photoreaction occurring on the surface.

Chapter 3 References

[1] V. San Miguel, C. G. Bochet, and A. del Campo, Journal of the American Chemical Society **133**, 5380 (2011).
[2] M. C. Pirrung, L. Fallon, and G. McGall, The Journal of Organic Chemistry **63**, 241 (1998).
[3] P. Stegmaier, J. M. Alonso, and A. d. Campo, Langmuir **24**, 11872 (2008).
[4] D. A. Hutt, E. Cooper, and G. J. Leggett, The Journal of Physical Chemistry B **102**, 174 (1998).
[5] C. Dulcey, J. Georger, V. Krauthamer, D. Stenger, T. Fare, and J. Calvert, Science **252**, 551 (1991).
[6] N. J. Brewer, R. E. Rawsterne, S. Kothari, and G. J. Leggett, Journal of the American Chemical Society **123**, 4089 (2001).
[7] T. Höfler *et al.*, Materials Chemistry and Physics **119**, 287 (2010).
[8] B. Manning, S. J. Leigh, R. Ramos, J. A. Preece, and R. Eritja, Journal of Experimental Nanoscience **5**, 26 (2010).
[9] S. Kaneko, H. Nakayama, Y. Yoshino, D. Fushimi, K. Yamaguchi, Y. Horiike, and J. Nakanishi, Physical Chemistry Chemical Physics **13**, 4051 (2011).
[10] M. Nakagawa and K. Ichimura, Colloids and Surfaces A: Physicochemical and Engineering Aspects **204**, 1 (2002).
[11] S. Fodor, J. Read, M. Pirrung, L. Stryer, A. Lu, and D. Solas, Science **251**, 767 (1991).
[12] S. Petersen, J. M. Alonso, A. Specht, P. Duodu, M. Goeldner, and A. del Campo, Angewandte Chemie International Edition **47**, 3192 (2008).
[13] P. Stegmaier and A. del Campo, ChemPhysChem **10**, 357 (2009).
[14] K. A. Willets and R. P. V. Duyne, Annual Review of Physical Chemistry **58**, 267 (2007).
[15] K. Sun Mi, L. Si Woo, M. Song Yi, and P. Jeong Young, Journal of Physics: Condensed Matter **28**, 254002 (2016).
[16] M. J. Kale, T. Avanesian, and P. Christopher, ACS Catalysis **4**, 116 (2014).
[17] M. J. Kale and P. Christopher, Science **349**, 587 (2015).
[18] K. Wu, J. Chen, J. R. McBride, and T. Lian, Science **349**, 632 (2015).
[19] H. Petek, M. J. Weida, H. Nagano, and S. Ogawa, Science **288**, 1402 (2000).
[20] M. J. Kale, T. Avanesian, H. Xin, J. Yan, and P. Christopher, Nano Letters **14**, 5405 (2014).
[21] M. L. Brongersma, N. J. Halas, and P. Nordlander, Nat Nano **10**, 25 (2015).
[22] H. Inouye, K. Tanaka, I. Tanahashi, and K. Hirao, Physical Review B **57**, 11334 (1998).
[23] C. Voisin, N. Del Fatti, D. Christofilos, and F. Vallée, The Journal of Physical Chemistry B **105**, 2264 (2001).
[24] K. Watanabe, D. Menzel, N. Nilius, and H.-J. Freund, Chemical Reviews **106**, 4301 (2006).
[25] J. I. Gersten and A. Nitzan, Surface Science **158**, 165 (1985).
[26] L. Xiaoguang, X. Di, and Z. Zhenyu, New Journal of Physics **15**, 023011 (2013).
[27] M. Lisowski, P. A. Loukakos, U. Bovensiepen, J. Stähler, C. Gahl, and M. Wolf, Applied Physics A **78**, 165 (2003).
[28] H. Zhang and A. O. Govorov, The Journal of Physical Chemistry C **118**, 7606 (2014).
[29] J. M. Stern, J. Stanfield, W. Kabbani, J.-T. Hsieh, and J. A. Cadeddu, The Journal of Urology **179**, 748 (2008).
[30] L. Cao, D. N. Barsic, A. R. Guichard, and M. L. Brongersma, Nano Letters **7**, 3523 (2007).
[31] A. Manjavacas, J. G. Liu, V. Kulkarni, and P. Nordlander, ACS Nano **8**, 7630 (2014).
[32] J. Hofmann and W. Steinmann, physica status solidi (b) **30**, K53 (1968).
[33] J. E. Sipe and J. Becher, J. Opt. Soc. Am. **71**, 1286 (1981).
[34] C. Clavero, Nat Photon **8**, 95 (2014).

[35] P. Dombi, A. Hörl, P. Rácz, I. Márton, A. Trügler, J. R. Krenn, and U. Hohenester, Nano Letters **13**, 674 (2013).
[36] A. O. Govorov, H. Zhang, and Y. K. Gun'ko, The Journal of Physical Chemistry C **117**, 16616 (2013).
[37] R. Sundararaman, P. Narang, A. S. Jermyn, W. A. Goddard Iii, and H. A. Atwater, Nat Commun **5** (2014).
[38] L. Brus, Accounts of Chemical Research **41**, 1742 (2008).
[39] J. Gavnholt, A. Rubio, T. Olsen, K. S. Thygesen, and J. Schiøtz, Physical Review B **79**, 195405 (2009).
[40] A. Nitzan and L. E. Brus, The Journal of Chemical Physics **75**, 2205 (1981).
[41] P. V. Kamat, The Journal of Physical Chemistry B **106**, 7729 (2002).
[42] R. Jin, Y. Charles Cao, E. Hao, G. S. Metraux, G. C. Schatz, and C. A. Mirkin, Nature **425**, 487 (2003).
[43] X. Wu, E. S. Thrall, H. Liu, M. Steigerwald, and L. Brus, The Journal of Physical Chemistry C **114**, 12896 (2010).
[44] E. S. Thrall, A. Preska Steinberg, X. Wu, and L. E. Brus, The Journal of Physical Chemistry C **117**, 26238 (2013).
[45] E. Thimsen, F. Le Formal, M. Grätzel, and S. C. Warren, Nano Letters **11**, 35 (2011).
[46] S. J. Kim, I. Thomann, J. Park, J.-H. Kang, A. P. Vasudev, and M. L. Brongersma, Nano Letters **14**, 1446 (2014).
[47] I. Thomann, B. A. Pinaud, Z. Chen, B. M. Clemens, T. F. Jaramillo, and M. L. Brongersma, Nano Letters **11**, 3440 (2011).
[48] P. Christopher, H. Xin, and S. Linic, Nat Chem **3**, 467 (2011).
[49] H. Chalabi, D. Schoen, and M. L. Brongersma, Nano Letters **14**, 1374 (2014).
[50] F. Wang and N. A. Melosh, Nature Communications **4**, 1711 (2013).
[51] S. Mukherjee *et al.*, Nano Letters **13**, 240 (2013).
[52] S. Mukherjee, L. Zhou, A. M. Goodman, N. Large, C. Ayala-Orozco, Y. Zhang, P. Nordlander, and N. J. Halas, Journal of the American Chemical Society **136**, 64 (2014).
[53] C. Daengngam, S. B. Thorpe, X. Guo, S. V. Stoianov, W. L. Santos, J. R. Morris, and H. D. Robinson, The Journal of Physical Chemistry C **117**, 14165 (2013).
[54] D.-Y. Wu, X.-M. Liu, Y.-F. Huang, B. Ren, X. Xu, and Z.-Q. Tian, The Journal of Physical Chemistry C **113**, 18212 (2009).
[55] Y. Fang, Y. Li, H. Xu, and M. Sun, Langmuir **26**, 7737 (2010).
[56] Y. Huang, Y. Fang, Z. Yang, and M. Sun, The Journal of Physical Chemistry C **114**, 18263 (2010).
[57] L.-B. Zhao, Y.-F. Huang, X.-M. Liu, J. R. Anema, D.-Y. Wu, B. Ren, and Z.-Q. Tian, Physical Chemistry Chemical Physics **14**, 12919 (2012).
[58] X. Liu, L. Tang, R. Niessner, Y. Ying, and C. Haisch, Analytical Chemistry **87**, 499 (2015).
[59] J.-F. Xu, S.-Y. Luo, and G.-K. Liu, Spectrochimica Acta Part A: Molecular and Biomolecular Spectroscopy **143**, 35 (2015).
[60] Z.-g. Dai *et al.*, Light Sci Appl **4**, e342 (2015).
[61] G. Frens, Nat Phys Sci **241**, 20 (1972).
[62] Z. Wang, S. Pan, T. D. Krauss, H. Du, and L. J. Rothberg, Proceedings of the National Academy of Sciences **100**, 8638 (2003).
[63] K. Su, Q. Wei, X. Zhang, J. Mock, D. R. Smith, and S. Schultz, Nano letters **3**, 1087 (2003).
[64] C. Sönnichsen, B. M. Reinhard, J. Liphardt, and A. P. Alivisatos, Nature biotechnology **23**, 741 (2005).
[65] L. He, E. A. Smith, M. J. Natan, and C. D. Keating, The Journal of Physical Chemistry B **108**, 10973 (2004).

[66] C. Ciracì, R. T. Hill, J. J. Mock, Y. Urzhumov, A. I. Fernández-Domínguez, S. A. Maier, J. B. Pendry, A. Chilkoti, and D. R. Smith, Science **337**, 1072 (2012).
[67] C. Daengngam, Dissertation, Virginia Polytechnic Institute and State University, 2012.
[68] K. Critchley, L. Zhang, H. Fukushima, M. Ishida, T. Shimoda, R. J. Bushby, and S. D. Evans, The Journal of Physical Chemistry B **110**, 17167 (2006).
[69] K. Critchley, J. P. Jeyadevan, H. Fukushima, M. Ishida, T. Shimoda, R. J. Bushby, and S. D. Evans, Langmuir **21**, 4554 (2005).
[70] B. A. Magill, X. Guo, C. L. Peck, R. L. Reyes, E. M. See, R. M. Davis, W. L. Santos, and H. D. Robinson, TBA **TBA**, TBA (TBA).

CHAPTER 4

4 Plasmon-Directed Patchy Particle Creation and Self-Assembly from Isotropic Silver Nanoparticles

This chapter represents a paper that will be, but has not yet been, submitted to Phys Chem C.

Changes have been made to allow for formatting differences

4.1 Abstract

We demonstrate the creation of anisotropic patchy silver-nanospheroids (AgNSs) using linearly polarized UV light and a photouncaging *o*-nitrobenzyl-based ligand, which anchors to the AgNSs via a double-sulfur group. This compound anchors to both gold and silver surfaces, and exposure to 1 J/cm^2 dose of UV light induces a photouncaging reaction which reveals a primary amine on the surface. By using linearly polarized UV light, we meter the exposure dose such that only the poles of the nanoparticle receive a full dose, limiting the photouncaging reaction primarily to the particle's plasmonic hot spots. We reveal this anisotropy by selectively adhering negatively charged gold nanospheres (AuNSs) to the AgNSs via electrostatic attraction between them and the positively charged primary amines generated by photouncaging. When performed on a surface, this results in aligned nanoscale structures, which are characterized by rotational polarimetric spectroscopy.

4.2 Introduction

The self-assembly of nanoparticles into larger-scale structures is a natural step in the advance of nanotechnology. One paradigm of controlled self-assembly hinges on the ability to create nanoparticles with differentiated regions or patches. Such particles have one or more patches whose surface properties differ from the rest of the nanoparticle [1]. These can include areas of chemical alteration, such as a localized binding groups or a small patch of charged amines.

Alternatively, the patches can be physical anisotropies, such as roughened areas or asymmetrical shapes. Some patches straddle between these two, such as a nanoparticle with a patch of structural material distinct from the bulk of the nanoparticle. Ultimately, what is most important is that these patches allow for anisotropic interaction with other particles or surfaces. Once created, these anisotropies can be used and manipulated to cause the patchy particles to self-assemble into larger scale structures, relying either solely on the properties of the particle patches, such as hydrophobicity, polarity, and solvency, or using external fields such as magnetic or electric fields [2-6].

The methods for creating patchy particles are vast and varied, and so too are the ways in which to classify them [2,4,7,8]. One very simple approach is to break them down into two broad categories. Liquid phase deposition (LPD), in which the patches are assembled or applied via some wet chemical process, and vapor phase deposition (VPD), which involves the evaporation or otherwise vapor based deposition or removal of chemical or structural patches on the nanoparticle [2,7]. Techniques that fall under the broad umbrella of VPD include glancing angle deposition, chemical vapor deposition, and metal evaporation onto a monolayer of particles. LPD techniques include, but are in no way limited to, colloidal assembly, capillary flow techniques, and DNA modification.

Templating is the oldest technique for creating patchy particles and involves the manufacture of patches via the manipulation of interface boundaries. In broad terms, this technique relies on chemically or physically partially trapping a nanoparticle within a surface or along a boundary (the template). Once trapped, the nanoparticles can be subjected to a variety of modifications along one of the interfaces, depending on the type of interface boundary. These include metal deposition, the application of additional adhesive nanoparticles, or exposure to functionalizing ligands. Once the template is removed and the nanoparticles released, the result is a nanoparticle with one or more modified areas. Templating can be performed on wide variety of interfaces, including solid-air, liquid-liquid, liquid-air, and liquid-solid boundaries, and can also make use of several methods for applying the patches at these boundaries, including chemical conjugation and electron-beam evaporation [2,4,7,9-12]. Because of this, templating can be thought of as straddling the boundary between LPD and VPD, as it falls under both umbrellas.

Another possible method of patchy particle creation is the selective activation of photocleavable chemicals functionalized on a nanoparticle surface, which is the topic of this paper. Significant work has already been done on self-assembled monolayers (SAMS) of photocleavable ligands, containing photosensitive groups such as, coumarin-4-ylmethyl groups, arylcarbonylmethyl groups, metal-based photocleaving groups, and nitroaryl moieties [13]. These SAMs allow the creation of functionalized surfaces which can be activated via exposure to light, altering the chemistry of the surface. In this way, an originally uniform surface can be texture via light exposure—in our case, an isotropic nanoparticle functionalized with a photocleavable SAM could be transformed into a patchy particle by exposing only portions of the nanoparticle to the incident light. Given that nanoparticles are, by definition, smaller than the wavelength visible and UV light, this would at first appear to be a rather difficult proposition.

One way to achieve the desired resolution could be to use metal nanoparticles, which have the ability to enhance and redirect light incident upon them into very small regions through two mechanisms: surface plasmon resonance (SPR) and the lightning rod effect. The former is a collective electron oscillation, excited by the electric fields of the incident light [14,15]. This causes the electrons in the nanosphere to act like a damped, driven oscillator, which can result in significant enhancements to the intensity of the electric field. These enhancements, as well as their location, depend on a variety of factors, including the shape of the particle, as well as the polarization and wavelength of the incident light.

The lightning rod effect is a geometric effect caused by field line crowding along the edges of nanoscale metal surfaces [16,17]. In the lightning rod effect, sharp and/or small metal features redirect incident electric fields, concentrating them in specific regions. Both SPR and the lightning rod effect result in hot spots, areas where the intensity of the light (and fields) is significantly greater than that of the light incident upon the particle as a whole. By combining surface plasmon resonance with photocleavable chemicals, it becomes possible to create patchy particles from isotropically functionalized nanoparticles solely via the introduction of polarized light. In this paper, we describe our first attempt at creating and characterizing such patchiness in silver nanospheroids (AgNSs).

Previous work by our group explored the properties of a member of the an *o*-nitrobenzyl based photocleavable ligand, 1-(6-Nitrobenzo[d][1,3]dioxol-5-yl)ethyl(4-(1,2-Dithiolan-3-

yl)butyl) carbamate (**1**), shown in Scheme 4.1. In Daengngam et al [18] we demonstrated how this ligand undergoes a photouncaging reaction into **1a** when exposed to 1 J/cm^2 of 365 nm light. Furthermore, a 2 mM solution of **1** in ethanol forms a self-assembled monolayer (SAM) when exposed to a gold surface by binding to the gold with its double-sulfide group. The SAM can then be patterned with UV light, which creates areas of **1a** bound to the gold surface. Because **1a** SAMs are positively charged at low (<6) pH, they can be used to electrostatically bind negatively charged gold nanospheres (AuNSs) to a surface, as shown in Figure 4.1.

We will demonstrate that we can transform silver nanonospheroids (AgNSs) isotropically conjugated with **1** into anisotropic patchy particles via exposure to a linearly polarized UV laser at carefully controlled doses. By adhering **1** to AgNSs deposited on a surface, we can utilize SPR (and the lightning rod effect) to enhance the dosage of light received to opposing poles of the nanoparticle, the location of which depends on the angle of polarization. This selectively cleaves **1** into **1a** mainly at the poles, as illustrated in Figure 4.2. If the resulting anisotropic particles are subsequently exposed to an AuNS bath, we can further build on the anisotropy, as the AuNS will adhere to **1a** (but not to **1**), assembling nanostructures on the sample surface that will be aligned to the polarization of the exposing UV light.

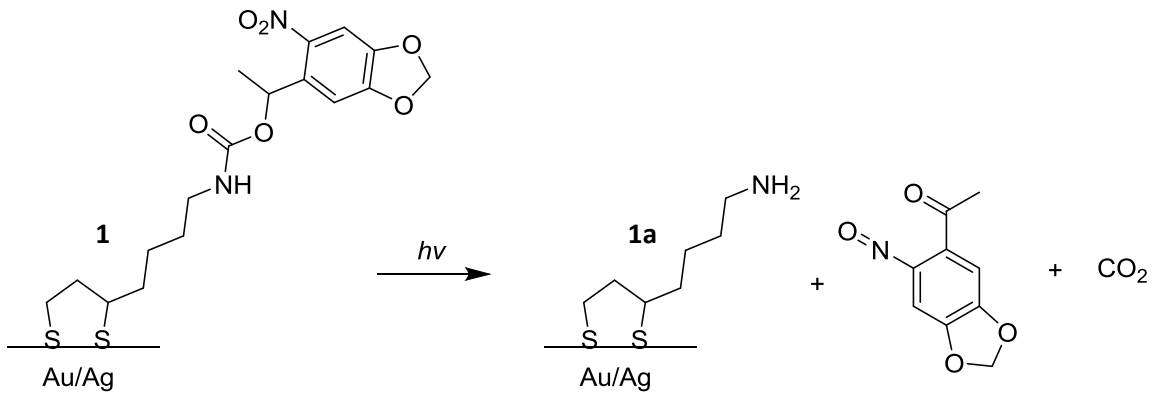

Scheme 4.1: Photocleavable ligand used for this paper. When exposed to ultraviolet light, 1 undergoes photocleavage, resulting in the amine-terminated 1a, its leaving group, and CO_2. Both 1 and 1a can bond or stay bound) to gold and silver surfaces via the double-sulfide group.

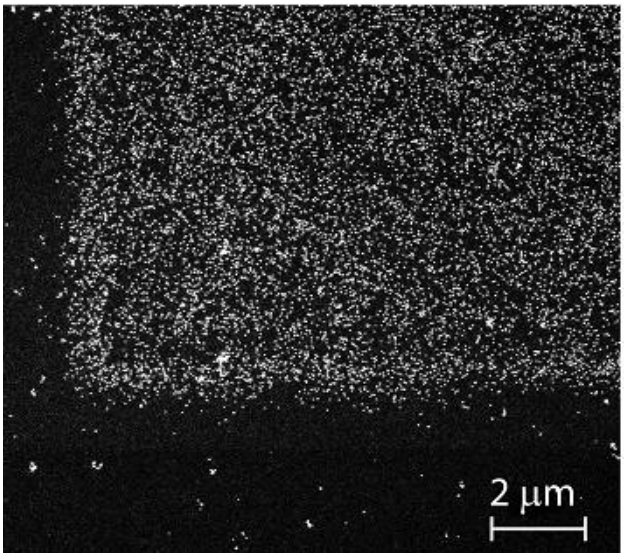

Figure 4.1: AuNSs deposited on a photoactivated substrate functionalized with a monolayer of **1**. Light dots indicate AuNS adhesion, and correspond to irradiation with ultraviolet light, which transforms **1** into **1a**. From Daengngam et al. [18]

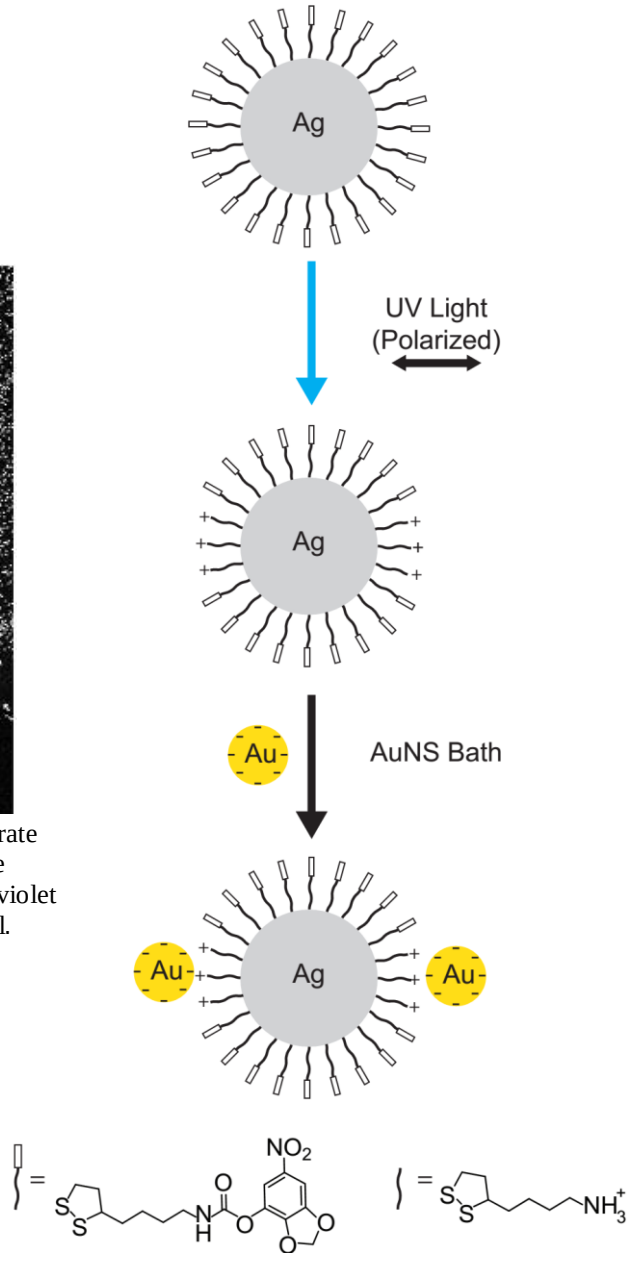

Figure 4.2: A mockup detailing how **1** can be used to build aligned, anisotropic structures. **1**, when adhered to a silver nanosphere, can be selectively photocleaved into **1a** with the help of surface plasmon resonance enhancing the intensity of the incident light at the hotspots. Subsequent exposure to AuNS will result in the selective binding of AuNS to the AgNS

4.3 Materials and Methods

4.3.1 Reagents and Materials

Silver (99.99%) and titanium were purchased from Kurt. J. Lesker Company. The glass substrates used were Fisherbrand Microscope Slides and were purchased from Fisher Scientific. Silver nitrate ($AgNO_3$) 99%, sodium citrate, and chloroauric acid (99.99%) were purchased from Sigma Aldritch. Potassium hydroxide pellets (85%) were purchased from Arcos Organics. Ammonium hydroxide was purchased from Spectrum. Glucose was purchased from Fisher Scientific. 1-(6-Nitrobenzo[d][1,3]dioxol-5-yl)ethyl(4-(1,2-Dithiolan-3-yl)butyl)carbamate was obtained via the method outlined by Daengngam et al [18].

4.3.2 Gold Nanosphere Synthesis

AuNSs were prepared via the Turkevitch method as outlined in G. Frens et al [19]. In brief, 2ml of 40mM trisodium citrate were added to a boiling 100 ml solution of 300 μM chloroauric acid under vigorous stirring, resulting in citrate-capped AuNS of ~10 nm diameter. The pH was adjusted to around 5.4 using diluted hydrochloric acid.

4.3.3 Surface and Sample Preparation

Rough silver nanospheroid (AgNS) surfaces were prepared via the Tollens method as outlined in Wang et al [20].

Glass microscope slides were used as a substrate. Prior to AgNS formation, the slides were prepared by soaking them in Aqua Regia for twenty minutes, rinsed thoroughly with deionized (DI) water, and finally dried with a stream of dry nitrogen gas just prior to use.

3 mL of 0.1 M $AgNO_3$ was then prepared in DI water. A single drop of pure ammonium hydroxide (NH_4OH) was added, resulting in a brown precipitant. Further NH_4OH was added dropwise until the resulting brown precipitant dissolved. The $AgNO_3$ was then mixed with 1.5 mL of 0.8 M KOH, resulting in a black precipitant. Pure NH_4OH was added again until the solution once more became clear. Then, 0.75 mL of the resulting solution was quickly mixed with 0.75 mL of a 0.05 M glucose solution, and drop cast onto the glass slides. The solution was allowed to sit for 75 seconds and then rinsed with DI water to halt the reaction. This resulted in

a glass substrate covered in silver nanospheroids (AgNS), with diameters ranging from 20 to 100 nm and with strong absorption peak between 350 and 450 nm.

The samples were double-rinsed thoroughly in DI water, dried in a stream of compressed air, then placed in a 1 mM solution of **1** in ethanol under argon for about 36 hours. After that time, the samples were removed and dried with a stream of nitrogen gas, and allowed to sit for approximately 5 hours in darkness, unless otherwise stated.

4.3.4 Photoexposure

A majority of the samples were exposed to polarized UV light in order to determine if, and under what conditions, selective photocleavage of **1** occurred on the substrate. Polarized UV light was provided by a 60 mW, 376 nm vertically polarized diode laser. The laser was directed through an OD 0.6 neutral density filter, dropping its power to 15 mW. A beam expander then expanded the laser spot size to a diameter of ~10 mm, resulting in a peak power density of about 76.4 mW/cm^2, assuming a Gaussian beam profile. A programmable shutter was used to control the exposure time (and thereby the dose strength). In order to demonstrate that the aligned anisotropies, if present, were dependent on the direction of the UV light's polarization, the laser was mounted such that its orientation could be varied, generating different polarization angles. A diagram of this setup can be seen in Figure 4.3.

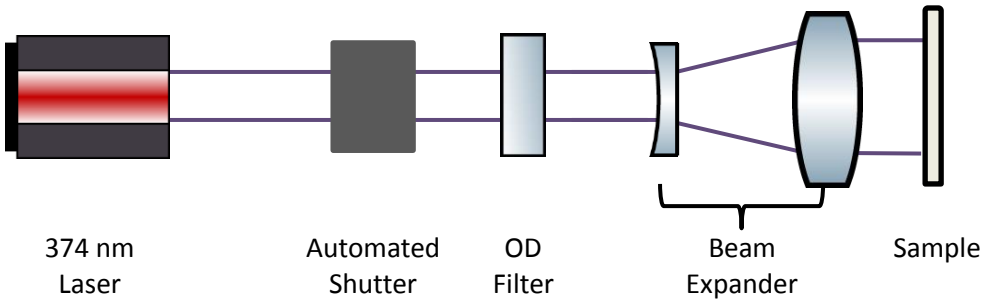

Figure 4.3: Diagram of exposure setup.

In addition to the laser-exposed samples, a control sample was exposed to 1 J/cm^2 of unpolarized UV light with a Fisher Scientific FB-UVXL-1000 UV Crosslinker lamp. A second control received no UV exposure whatsoever.

Table 1 provides an overview of various samples investigated, including both the exposure type and the angle of polarization of the UV light, as measured clockwise with respect with respect to the sample's vertical.

Table 4.1: List of samples, including exposure type and exposure angle (if applicable)

Sample Name	Exposure Type	Exposure Angle
A	UV Laser, 0.3 J/cm^2	30˚
B	UV Laser, 0.3 J/cm^2	0˚
C	UV Laser, 0.3 J/cm^2	-30˚
D	None	N/A
E	UV Crosslinker, 1J/cm^2	N/A
F	UV Laser, 0.3 J/cm^2	30˚ (No AUNS)
G	UV Laser, 10J /cm2	30˚

4.3.5 AuNS Conjugation

Immediately following exposure, all samples (unless otherwise noted) were placed in an aqueous AuNS suspension at pH 6 and left for approximately 24 hours. They were then removed from the suspension, rinsed thoroughly with deionized water, and dried with a stream of compressed air.

4.3.6 Rotational Polarmetric Spectroscopy

Sample analysis and characterization was performed via a modified Filmetrics F10-VC system, shown schematically Figure 4.4. The sample was attached to a rotating stage, and placed in-line with a stationary Edmund Optics wire mesh 400-1200nm polarizer (product #33-082), in order to measure the sample's optical extinction as a function of its orientation with respect to the polarizer. In an ideal setup, we would rotate the polarizer and keep the sample stationary, as the polarizer is be far more uniform than the sample, and so generates less error if not centered perfectly over the axis of rotation. However, the light provided by the Filmetrics system has a minor degree of polarization, meaning we must keep the polarizer fixed in place in order to account for this, and instead rotate the sample. The rotational stage was then mounted in the beam-path of the Filmetrics system to allow for rotational spectroscopy measurements. On all

samples, 0˚ on the polar plot indicates when the linear polarizer is parallel to the vertical axis of the sample.

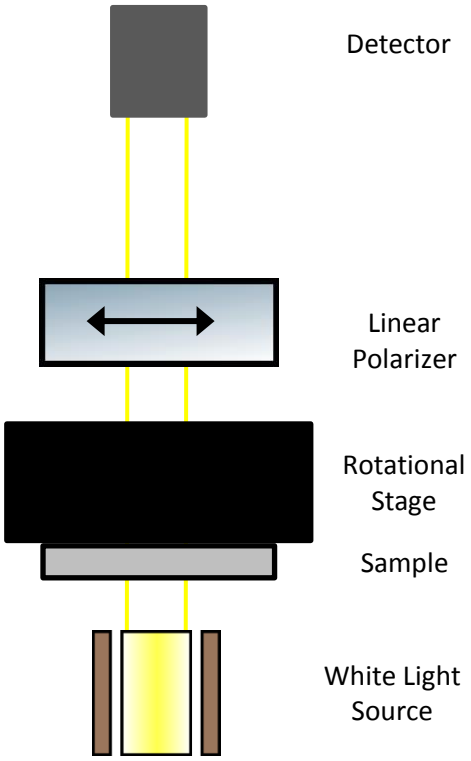

Figure 4.4: Diagram of measurement apparatus.

Some select samples were also measured via rotational spectroscopy between two crossed polarizers. In these cases, the second polarizer is placed between the white light source and the sample, with its axis of polarization at 90˚ to the polarizer placed between the sample and the detector.

4.3.7 AgNS Plasmonic Enhancement

Computationally solving Maxwell's equations for a spherical particle's response to incident electric fields can be done via the Mie expansion of vector spherical harmonics, which can provide calculations for the electrical and optical intensity enhancements generated by plasmon resonance [21]. This expansion can be seen below

$$\boldsymbol{E}_s = \sum_{n=1}^{\infty} E_0\, i^n \frac{2n+1}{n(n+1)} \left(i a_n \boldsymbol{N}_{e\,ln}^{(3)} - b_{\boldsymbol{n}} \boldsymbol{M}_{o\,ln}^{(3)} \right) (1)$$

Where E_0 is the incident electric field intensity, and a_n and b_n are the Mie coefficients, and $\boldsymbol{N}_e^{(3)}{}_{ln}$ and $\boldsymbol{M}_o^{(3)}{}_{ln}$ are vector spherical wave functions. Here, a_n and b_n can be written (in air) as

$$a_n = \frac{m^2 j_n(mx)[xj_n(x)]' - \mu_p j_n(x)[mxj_n(mx)]'}{m^2 j_n(mx)[xh_n^{(1)}(x)]' - \mu_p h_n^{(1)}(x)[mxj_n(mx)]'} \quad (2)$$

$$b_n = \frac{\mu_p m^2 j_n(mx)[xj_n(x)]' - j_n(x)[mxj_n(mx)]'}{\mu_p m^2 j_n(mx)[xh_n^{(1)}(x)]' - h_n^{(1)}(x)[mxj_n(mx)]'} \quad (3)$$

And $\boldsymbol{N}_e^{(3)}{}_{ln}$ and $\boldsymbol{M}_o^{(3)}{}_{ln}$ can be written as

$$\mathbf{M}_{lm}^{(i)}(nk\mathbf{r}) = z_l^{(i)}(nkr)\boldsymbol{\Phi}_l^m(\hat{\mathbf{e}}_r) \quad (4)$$

$$\mathbf{N}_{lm}^{(i)}(nk\mathbf{r}) = \frac{1}{nk}\boldsymbol{\nabla} \times \mathbf{M}_{lm}^{(i)}(nk\mathbf{r}) \quad (5)$$

Where μ_p is magnetic permeability of the particle, ε_p is the electric permittivity of the particle, $m = \sqrt{\varepsilon_p \mu_p}$, $x = \frac{2\pi r}{\lambda}$, j_n and h_n are the spherical Bessel functions of the first and third kind, respectively, $z_l^{(1)} = j_n$, and $z_l^{(3)} = h_n^{(1)}$.

Figure 4.5a shows a density plot of the optical enhancement near the surface for a silver nanosphere 30 nm in diameter when exposed to linearly polarized light at 376 nm. In the visualization of this calculation (Figure 4.5a), the light is incident from the left-hand side of the image and polarized vertically (along the y axis). This provides a qualitative look at the optical intensity enhancement from surface plasmon resonance, as well as the location of the resonance peaks. We can see that the intensity of the enhancement drops off rapidly as we move away from the surface of the sphere. Furthermore, we can see that the enhancement is not perfectly symmetrical about the vertical axis of the sphere, which is expected with larger particles. A more quantitative examination of the enhancement near the surface of the sphere can be found in Figure 4.5b, which plots the optical enhancement at the surface of the sphere as a function of azimuthal angle, where 0˚ is on the side of the sphere opposite the incident light and moving counter-clockwise around the sphere.

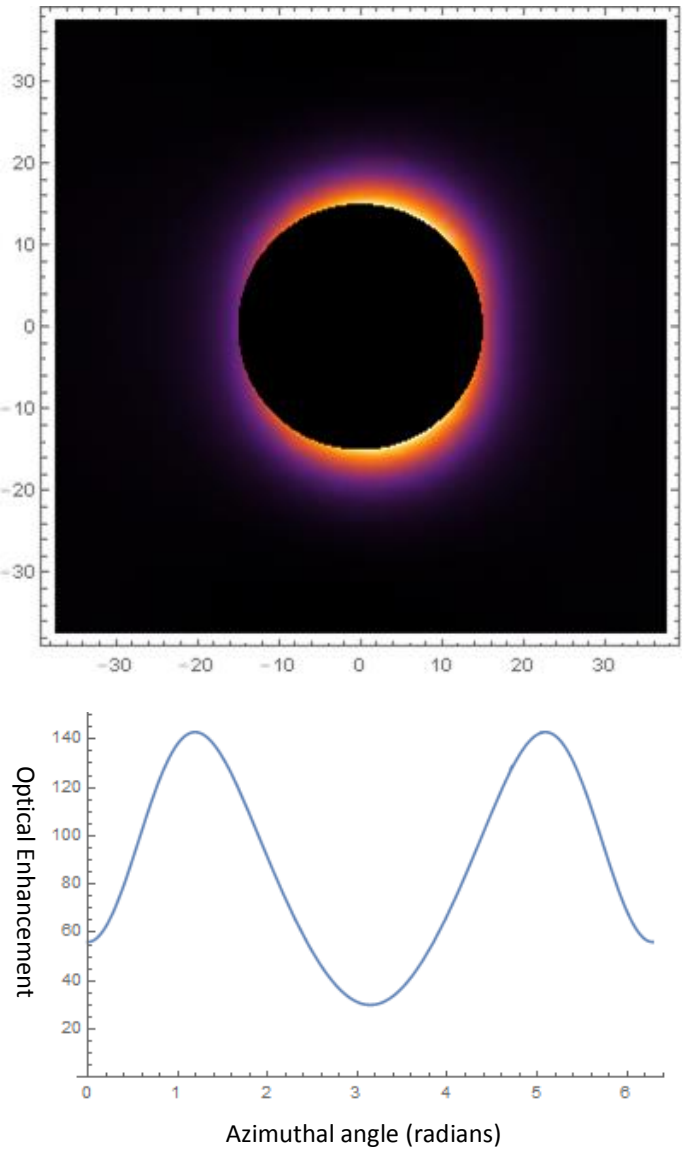

Figure 4.5: Computational results of Mie theory calculations for 30 nm diameter silver sphere exposed to vertically polarized 376 nm light a) A heat map of the optical enhancement near the surface of the sphere b) A graph of optical enhancement at the surface of the sphere as a function of angle.

Figure 4.5b shows that the optical intensity enhancement on the surface of a 30 nm silver sphere exposed to vertically polarized 376 nm light has a maximum of approximately 140 times around 90˚ and 270˚, indicating that the strongest enhancements will be parallel to the polarization of the incident light, i.e at the poles of the sphere. Smaller spheres will experience greater enhancement at this wavelength, and larger spheres less. In theory, this means that we can use light on the order of 0.01 J/cm^2 in order to achieve the desired selective photocleavage effect. Furthermore, we see that the minimum enhancement is still on the order of 20 times, meaning that any exposures above 0.05 J/cm^2 should result in full photocleavage. However, the simulation used to generate this enhancement makes an important assumption: that the sphere is made out of pure silver and uncoated. As this synthesis is carried out in an atmospheric environment, and the AgNS surface is exposed to oxygen at almost every step, this is almost certainly not true—our AgNS almost certainly have an oxide layer covering their surface. Literature shows that this oxide coating can have significant impact on the plasmon resonance of the AuNS, redshifting the resonance peak by 20 nm with even the thinnest of oxide layers. This, combined with the fact that our spheres are coated in **1**, means that the resonance peak is shifted away from 376 nm, and thus our actual enhancement is dramatically smaller than the theory predicts [22,23]. Lastly, the presence of the oxide layer means that our photocleavable ligand is now

physically farther from the hot spots of the plasmonic nanoparticle. As intensity enhancements drop off quickly with distance from the surface of the sphere, the plasmonic intensity is substantially reduced.

4.4 Results and Discussion

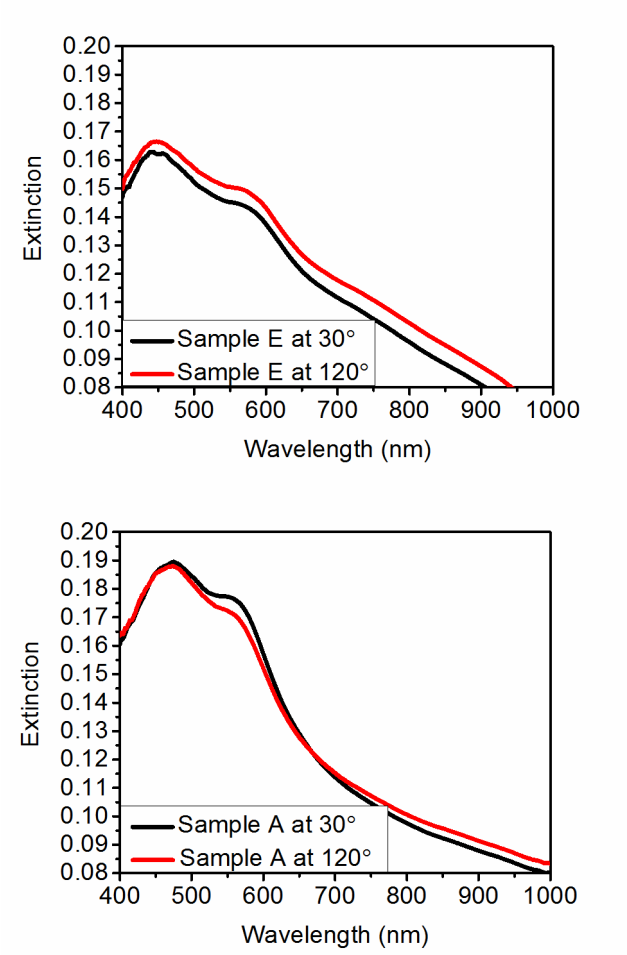

Figure 4.6: Absorption spectra of a) Sample E at 30˚ and 120˚ orientations, showing little variation in absorption intensity across the entire range. b) Sample A at 30˚ and 120˚ orientations, showing significantly different absorption characteristics at 550nm.

To discern the extent to which aligned nanostructures were present on the surface of a sample, extinction spectra were collected using the setup in Figure 4.4, varying the angle between the polarizer and the sample vertical. Aligned metallic nanostructures (such as those outlined in Figure 4.2), will preferentially scatter light polarized at orientations favorable to exciting surface plasmon resonances, effectively altering the polarization of the light passing through them. This, in turn, will result in a dipolar extinction (and transmission) plot when placed in our measurement device, allowing us to determine both if aligned nanostructures are present on our sample, and the orientation of their alignment.

Aligned metal nanostructures preferentially scatter light polarized along the direction of their alignment (which is, in turn, the orientation of the exposure polarization). A gap plasmon (that forms in the gap between two closely spaced nanoparticles) is more pronounced and scatters light better than the plasmon resonances of the individual particles. This gap plasmon is polarized along the axis that joins the particles, which in our case is preferentially

aligned with the exposing light's polarization. For our AgNS-AuNS structures, we can expect a gap plasmon to be in the 550-600 nm rage [24-26]. Therefore, we would expect to have an extinction maximum (and transmission minimum) near 550 nm when the polarized rotational spectrometer and exposure polarization orientations are aligned, due to our structures preferentially scattering light along that axis. We would expect an extinction minima (and transmission maximum) when their axis of alignment (and of exposure polarization) is orthogonal to the polarizer. Similar behavior has been recorded with arrays of aligned gold nanorods [27].

Figure 4.6a plots the extinction spectra from 400 nm to 1000 nm for a sample illuminated with unpolarized UV light prior to AuNS conjugation (Sample E) at both 0˚ and 90˚ orientations, a sample we expect to see no variance in. While the spectra do not line up exactly in terms of intensity (owing, in part, to minor variances in lamp brightness and sample position), we do see that the shape of the graphs are nearly identical to each other, even at the 550 nm position. This suggests that there is no major difference in the absorption of the light for Sample E regardless of sample orientation. Conversely, Figure 4.6b shows the extinction spectra of a sample illuminated with linearly polarized UV light prior to AuNS exposure (Sample A), plotted from 400 nm to 1000 nm at both the 30˚ and 120˚ orientation, where we would expect to see the greatest variance, as sample A was exposed to UV light polarized at 30˚. We can see a clear difference between the two spectra in that the peak at 550 nm is more pronounced in 30˚ spectrum. This peak is due to attachment of AuNS to the silver particles, and this plasmon mode is polarized along the symmetry axis of the Au-Ag dimer. We can therefore conclude that more AuNs are attached to AgNSs along the direction of the polarization of the UV exposure (30˚) than perpendicular to it (120˚).

Because the peak at 550 nm shows the greatest variation in extinction in Sample A, we will plot the extinction centered at the 550 nm wavelength (integrated over a 14 nm bandwidth) in our polar plots. To account for sample variations, as well as lamp fluctuations, we will also normalize our measurements with respect to the signal at 950 nm. At such long wavelengths, the extinction measurements should be unaffected by our sample, as the extinction approaches zero. The exact formula used to calculate the normalized extinction spectra is $-Log\left(\frac{I(550\,nm)}{I_0(550\,nm)}\right) +$

$Log(\frac{I(950\,nm)}{I_0(950\,nm)})$, where I(x nm) is the intensity measurement at wavelength x, I_0(x nm) is the background intensity measurement, taken automatically during system setup.

To better characterize the samples, we will also present crossed-polarizer measurements alongside our single-polarizer measurements. For measurements performed using crossed polarizers, it is our transmission measurements, rather than extinction, that we will find more informative. When rotated between two crossed polarizers, we expect anisotropic aligned metal structures to display a quadrupolar transmission graph, with the maxima occurring when the axis of alignment is at 45˚ to either (and both) of the polarizers. The crossed-polarizer arrangement has the advantage that isotropic scattering contributes nothing to the signal, and completely isotropic samples will generate a near zero signal. This also means that no normalization or background subtraction is required in this case. For ease of graphing and comparison, these samples have been offset such that they share a common extinction miniumum of zero.

4.4.1 Exposure to Polarized UV Light

Figure 4.7 shows the absorption plots of three samples exposed to polarized UV light at 0.3 J/cm^2—Sample A (Figure 4.7a), Sample B (Figure 4.7b) and Sample C (Figure 4.7c). Each absorption plot also contains a blue line, indicating the polarization of the UV light used to expose the sample.

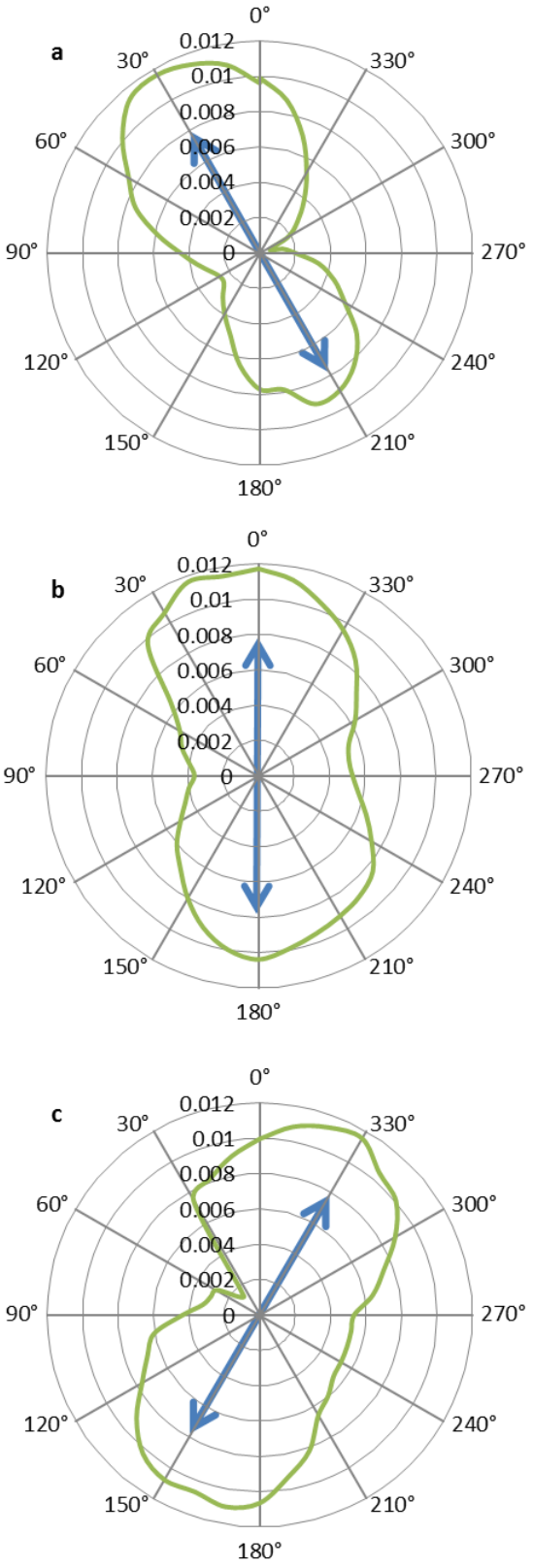

Figure 4.7: Normalized polar absorption plots (at 550nm) of samples exposed to a UV laser at 0.3 J/cm^2, then submerged in an AuNS bath. The angle is the angle between the polarizer and the sample's vertical. The blue line signifies the orientation of the exciting UV laser's polarization for each sample, demonstrating how the dipolar absorption plot tracks with the laser orientation. a) Sample A b) Sample B c) Sample C

For all three samples, the dipolar extinction plots show that the samples have a maximum extinction at 550 nm when the polarizer is aligned with the exposure polarization of the sample. Conversely, when the polarizer is at a 90˚ angle to the exposure polarization, we find an extinction minimum. This is consistent across all three samples, with the orientation of the dipole graph tracking with the orientation of the laser's polarization. Figure 4.8 displays the transmission plot of Sample C, placed between two crossed polarizers. In Figure 4.8, we do see a quadrupolar transmission plot.

When the sample's exposure polarization is aligned with one of the polarizers (at 60˚, 150˚, 240˚, and 330˚), there is a local minimum in the transmission plot. Directly between these points, when the sample's exposure polarization is at a 45˚ to the polarizers, there is a local maximum in the transmission plot. This is indicates that the sample is altering the polarization of the light passing through it, which suggests that Sample C (and, thus, likely Sample A and Sample B) does indeed have anisotropic, aligned metal nanostructures on its surface.

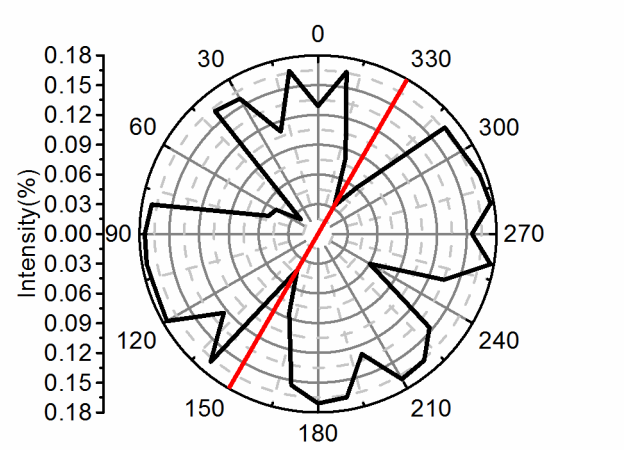

Figure 4.8: Transmission plot (at 550 nm) of Sample C between two crossed polarizers. The quadrupole indicates aligned metal nanostructures on the surface of the sample.

4.4.2 Control Samples

To exclude causes of anisotropy other than those due to anisotropic particle attachment, we fabricated four control samples that under ideal circumstances should not present any anisotropies. These controls include a sample that had not been exposed to any light (Sample D), one that had been fully exposed to unpolarized UV light (Sample E), one that had been exposed to 0.3 J/cm^2 UV light but not incubated in an AuNS suspension (Sample F), and one that was exposed to 10 J/cm^2 UV light.

Figure 4.9a presents the polar plot of extinction at 550 nm for Sample D, which was never exposed to UV light. This shows a minor degree of anisotropy aligned with 0˚, the vertical of the sample. We also see a sharp jump towards 0 at 30˚. This is unexpected, as the Tollens surface should be largely isotropic, as shown in Wang et al [20]. Figure 4.9b shows the extinction plot of Sample E, which was placed in a UV crosslinker (Sample E) and exposed to 1 J/cm^2 of unpolarized UV light, which should have transformed all **1** present on the surface into **1a.** Again, we see a minor anisotropy of approximately the same strength as for Sample D, with an identical alignment, and an identical cut towards 0 at 30˚. This indicates that the addition of the AuNSs did not enhance the existing anisotropy, whether it was structural or a product of the measurement system. This, in turn, suggests the AuNSs adhered isotropically to the AgNSs. In

both cases, the magnitude of the dipoles (from strongest to smallest point) is approximately 1/3 of those seen in the samples exposed to polarized UV light.

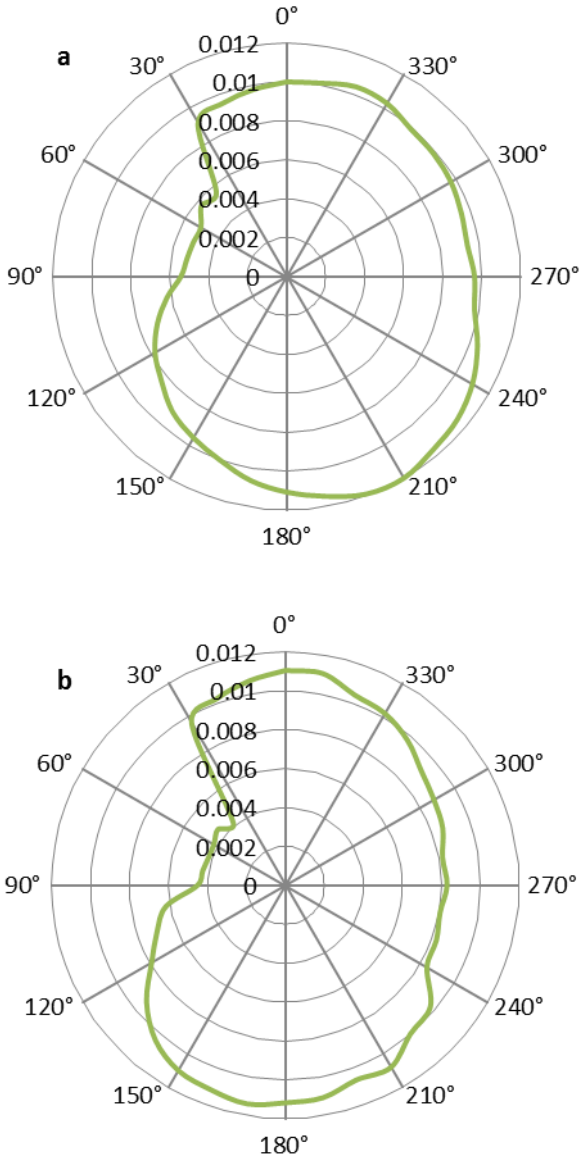

Figure 4.9: Polar plots of the absorption (@550 nm) through a) A glass slide coated in AgNSs (Tollens Sample) conjugated with 1 (Sample D), and b) A sample that was completely photocleaved and exposed to AuNS (Sample E).

Furthermore, we can be certain of the adhesion of AuNSs to the AgNSs by comparing the extinction spectra of Sample D and Sample E, as shown in Figure 4.10. We can see that the spectra differ strongly in the 550-650 nm range. There, Sample E shows a shoulder, indicating the adhesion of AuNSs to the AgNSs. Sample D, however, does not show this result, indicating that no AuNSs adhered to the sample.

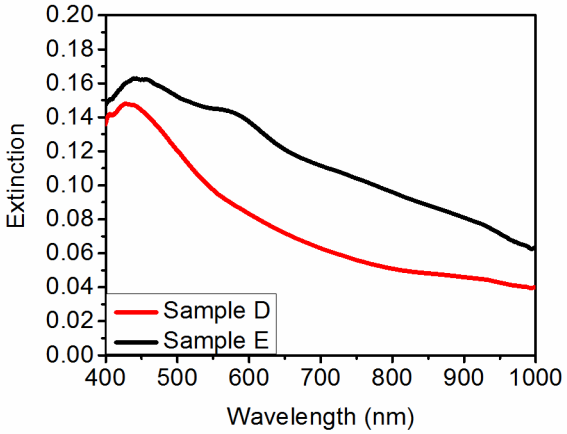

Figure 4.10: Extinction spectra of samples D and E, showing the adhesion of AuNSs to Sample E by means of the shoulder and extended peak in the 550-600 nm range.

If the dipolar pattern seen in Figures 4.9a and 4.9b are due to aligned nanostructures on the substrate, a quadrupolar transmission pattern should result if the sample is rotated between crossed polarizers, as seen in Figure 4.8. Figures 4.11a and 11b show such data from Sample D and E

respectively. While the patterns are not perfectly circular, they show no distinct quadrupole pattern. From this, we conclude that the weak dipole patterns seen in Figures 4.9a and 4.9b are likely due to an intrinsic anisotropy of our setup, and not preferential alignment of the nanoassemblies on samples D and E.

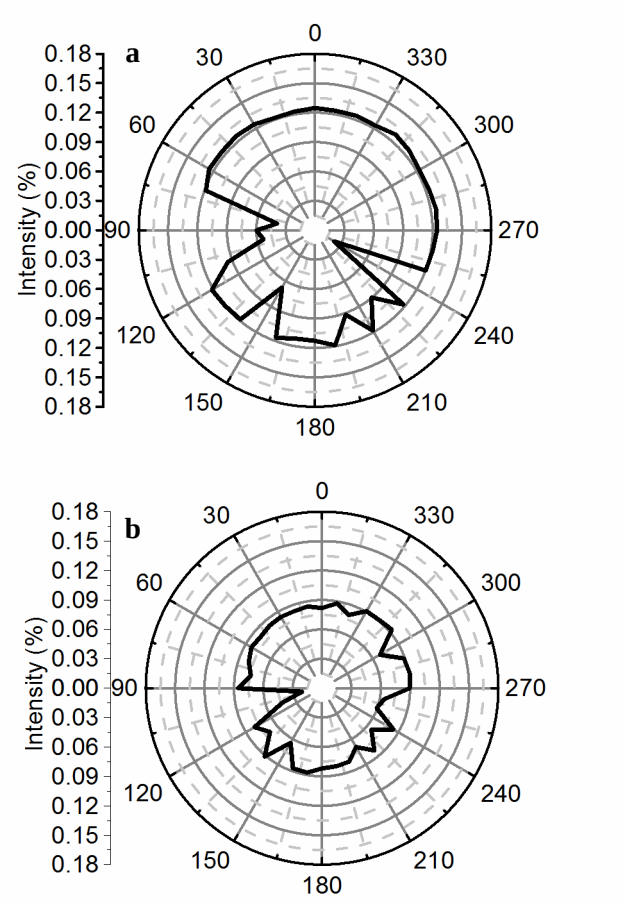

Figure 4.11: Polar transmission plots (at 750 nm) of two different samples placed between crossed polarizers. a) Had no exposure to UV, b) Was exposed to 1 J/cm^2 of unpolarized UV light and submerged in an AuNS bath. Neither show a quadrupole pattern, indicating there are no aligned metal nanostructures on the surface.

Figure 4.12 shows the absorption plot for Sample F, which was exposed to polarized light from the UV laser, but was not incubated in an AuNS bath. This was done in order to make certain that the UV laser light exposure was not by itself causing any aligned structural anisotropies, for instance by causing patchy oxidation of the AgNSs. The polarization of the laser was at a 30˚ angle, and the sample received a 0.3 J/cm^2 dose of UV light, the same as received by samples A, B, and C. In Figure 4.12, we see an elongated extinction pattern aligned with the vertical axis, comparable in magnitude and shape to that observed in the other control samples. This informs us that the UV-laser exposure by itself is likely not creating any significant structural anisotropies, and that the extinction patterns seen in Figure 4.7 do indeed come from self-assembled, aligned, anisotropic structures comprised of both AgNSs and AuNSs.

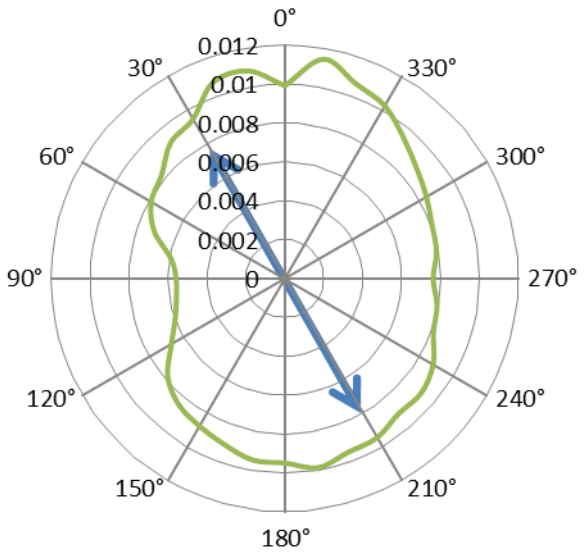

Figure 4.12: Sample F, exposed to polarized UV laser at 30˚ (blue line), but not to AuNS. It shows anisotropies similar to those in Figure 7.

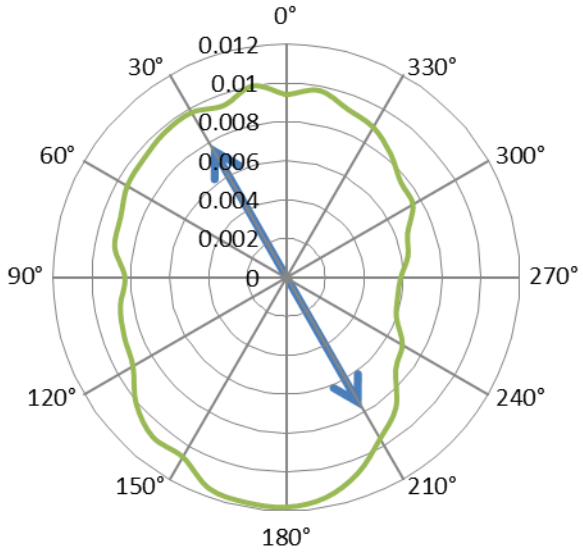

Figure 4.13: Normalized polar absorption plot (@550nm) of Sample G, exposed to polarized UV laser at a dose of 10J/cm2, then placed in an AuNS bath. Unlike the polar plots in figure 8, this shows a dipole absorption plot independent of the UV-laser orientation, similar to those seen in the controls.

Lastly, Figure 4.13 shows the extinction plot for a sample exposure to polarized light with a dose of 10 J/cm^2 (Sample G). Here, too, we observe a pattern very similar to the other controls, implying that the structure on its surface are similar to the sample exposed to unpolarized light. In other words, if the dose is sufficiently high, all areas of the silver particles are fully exposed regardless of polarization, and the alignment anisotropy goes away.

4.4.3 FESEM Imaging

While the above data is fairly conclusive, images of the surface could bolster our case. FESEM imaging of Sample A is shown in Figure 4.14, falsely colored to show AuNSs in yellow. While strongly suggestive of aligned exposure, is not entirely conclusive. While we do see a number of AuNSs (false colored in yellow) adhering to the AgNSs (grey) along the axis of polarization, we also see some degree of non-specific binding outside of that alignment. This is not, however, entirely unexpected. Previous work with **1** has shown that even a partial exposure (sub 1 J/cm^2) to UV light will cause some photocleavage into **1a,** which in turn allows for some AuNS adhesion even when not all **1** has been cleaved into **1a**. As our AgNS substrates are resonant near the UV spectrum, and do receive some exposure outside of the hotspots, some degree of non-specific binding is to be expected.

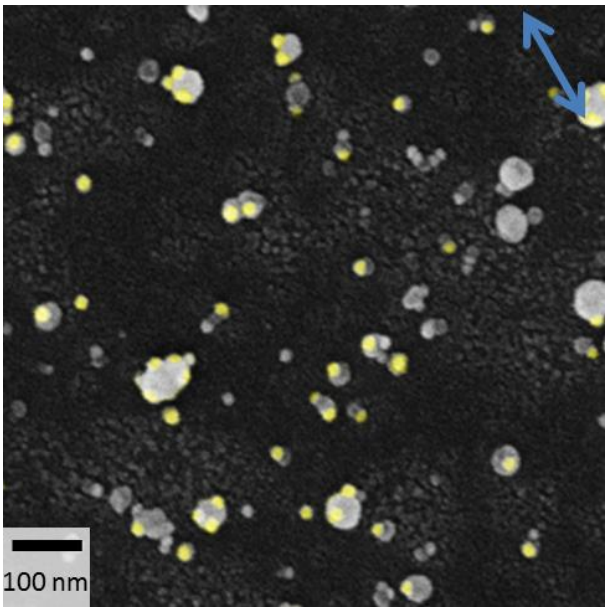

Figure 4.14: FESM image of Sample A. AgNSs are the bright grey blobs, and AuNSs are false colored in red. The blue arrow indicates the polarization of the incident UV laser.

4.5 Discussion

Together, these results are indicative of the fact that we have, indeed, created aligned metallic nanostructures from our AuNS and AgNS building blocks, with the alignment determined by the axis of polarization of the incident light. The polarization alignment of the exposing UV light determines the orientation at which **1** will preferentially be cleaved into **1a**, and then negatively charged AuNSs then bound to the areas where **1a** was present, creating aligned plasmonic nanostructures on the surface. While our controls do not show perfectly anisotropic extinction, the spectra from the controls are unaffected by laser orientation, and are all of approximately the same intensity. In contrast, the samples which we exposed to linearly polarized UV light showed that the extinction spectra would shift with, and match, the orientation of the linearly polarized UV light, which is evidence both that we are indeed creating these structures, and that the samples are is isotropically conjugated with **1** prior to the polarized UV exposure.

While our FESEM data, shown in Figure 4.14, does not show a perfect alignment free of nonspecific binding, it does help support (and certainly does not negate) the previous data, which

indicates the existence of aligned anisotropies. Further, even if the SEM data is not fully conclusive, it is likely that the circumstances that generated the polar absorption plots are an ensemble effect, and may not be easily discernable by visual inspection.

4.6 Conclusion

We have demonstrated the ability to bind **1** to AgNS, and then to generate anisotropic patches of positively charged **1a** in a dipolar shape on the surface by exposing it to polarized UV light. Introducing negatively charged AuNSs to this system leads to the self-assembly of aligned structures parallel to the exciting light's axis of polarization, making the anisotropy apparent in optical measurements.

Future research will include attempting to combine this technique with a photo-reversal effect described in See et al [28] in order to create structures aligned orthogonal to the original UV-polarization. Other plans include replicating this process with an AuNS based substrate (as opposed to an AgNS one), utilizing the lightning-rod effect, rather than plasmon resonances, to create aligned nanoscale structures.

Chapter 4 References

[1] Zhang and S. C. Glotzer, Nano Letters **4**, 1407 (2004).
[2] A. B. Pawar and I. Kretzschmar, Macromolecular Rapid Communications **31**, 150 (2010).
[3] É. Duguet, C. Hubert, C. Chomette, A. Perro, and S. Ravaine, Comptes Rendus Chimie **19**, 173 (2016).
[4] A. Walther and A. H. E. Müller, Chemical Reviews **113**, 5194 (2013).
[5] Q. Chen, S. C. Bae, and S. Granick, Nature **469**, 381 (2011).
[6] S. Gangwal, O. J. Cayre, and O. D. Velev, Langmuir **24**, 13312 (2008).
[7] A. Perro, S. Reculusa, S. Ravaine, E. Bourgeat-Lami, and E. Duguet, Journal of Materials Chemistry **15**, 3745 (2005).
[8] J. Du and R. K. O'Reilly, Chemical Society Reviews **40**, 2402 (2011).
[9] S. U. Pickering, Journal of the Chemical Society, Transactions **91**, 2001 (1907).
[10] L. Hong, S. Jiang, and S. Granick, Langmuir **22**, 9495 (2006).
[11] A. Walther and A. H. E. Muller, Soft Matter **4**, 663 (2008).
[12] Y. Yang, Z. Jia, Y. Wang, Y. Gu, and J. Qin, Colloid and Polymer Science **291**, 1049 (2013).
[13] P. Klán, T. s. Šolomek, C. G. Bochet, A. l. Blanc, R. Givens, M. Rubina, V. Popik, A. Kostikov, and J. Wirz, Chemical reviews **113**, 119 (2012).
[14] A. Wokaun, Molecular Physics **56**, 1 (1985).
[15] K. L. Kelly, E. Coronado, L. L. Zhao, and G. C. Schatz, The Journal of Physical Chemistry B **107**, 668 (2003).
[16] O. J. F. Martin and C. Girard, Applied Physics Letters **70**, 705 (1997).
[17] L. Novotny, R. X. Bian, and X. S. Xie, Physical Review Letters **79**, 645 (1997).
[18] C. Daengngam, S. B. Thorpe, X. Guo, S. V. Stoianov, W. L. Santos, J. R. Morris, and H. D. Robinson, The Journal of Physical Chemistry C **117**, 14165 (2013).
[19] G. Frens, Nat Phys Sci **241**, 20 (1972).
[20] Z. Wang, S. Pan, T. D. Krauss, H. Du, and L. J. Rothberg, Proceedings of the National Academy of Sciences **100**, 8638 (2003).
[21] B. G. Garcia-Camara, Francisco; Moreno, Fernando; Gomez-Medina, Raquel; Saenz, Juan; Nieto-Vesperinas, Manuel, in *Smart Nanoparticles Technology*, edited by A. Hashim (INTECH, 2012).
[22] Y. Yin, Z.-Y. Li, Z. Zhong, B. Gates, Y. Xia, and S. Venkateswaran, Journal of Materials Chemistry **12**, 522 (2002).
[23] A. Henglein, Journal of Physical Chemistry **97**, 5457 (1993).
[24] C. Ciracì, R. T. Hill, J. J. Mock, Y. Urzhumov, A. I. Fernández-Domínguez, S. A. Maier, J. B. Pendry, A. Chilkoti, and D. R. Smith, Science **337**, 1072 (2012).
[25] L. He, E. A. Smith, M. J. Natan, and C. D. Keating, The Journal of Physical Chemistry B **108**, 10973 (2004).
[26] K. Su, Q. Wei, X. Zhang, J. Mock, D. R. Smith, and S. Schultz, Nano letters **3**, 1087 (2003).
[27] Q. Liu, Y. Cui, D. Gardner, X. Li, S. He, and I. I. Smalyukh, Nano Letters **10**, 1347 (2010).
[28] E. M. See, C. L. Peck, X. Guo, W. L. Santos, and H. D. Robinson, (Unpublished).

Chapter 5

5 Selective Self Assembly on Gold Nanorods

5.1 Introduction

In Chapter 4, we used substrates coated with AgNSs for plasmonic self-assembly driven by a linearly polarized UV laser, which in part worked due to the natural plasmon resonance of the AgNS substrate being close to the absorption band of **1**. This allowed us to use LSPR to direct the linearly polarized UV light to the poles of the AgNSs, and to preferentially cleave **1** into **1a** at these locations. However, the LSPR also brings with it some degree of nonspecific binding. While the optical enhancement is strongest at the poles (s ee Figure 4.5), there is significant light intensity at every position around the nanosphere, leading to some photocleavage (and AuNS adhesion) even in areas that are not strongly plasmonically enhanced. This makes it more difficult to visually characterize the samples with AuNSs, as shown in Figure 4.14. Furthermore, relying solely on particles with a plasmon resonance near the absorption band of **1** significantly limits the structures we can create.

We turn, then, to AuNRs, which our group has previously used in selective self-assembly with **1**. As AuNRs have plasmon resonances far from **1**'s absorption band, we cannot rely on the LSPR enhancement of UV light to direct the photocleavage and subsequent self-assembly. Previously, our group has used the lightning rod effect (described in section 5.2) to affect controlled self-assembly of AuNSs onto the tips of AuNRs, using UV light with some degree of success. We propose that it is also possible to use multi-photon absorption (described in section 5.3) in conjunction with the longitudinal plasmon resonance of AuNRs to cause the selective photocleavage of **1** into **1a**.

5.2 Lightning Rod Effect:

While previous sections have focused on the optical enhancement generated via surface plasmon resonance, earlier work by our group has relied on another form of nanoscale optical enhancement. Even outside of the surface-plasmon resonance conditions, metallic nanoparticles

are capable of enhancing the electromagnetic intensity in certain areas on their surface. This is caused by enhanced fields that occur near sharp metallic features, which has led to it being called the lightning rod effect. This effect arises *purely* as a consequence of the geometry of the structure, and not the wavelengths or the structures plasmon resonance. In the lightning rod effect, field line crowding occurs near features with small radii, which in turn results in an enhancement of the electromagnetic field in these regions. This enhancement can, depending on geometry, be on the order of tens to hundreds of times the intensity of the incident field [1,2].

5.3 Multi-Photon Absorption

Direct excitation with UV light is not the only method by which **1** might be photocleaved into **1a.** Instead, if n photons, each with one n^{th} the necessary photoactivation energy, are incident upon the molecule at the same time, **1** can photocleave into **1a** via a process known as multi photon absorption. Multi photon absorption is of particular interest because of the increased selectivity it provides when attempting to photocleave **1.**

The master equation for the photocatalytic reaction of **1**into **1a** can be written as $\dot{\mathbf{c}} = \boldsymbol{\alpha} I^n(1 - \mathbf{c})$**,** where **c** is the fraction of reacted **1a** (that is, the fraction of **1a** present) I is the intensity of the incident light, *n* is the degree of photoabsorption (single-photon, two-photon, three-photon, etc.), and $\dot{\mathbf{c}} = \frac{\mathrm{d}c}{\mathrm{d}t}$. The constant α is determined by the specifics of the reaction, including the n-photon cross section and a setup-dependent geometric correction factor. As we are comparing the selectivity of single photon absorption to multi-photon absorption, we do not need to examine α in depth.

From the master equation, and from the starting condition that at t=0, c=0 (no **1** has photocleaved into **1a**), we can derive an equation for the fraction of **1a** present given a specific optical intensity and exposure time: $c = 1 - e^{-\boldsymbol{\alpha} I^n t}$. Using the Taylor expansion, this becomes $c = 1 - (1 - \boldsymbol{\alpha} I^n t + (\boldsymbol{\alpha} I^n t)^2 - (\boldsymbol{\alpha} I^n t)^3 + \cdots$. For small doses, we can eliminate all but the first order term, leaving us with $c = \boldsymbol{\alpha} I^n t$, a reaction that proceeds linearly in time, but proceeds as the n^{th} power of optical intensity, where n is the level of multi-photon absorption. This, in turn,

means any effects that enhance or alter the intensity of incident light (such as the lightning rod effect or LSPR) will themselves be enhanced to the n^{th} degree.

If a particle receives a 100 times enhancement at its plasmonic hotspots, then for small photoexposures under single-photon absorption, we would expect there to be 100 times more **1a** present at the hot spots than elsewhere on the surface. However, if the particle is undergoing a multi-photon absorption, then we would expect a selectivity of 100^n, or 100^n times more **1a** at the hotspots than elsewhere on the particle (assuming an exposure such that $c<<1$ at all locations). This allows multi-photon absorption, when combined with plasmon enhancement or the lightning rod effect, to offer a far greater selectivity in defining patches with distinct properties. This premise is not so different from the ways in which plasmon resonance can enhance Raman scattering in SERS, as discussed in Chapter 1.

As shown in Figure 3.8 from Chapter 3, **1** has an absorption band centered at the 360nm wavelength, with an absorption edge at about 400nm. Therefore, if two photons near 720nm are incident upon the molecule at the same time, **1** can absorb both to gain the energy needed for the photo-uncaging reaction that frees the amine group, transforming into **1a**. Previous work by Magill et al. has demonstrated, however, that this may be more complicated than simple two-photon absorption, and that **1** on an Au substrate has shown results consistent with *multi*-photon absorption in the 720nm range [3].

While the range needed for multi-photon absorption of **1** demonstrated by Magill et al [3] is outside the resonant range of regular Au and Ag nanospheres, it is within the resonant range that can be achieved by AuNRs. Figure 2.4 in Chapter 2 shows the absorption spectrum of a batch of AuNRs specifically grown for this experiment. This spectrum shows a longitudinal plasmon resonance of approximately 740nm, overlapping the range used by Magill et al. for multi-photon absorption. This resonance is important because the enhancement offered by the lightning rod effect is very weak--on the order of 5 times the intensity of the incident light. This means, under multiphoton absorption, hot spots see a selectivity of 5^n times higher when only the lightning rod effect is used for optical enhancement. AuNRs, however, can have optical enhancements on the order of 500 times at their longitudinal plasmonic hotspots, meaning that under multiphoton absorption they could see a selectivity enhancement of 500^n times between the hotspots and the rest of the nanoparticle, allowing for greatly refined selectivity.

5.4 Lightning-rod effect Driven Self Assembly on AuNRs

Previously, our group explored the binding of AuNSs to AuNRs utilizing **1** via exposure to UV light [4]. The premise was to utilize the lightning rod effect to concentrate the incident UV light at the poles of the nanorod. This would, ideally, mean that we would photocleave **1** into **1a** only at the ends of the rods, where the light intensity was enhanced. This, in turn, would allow the AuNS to adhere only at the ends of the nanorod, and, creating a dumbbell shaped structure. A mockup of this can be seen in Figure 5.1.

Figure 5.1: AuNS (blue) adhesion to AuNR's solely at the rod tips, where the enhancement from the lightning rod effect will be greatest.

Drawn from Chalongarat Daengngam's thesis, Figure 5.2 shows the results of exposing an AuNR sample to six different doses of UV light, followed by a low pH AuNS bath. These doses are, in order, an unexposed sample (Figure 5.2a), a 0.15 J/cm^2 sample (5.2b), a 0.29 J/cm^2 dose of UV light (Figure 5.2c), a 0.42 J/cm^2 dose (Figure 5.2d), a 0.57 J/cm^2 dose (Figure 5.2e), and a 0.7 J/cm^2 dose (Figure 5.2f). While all doses are below the dose required to fully photocleave all **1** into **1a** (1 J/cm^2), we nevertheless see AuNSs bound to AuNRs in all samples that received UV exposure, and no AuNS binding in the sample that did not. Furthermore, in Figure 5.2c, we see spheres binding, primarily, to the nanorod tips. Figure 5.2b shows this as well, but with less binding. Starting with Figure 5.2d, we can also see that as dose strength increases towards 1J/cm^2, we begin to see more and more nonspecific binding, with many spheres adhering to the sides of the rods in addition to the tips. However, even Figure 5.2c shows

some small nonspecific binding, and while the images suggests a some degree of success, our previous work suggests a low yield for this technique. In order to more selectively and successfully adhere the AuNS to the AuNR, we will need to turn to a different methodology.

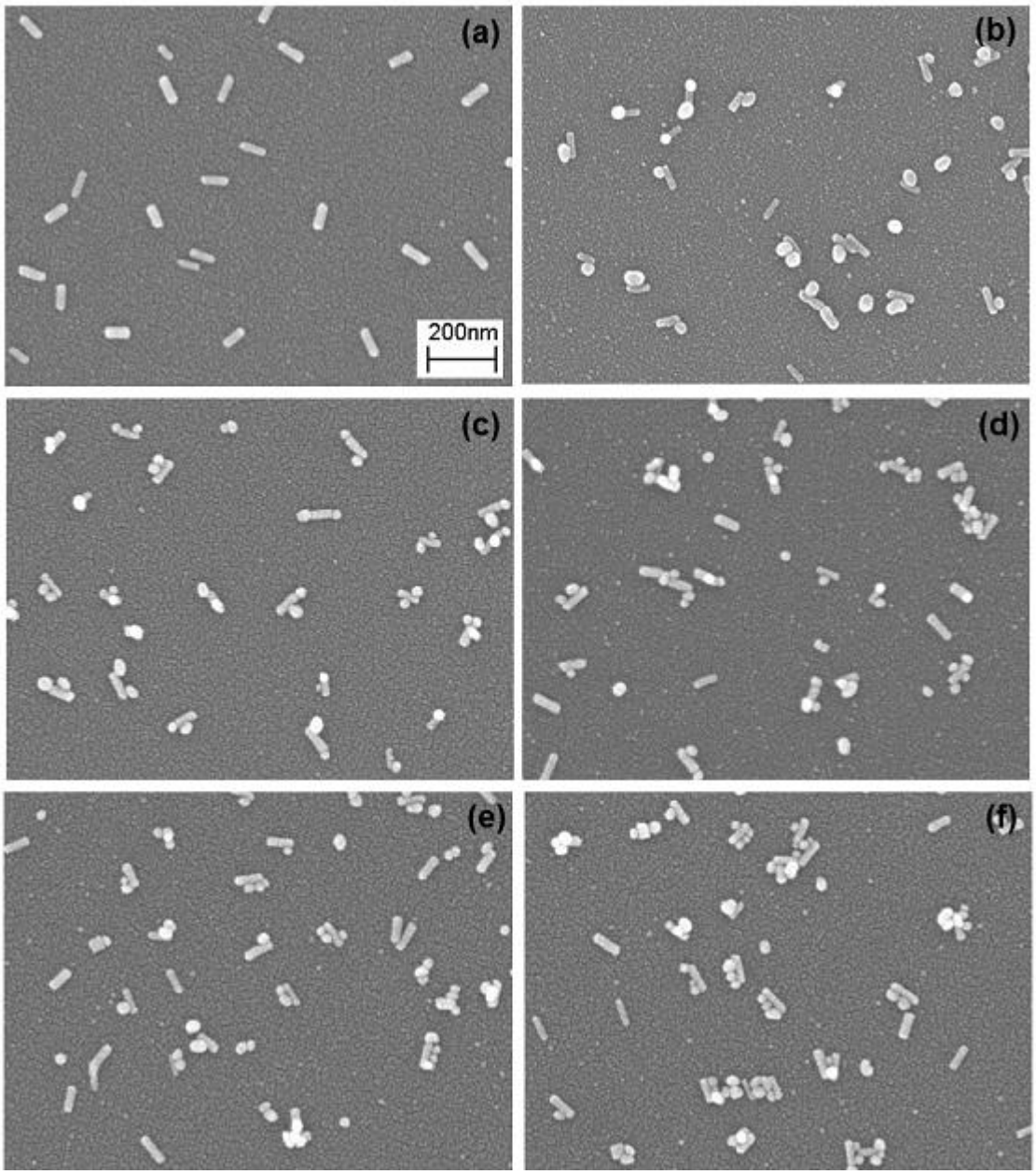

Figure 5.2: AuNRs coated in 1 exposed to increasing doses of UV light, then exposed to a low pH AuNS bath, prompting AuNS binding on photocleaved areas of 1. Dose strengths are a) 0 J/cm^2 b) 0.15 J/cm^2 c) 0.29 J/cm^2 d) 0.42 J/cm^2 e) 0.57 J/cm^2 f) 0.7 J/cm^2 Taken from Daengngam et al.[4]

5.5 AuNR Sample Setup

As only a small area of the AuNR substrate is exposed to the laser (described in section 2.7.3), every sample included two landmarks by which both the laser exposure and subsequent SEM imaging could be guided: a physical, etched line in the sample surface, and an over-exposed laser line, shown in the schematic of the sample in Figure 5.3 . These allowed us to find the same area with both the patterning laser and the SEM imaging afterwards. The first landmark was prepared by scratching the sample substrate with a diamond scribe prior to AuNR deposition, creating a line in the surface. The second landmark was created during the laser patterning of the substrate, where immediately below the scratched line we created a single, horizontal line of overexposure. By overexposing this area to the laser, we were able to physically ablate the AuNRs from the sample surface, which presents in the SEM images as a long, blank line (shown in the micrograph in Figure 5.3). Subsequent patterned areas were performed at fixed, documented intervals below this over exposed line, running parallel to it. Together, these allow us to locate the areas of the sample that had been patterned by the laser, as well as determine what laser exposure each examined area received.

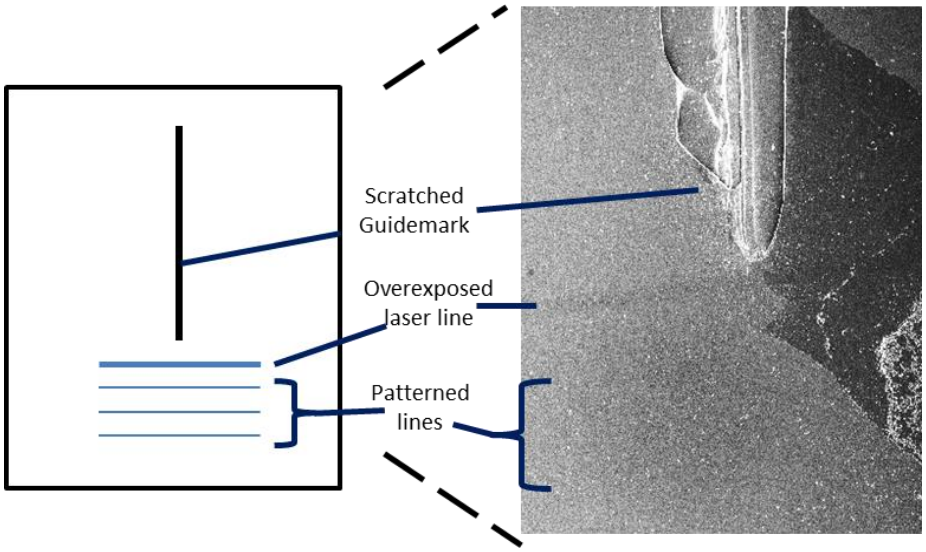

Figure 5.3: Two landmarks (etched mark in glass, over-exposed laser-line) used to find the specific patterned areas on the sample. Contrast enhanced.

AuNR adhesion follows the procedures laid out in Chapter 2.5. Laser exposure was done via the method outlined in section 2.7.3, using the ultrafast, femtosecond pulsed laser. This was followed by incubation with AuNSs by dropcasting 10x concentrated AuNS solution on the substrate for 1 day.

5.6 Results

After exposure and incubation with nanoparticles, samples were characterized in a FESEM in order both to determine the AuNS-binding density and to characterize the specificity of the binding of AuNSs to the rod ends. By examining the actual surface, we can determine whether AuNSs have adhered to the AuNR, and in what configurations. We must also examine control samples—a sample exposed to unpolarized UV light, and a sample exposed to neither UV nor high intensity pulsed red light, to demonstrate that any selective self-assembly comes only from the exposure to the femtosecond pulsed laser.

Figure 5.4 is an image of a control sample that was exposed to neither UV nor circularly polarized red light prior to submersion in a AuNS bath. To better show and separate these bindings, the FESEM images have been fake colorized to show rod-sphere pairs. We can see very little adhesion of AuNSs to the surface, indicating a lack of nonspecific binding. This suggests that the AuNSs are not binding strongly to the nanorods in the absence of photoexposure, which is what we would expect for a surface uniformly conjugated with **1.** This is good, as it suggests our unexposed control is not showing a significant degree of AuNS binding.

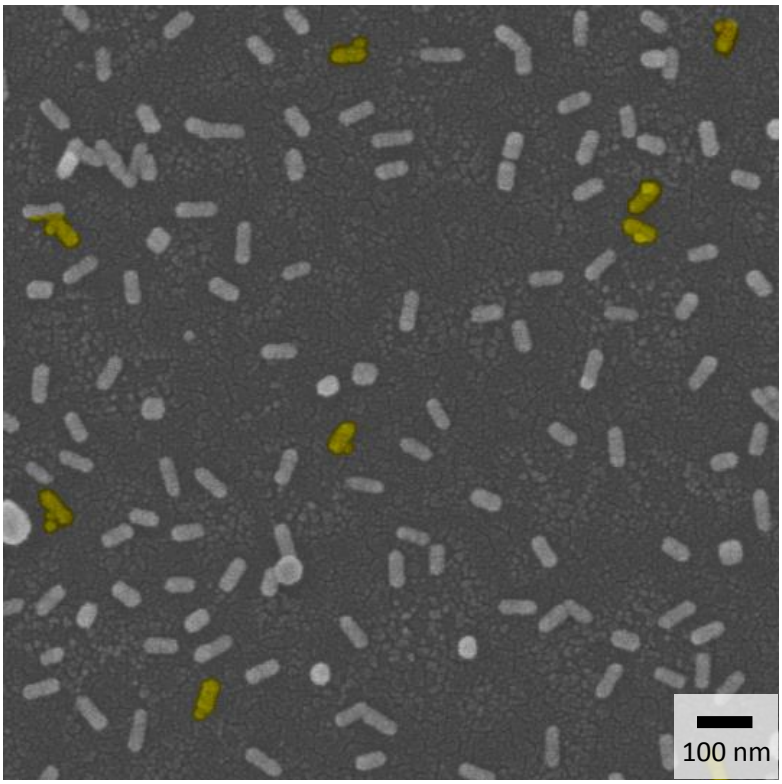

Figure 5.4: Unexposed sample conjugated with **1** and submerged in low pH AuNS bath. Note the lack of AuNS adhesion on the sample.

Conversely, Figure 5.5 shows areas of a sample that were exposed to 1 J/cm^2 of UV light, which should result in nearly complete photocleavage of **1** into **1a**. Here, we see a high degree of AuNS binding, both to the tips and sides of the AuNRs. There is no major trend in either direction—the binding appears, primarily, to be random. This both confirms **1** has successfully

been conjugated to our samples, and when exposed to a large dose of UV light is photocleaving into **1a** with no discernable preference for AuNR tips vs AuNR slides.Figure 5.6, in comparison, shows an FESEM image of an area that was exposed to femtosecond pulsed, circularly polarized light a wavelength of ~730 nm and a power of ~45.3 mW at the center o the beam. Both the wavelength and the high intensity of the fs pulses, especially when focused, are conducive to multi-photon absorption leading to photocleavage of **1**. As before, in the false color images, AuNS-AuNR pairs are false colored in yellow.

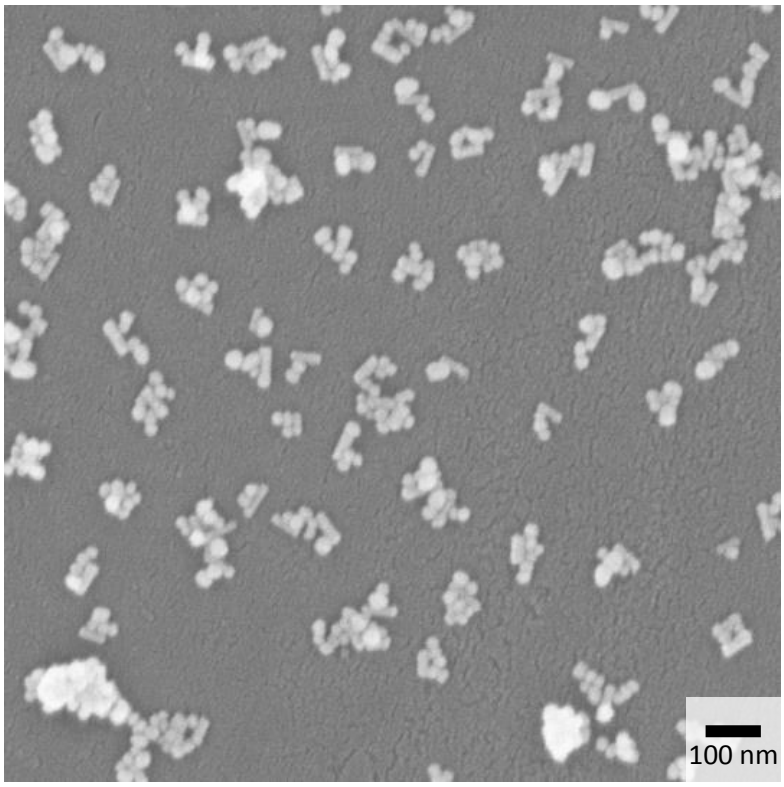

Figure 5.5: Exposed (UV, 1 J/cm^2) sample conjugated with **1** and submerged in low pH AuNS bath. AuNSs have bound copiously to every nanorod spot available, clustering strongly along their length.

Figure 5.7 shows another area of the same sample, albeit at a higher magnification, showing that this selective binding is consistent across the exposed areas.

We can see a clear distinction between the two samples patterned via femtosecond pulsed, 730nm wavelength laser light (Figures 5.6 and 5.7), and the unexposed and UV exposed controls (5.4 and 5.5). In Figure 5.5, the AuNSs have bound all over the rods, indicating indiscriminate photocleavage. In comparison, Figures 5.6 and 5.7 show the AuNSs binding, primarily to the ends of the rods. This difference between the UV-exposed and femtosecond pulsed laser samples is critical, as it helps reinforce that this controlled binding is, in fact, due to plasmonically enhanced multi-photon absorption, and not due to the lightning rod effect, as was the case in Figure 5.2.

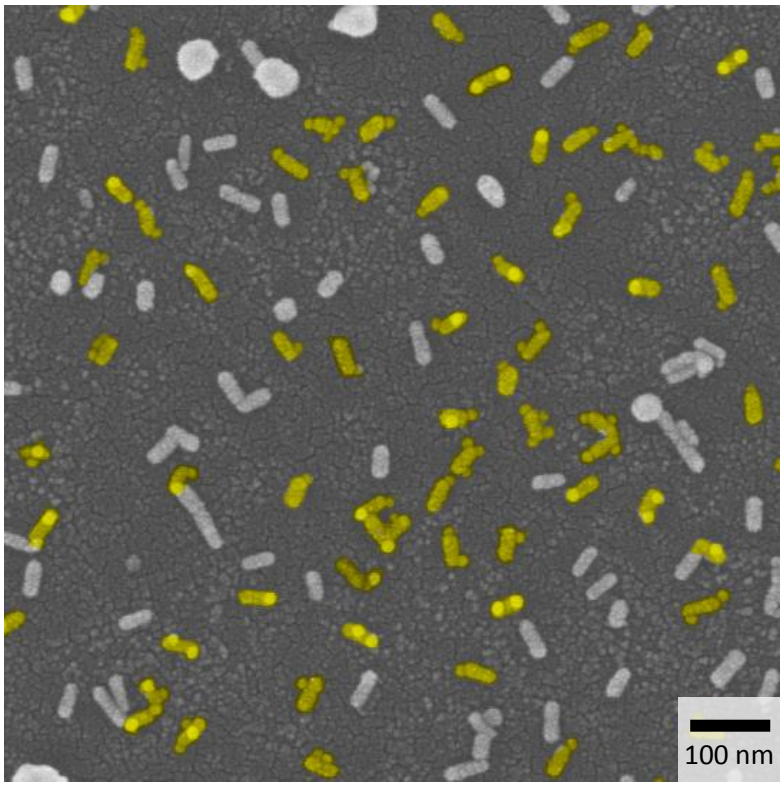

Figure 5.6: Sample exposed to femtosecond pulsed circularly polarized red light, then submerged in an AuNS bath. False-colored in yellow are pairs were AuNSs have bound to AuNRs.

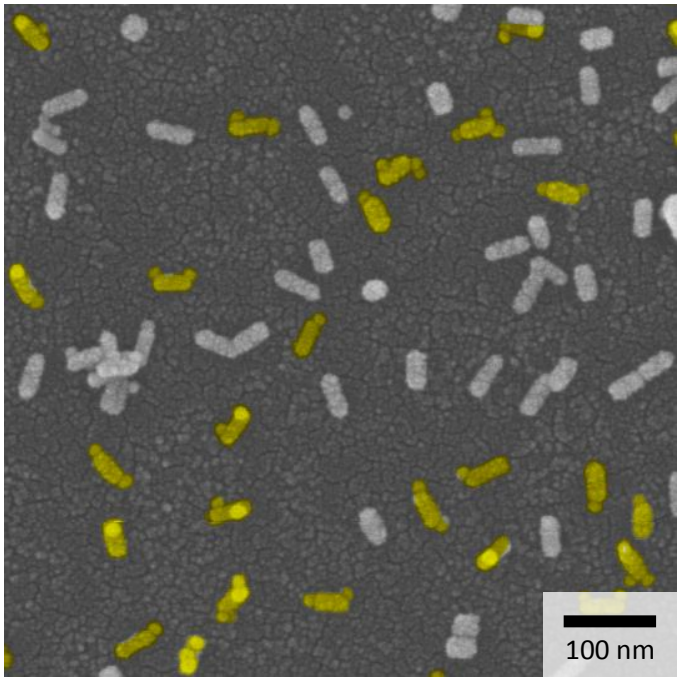

Figure 5.7: Different area of the sample shown in Figure 5.6, at higher magnification, showing that the selective adhesion was not relegated to a single area.

5.7 Conclusion

While these are only preliminary results, they do indicate that we have been able to selectively cleave **1** into **1a** via multi-photon absorption using circularly polarized, femtosecond pulsed 730nm light and that the reaction is preferential to the hot spots at the ends of the rods. Future goals include replicating this effect across multiple samples, both to demonstrate its repeatability, provide statistical analysis of the efficacy of this technique, and to determine the optimum exposure power, duration, and other conditions necessary to achieve high-yields and low non-specific binding. This process is ongoing. Beyond that, other projects include attempting this two-photon activated self-assembly in solution, as opposed to on a surface, as is performed here.

Chapter 5 References

[1] L. Novotny, R. X. Bian, and X. S. Xie, Physical Review Letters **79**, 645 (1997).
[2] O. J. F. Martin and C. Girard, Applied Physics Letters **70**, 705 (1997).
[3] B. A. Magill, X. Guo, C. L. Peck, R. L. Reyes, E. M. See, R. M. Davis, W. L. Santos, and H. D. Robinson, TBA **TBA**, TBA (TBA).
[4] C. Daengngam, Dissertation, Virginia Polytechnic Institute and State University, 2012.